

Heavy Ion Beam Pumped KrF^{*} Excimer Laser

Dissertation
zur Erlangung des Doktorgrades
der Naturwissenschaften

vorgelegt beim Fachbereich Physik
der Johann Wolfgang Goethe-Universität
in Frankfurt am Main

von

Aleksey Adonin
aus Sankt-Petersburg

Frankfurt 2007

D 30

vom Fachbereich Physik der Johann Wolfgang Goethe-Universität
als Dissertation angenommen.

Dekan:

Prof. Dr. Wolf Aßmus

Gutachter:

Prof. Dr. Joachim Jacoby
Priv. Doz. Dr. Andreas Ulrich

Datum der Disputation:

14. März 2008

Abstract

The high energy loss of heavy ions in matter as well as the small angular scattering makes heavy ion beams an excellent tool to produce almost cylindrical and homogeneously excited volumes in matter. This aspect can be used to pump short wavelength lasers.

In an experiment performed at the GSI (Gesellschaft für Schwerionenforschung, Darmstadt, Germany) ion accelerator facility in December 2005 the well-known KrF* excimer laser was pumped with an intense high energy uranium beam. Pulses of an uranium beam with initial particle energy of 250 MeV per nucleon, provided by heavy-ion-synchrotron SIS-18, were delivered to the HHT-target station and then stopped inside a gas laser cell. The maximum beam intensity reached in the experiment was $2,5 \cdot 10^9$ particles per pulse, which resulted in 34 J/g specific energy deposited in the laser gas. By applying electron cooling and a bunch compression technique at SIS-18, the beam pulses were compressed down to 110 ns (FWHM).

A mixture of an excimer laser premix gas (95,5% Kr + 0,5% F₂) and a buffer gas (Ar 4.8) was used as the laser gas in proportions of 35/65 and 60/40, respectively. The gas pressure inside the laser cell was varied in the range of 1,2÷2 bar in continuous flow mode. The experimental setup consisted of a 1 m long stainless steel tube with a number of diagnostic viewports and two mirror adjustment units. The optical cavity was formed by a flat, Al-coated mirror at the beam entrance and a second dielectrically coated, highly reflective mirror with 3 m radius of curvature at a distance of 1,3 m.

A beam of heavy ions has been used to pump a short wavelength gas laser for the first time. Laser effect on the KrF* laser transition ($\lambda = 248 \text{ nm}$) has been successfully demonstrated. Laser threshold for this specific setup was reached with a beam intensity of $1,2 \cdot 10^9$ particles per pulse. Laser action has been clearly proofed by the following methods: appearance of the laser line, spectral narrowing of the laser line, temporal narrowing of the laser signal, non-linear response of the laser output intensity on the pumping power, and cavity disalignment effect. An energy of the laser pulse of about 2 mJ was measured for an ion beam intensity of $2 \cdot 10^9$ particles per pulse. The time delay of the onset of the laser emission with respect to the pumping pulse was measured as a function of ion beam intensity. The dependence of spontaneous emission spectra on the gas pressure in a range of 1,3÷2 bar was observed and the optimal gas pressure for laser experiments in the sense of laser efficiency was concluded.

As a next step in studying short wavelength lasers pumped with heavy ion beams it is planned to reduce the laser wavelength down to the VUV region of the spectrum, and to proceed to the excimer lasers of the pure rare gases: Xe₂* ($\lambda = 172 \text{ nm}$), Kr₂* ($\lambda = 146 \text{ nm}$), Ar₂* ($\lambda = 126 \text{ nm}$), Ne₂* ($\lambda = 83 \text{ nm}$) and He₂* ($\lambda = 80 \text{ nm}$). We believe that the use of heavy ion beams as a pumping source may lead to new pumping schemes on the higher lying level transitions and considerably shorter wavelengths (XUV and X-ray spectral region), which rely on the high cross sections for multiple ionization of the target species.

Contents

1. Introduction	1
1.1 Motivation of the work	1
1.2 Goals for the first experiment	3
2. Theoretical Background	7
2.1 Interaction of heavy ion beams with matter	7
2.1.1 Stopping power in cold matter	8
2.1.2 Calculation of “cold” stopping	11
2.1.3 Energy deposition by the ion beam	12
2.2 Rare gas halogen excimers	13
2.2.1 Electronic structure and binding parameters	14
2.2.2 Spectroscopy and radiative parameters	15
2.2.3 Formation and quenching	18
3. Design of the Experiment and Numerical Predictions	27
3.1 Selection of the ion beam parameters	27
3.2 Ion beam envelope calculation	28
3.3 Selection of an entrance window to the laser cell	31
3.4 Ion beam stopping in the gas mixture	33
3.5 Energy deposition in the entrance mirror	40
3.6 Calculation of the laser spot sizes	41
3.7 Optical gain calculations	42
3.8 Conclusions	46
4. Experimental Setup and Diagnostics	47
4.1 GSI accelerator facility	47
4.2 Setup of the optical cavity	50

4.2.1	Vacuum System.....	51
4.2.2	High Pressure Gas System	52
4.2.3	Opto-Mechanical System of the Laser Cavity	53
4.2.4	Pressure and Diagnostic Windows.....	53
4.3	Diagnostic tools	54
4.3.1	Ion beam diagnostics	54
4.3.2	Spectral measurements.....	60
4.3.3	Laser and spontaneous emission measurements	61
4.3.4	Remote adjustment of cavity mirrors.....	63
5.	Experiment and Results	65
5.1	Ion beam and target parameters.....	65
5.2	Calculation of the ion beam sizes at the cavity entrance.....	67
5.3	Ion beam diagnosing with CCD-cameras	69
5.3.1	Ion energy at cavity entry.....	69
5.3.2	Ion beam spot size.....	69
5.4	Spectrometer data	72
6.3.1	Demonstration of the laser effect	72
6.3.2	Spectral narrowing of the laser line.....	74
6.3.3	Dependence of spontaneous emission on gas pressure	75
5.5	Measurements with photodiodes	77
6.4.1	Light output from the ion beam intensity.....	78
6.4.2	Temporal narrowing of the laser emission.....	80
6.4.3	Time delays of the laser emission	83
6.4.4	Calculation of the laser output power	83
5.6	Calculations of the Laser efficiency from the Threshold value.....	84
6.5.1	Laser threshold value	85
6.5.2	Threshold conditions.....	85
6.5.3	Laser Efficiency	86
5.7	Observation of transversal structure of the laser light.....	88
5.8	Entrance cavity mirror under the ion beam	89
6.	Conclusions and Outlook	93
6.1	Main results of the present work	93
6.2	Suggestions and outlook for future experiments	95

6.3	Numerical estimations for future experiments	96
Supplement		103
A.	Calculation of gases concentrations in the laser gas mixture	103
B.	Observed atomic spectral lines	107
C.	Damaged reflective area on the entrance mirror.....	109
Bibliography		113
Zusammenfassung		127
Acknowledgements		135

Abbreviations and Symbols

AXUV	–	<i>Absolute X-ray and Ultraviolet detectors</i>
CCD	–	<i>Charge Couple Device</i>
FCT	–	<i>Fast Current Transformer</i>
FWHM	–	<i>Full Width at Half Maximum</i>
GSI	–	<i>Gesellschaft für Schwerionenforschung, Darmstadt, Germany.</i>
HHT	–	<i>High energy High Temperature</i>
NIR	–	<i>Near Infrared</i>
PHELIX	–	<i>Petawatt High-Energy Laser for heavy Ion experiments</i>
UNILAC	–	<i>Universal Linear Accelerator</i>
USB	–	<i>Universal Serial Bus</i>
VUV	–	<i>Vacuum Ultraviolet</i>
A_{ul}	–	<i>spontaneous emission rate</i>
R_{lu}	–	<i>pumping rate in a volume unit</i>
B_{ul}	–	<i>stimulated emission rate</i>
C_{ul}	–	<i>collision decay rate</i>
ε	–	<i>specific deposited energy</i>
$\varepsilon_x, \varepsilon_y$	–	<i>transversal emittances of the ion beam</i>
g_{ss}	–	<i>small signal gain coefficient</i>
I_{beam}	–	<i>number of particles in ion beam pulse</i>
λ	–	<i>wavelength</i>
N_u	–	<i>upper state population</i>
p_{pd}	–	<i>pumping power density</i>
S	–	<i>stopping power of medium ($S = -dE/dx$)</i>
S_{beam}	–	<i>ion beam spot size</i>
σ_{st}	–	<i>stimulated emission cross section</i>
τ	–	<i>radiative lifetime of excited atoms and molecules</i>
Z_p	–	<i>ion charge state</i>

List of Figures

Fig.2.1:	<i>Energy losses of ^{238}U ions in Ar gas over a wide energy range</i>	10
Fig.2.2:	<i>Potential energy diagram of KrF^* molecule</i>	15
Fig.2.3:	<i>Fluorescent spectrum of Ar/Kr/F_2 laser gas mixture.</i>	16
Fig.2.4:	<i>Electronic terms behavior of Kr^* and F_2</i>	20
Fig.2.5:	<i>Reaction kinetics of KrF^* in Ar/Kr/F_2 laser gas</i>	25
Fig.3.1:	<i>Scheme of the ion beamline at HHT experimental area</i>	29
Fig.3.2:	<i>Ion beam focusing inside a laser cavity</i>	29
Fig.3.3:	<i>Ion beam envelopes for different beam focusing parameters</i>	30
Fig.3.4:	<i>Ion beam straggling inside the laser cell</i>	36
Fig.3.5:	<i>Ion beam spot size as a function of depth inside the laser cell</i>	37
Fig.3.6:	<i>Energy loss of U-ions in the excimer gas calculated with SRIM</i>	38
Fig.3.7:	<i>Power density distribution deposited by U-beam</i>	39
Fig.3.8:	<i>Laser beam in a half-symmetric resonator</i>	42
Fig.4.1:	<i>GSI accelerator facility</i>	48
Fig.4.2:	<i>Beam transport line at the HHT experimental area</i>	49
Fig.4.3:	<i>Heavy-ion-beam laser setup</i>	51
Fig.4.4:	<i>Scheme of the heavy-ion-beam laser setup</i>	52
Fig.4.5:	<i>Transmission curves for Sapphire and MgF_2 in UV-VIS range</i>	54
Fig.4.6:	<i>Time structure of the ion beam pulse recorded with FCT</i>	55
Fig.4.7:	<i>Experimental setup with diagnostics</i>	56
Fig.4.8:	<i>Spectral response of PixelFly CCD image sensors</i>	58
Fig.4.9:	<i>Light profile of the ion beam in the laser gas</i>	59
Fig.4.10:	<i>Example of a laser spectrum recorded with HR4000</i>	60
Fig.4.11:	<i>Structure scheme and quantum efficiency of AXUV photodiodes</i>	62
Fig.4.12:	<i>Reflectivity curves for Al-MgF_2 mirror for different coating</i>	63
Fig.5.1:	<i>Light intensity profile of a uranium beam in Ar</i>	70
Fig.5.2:	<i>Appearance of the laser line on the on-axis spectrum</i>	73
Fig.5.3:	<i>Spectral narrowing of the laser line</i>	74
Fig.5.4:	<i>Spectra of spontaneous emission at different gas pressures</i>	75
Fig.5.5:	<i>Relative emission intensities of the main spectral components</i>	76
Fig.5.6:	<i>Intensity ratio of the KrF^* and Kr_2F^* emissions</i>	77
Fig.5.7:	<i>Dependence of spontaneous emission on the beam intensity</i>	78

Fig.5.8:	<i>Laser output intensity as a function of ion beam intensity</i>	79
Fig.5.9:	<i>Time structures of ion beam, spontaneous and laser pulses</i>	81
Fig.5.10:	<i>Laser pulse duration as a function of ion beam intensity</i>	82
Fig.5.11:	<i>Time delays of the laser emission from the ion beam pulse</i>	83
Fig.5.12:	<i>Transversal structure of the laser light</i>	88
Fig.6.1:	<i>Emission spectra of the pure rare gas excimers</i>	95
Fig.6.2:	<i>Ion beam envelope inside the gas cell for U-ions</i>	99
Fig.B.1:	<i>Saturated spectra of the spontaneous emission of the laser gas</i>	107

Chapter 1

Introduction

1.1 Motivation of the work

Lasers are widely applied in many branches of human activity. They occupy a wide spectral range from mid-infrared (several micrometers) down to X-ray (several nanometers) and they are used with different types of pumping sources from electrical current provided by a small battery (semiconductor lasers) to a flux of nuclear fission fragments, provided by a big reactor facility [You81, Kar97], depending on the power and purpose of the laser. The shorter the wavelength used in the laser the higher power is required for pumping. In this work the first successful operation of a KrF* excimer laser ($\lambda = 248$ nm) pumped with an intense, highly energetic uranium ion beam is demonstrated [Ulr06a, Ulr06b, Ado07a]. The ion beam has been provided by the heavy-ion-synchrotron SIS-18 at GSI (Gesellschaft für Schwerionenforschung, Darmstadt, Germany) ion accelerator facility.

The basic idea of heavy ion beam pumping of gas lasers is to use the specific features of the ion interaction with matter. First of all, heavy ions have a very high energy loss in matter which scales quadratically with the charge of the projectile and allows high pumping power densities in the laser medium. Moreover, a number of experiments performed at GSI have demonstrated a strong dependence of the ions energy loss on the matter properties, in particular extremely high stopping power was observed in ionized matter [Jac95]. Secondly, heavy ions have a unique ability to produce non-thermal excitation of atoms and molecules of the stopping medium which is one of the general requirements for pumping short wavelength lasers. And finally, heavy projectiles have a small angular scattering in the propagated medium, which in combination with ion beam focusing and the dependence of

power deposition to the medium from the projectile energy gives almost cylindrical and homogeneously excited volume on the beam axis [Tah05a, Tah05b]. This can be well matched with the mode volume of a laser cavity [Ulr06a].

Due to a strong improvement of beam intensity and beam quality over the last few years, the SIS-18 at GSI became capable to provide intense, energetic and short pulsed heavy ion beams with low emittance. Therefore the experiment described in the present work was performed to study the possibility of using such beams for pumping short wavelength lasers.

For the first time heavy ion beam pumping of gas lasers had been demonstrated in 1983 in the Munich Tandem van de Graaff accelerator by pumping an infrared He-Ar laser with a 100 MeV ^{32}S beam [Ulr83]. These experiments were stimulated by experiments on nuclear pumped gas lasers in which the power level of He-Ar laser had been scaled up to 1 kW [You81, Kar97]. A flux of nuclear fission fragments was used there as a pumping source of gas lasers. Various laser schemes, driven by heavy ions, have been studied later [Ulr91, Bus93, Ulr94a, Sa198], but due to the limited pumping power densities, provided by ion accelerators, the wavelength range of the ion beam pumped lasers had been limited to the infrared and visible spectral region [Ulr83, Ulr94b]. But now this situation has changed due to the significant improvement of beam parameters at the GSI and it became possible to extend the wavelength of the ion beam pumped gas lasers to UV and, hopefully, VUV region.

The laser experiment, presented in this work, was performed in the context of plasma physics studies at the GSI facility. These studies aim at the production and investigation of high energy densities in matter [Hof05]. The general aspects of the formation of plasmas, induced by heavy ion beams, have been extensively studied over the last years [Ulr87, Jac90, Jac95, Tah05a, Tah05b]. Short wavelength lasers pumped with ion beams could be used as a sensitive tool for studying ion beam induced plasmas, because population inversion and laser effect only occurs under specific conditions with respect to plasma density and temperature, electron density and temperature, as well as opacity of the target material at the laser wavelength. A comparison of measured laser parameters with model calculations can provide a deep insight into the excitation and relaxation processes in ion beam induced plasmas [Ulr06a].

A serious competition to heavy ion beams in pumping short wavelength lasers could be made by high-power pulsed lasers. Using high power lasers it became possible to obtain and study the laser effect in the X-ray spectral region. The first X-ray laser was demonstrated in 1985 in the transition of neon like ions of Se (20,63 nm and 20,96 nm) by exploding thin Se-foils with short-pulse high power green laser [Ros85, Mat85]. Since that time, laser pumped X-ray lasers have made significant progress: the wavelength was reduced down to the “water window”¹ [Max93, Spi97] and the pulse duration down to a few picoseconds [Kli02, Abo03]. At the GSI accelerator facility a high-intensity and high-energy laser system named PHELIX (Petawatt High-Energy Laser for Heavy-Ion Experiments) is under construction. The system consists of a long- and a short-pulse front end providing up to 20 ns and 130 fs pulses respectively. It will provide laser pulses of energies up to 4 kJ (in a high-energy mode) and recompressed pulses of powers up to 1 PW (in a high-intensity mode) [PHEL]. In 2003 the first X-ray laser experiment on PHELIX has been performed. Strong lasing was observed at $\lambda = 22$ nm in nickel-like zirconium pumped using the front end of the PHELIX laser system [Neu04]. However, conversion efficiencies (in the order of 10^{-6}) and repetition rates (one shot every 5-6 minutes) of such lasers are still very low [PHEL].

1.2 Goals for the first experiment

For the first experiment with heavy ion beams the well known KrF* excimer laser line at a wavelength of 248 nm has been chosen. This wavelength was chosen due to two main reasons: firstly, it is rather short, already in the UV region, and secondly, it is still easy to detect. Radiation on this wavelength can propagate in air without strong attenuation, so there is no need to evacuate the light path for observation. Moreover, 248 nm is still in the working range of usual quartz optics (diagnostic windows, lens, fibers, etc.) and CCD detectors used in cameras and spectrometers. All this allows making the detection of spontaneously emitted and laser light much more simple than in the case of VUV ($\lambda < 200$ nm) or X-ray radiation.

The main goal for the first experiment was to achieve a laser effect in a cavity and to prove laser action with several independent methods. In the case of a successful observation of the laser action the following aims have been assigned:

¹ „Water window“ is a wavelength region between the K absorption edge of oxygen at 23,3 Å and the K absorption edge of carbon at 43,7 Å. In this region water is relatively transparent [See89].

- to measure the laser pulse parameters (output power, pulse duration, etc.) as a function of pumping power,
- to obtain a laser threshold value for a specific cavity setup,
- to study an optical gain as a function of pumping power density,
- to estimate a conversion efficiency of the ion beam energy to the laser energy,
- to study a laser saturation intensity as a function of pumping power,
- to find optimal gas pressure and laser gas consistence (mixing ratio between buffer gas and excimer laser premix) in order to increase the laser efficiency,
- to observe spatial characteristics of the laser radiation,
- to study a possible influence of non-linear hydrodynamic effects in the laser gas, heated by the ion beam, on the laser operation at high pumping power densities.

This thesis is dedicated to the first UV excimer laser pumped with the beam of heavy ions. In Chapter 2 some theoretical aspects of an interaction of heavy ions with cold matter are given. In the second part of this chapter it is paid attention to rare gas halide excimers. Electronic structure, spectroscopy and reaction kinetics are discussed in details on the example of KrF^* molecule. Also a number of references on the previous works in this field are given.

The design of the experiment, selection of the ion beam parameters as well as the results of some numerical simulations (calculations) of the ion beam inside the laser cavity are represented in Chapter 3. Also predictions for pumping power density and optical gain, expected to achieve in the experiment are discussed.

Chapter 4 is dedicated to the experimental setup of the laser cavity. In the beginning a short overview of the GSI accelerator facility and HHT experimental area is given, where the experiment has been performed. Various systems constituent to the laser installation are discussed in details. A lot of attention is given to the diagnostics, used in the experiment. The spectroscopic and time resolved intensity measurements of spontaneous and laser radiation as well as ion beam intensity and space profile measurements are particularly described.

The carrying out of the experiment and main results of the work are discussed in Chapter 5. An analysis of the experimental data obtained from different detectors (photodiodes, spectrometers, CCD-cameras, etc.) combined with calculations of the parameters, which could not be measured directly during the experiment, has provided a lot of information and it is also given in this chapter.

Finally, in Chapter 6 the conclusions which can be drawn from this work are noted, underlining the main results. Suggestions and an outlook for future experiments and possible extension of the work are given. Also two possible experiments with Xe and Kr excimers, which do not require significant changes in the present setup, are considered. The maximum deposited power density as well as the optical gain for both cases is estimated, taking into account existed parameters of the ion beam.

Chapter 2

Theoretical Background

This chapter is dedicated to some theoretical aspects of the two big fields of physics, which are directly related to the present work, Plasma Physics and Atomic Physics.

In the first part, the main results of research carried out previously in the fields relevant to “ion beam interaction with dense matter” are discussed. These fields include atomic processes occurring during slowing down of heavy ion beams in matter as well as the effects connected to high energy density states that can be induced in the material by intense beams. Some basic theoretical concepts of the energy loss of relativistic heavy ions due to ionization of the medium and related effects are considered.

The second part is dedicated to one of the exotic class of molecular gases – rare gas halogen excimers, and to the widespread type of the gas lasers in UV region – excimer lasers. Specific aspects of an electronic structure, binding and transition parameters as well as particularity of formation and quenching of excimer molecules are discussed with regards to lasers.

2.1 Interaction of heavy ion beams with matter

The subject of penetration of energetic heavy ions through matter has fascinated generations of physicists over the past decades because of its applications to basic and applied sciences as well as to industry. As a result, there has been a continuous effort among the scientific community to improve the understanding of various complex physical processes that are involved in such beam-matter interactions. These include the energy dissipation of the projectile ions due to interaction with bound and free electrons of the target matter, elastic and inelastic nuclear collisions and evolution of the charge-

state distribution of the projectile ions. The momentum transfer to the target nuclei in elastic (Coulomb) nuclear collisions is small compared to the electronic energy loss because of the mass ratio factor, m_e/m_i , and for projectile energies above $0.1 \div 1 \text{ MeV}/u$ it can be neglected (Fig.2.1). Therefore, the energy transfer to the target electrons is the dominating mechanism of the projectile energy loss in this energy region.

The energy loss of projectile particles to electrons may be separated into two parts, namely, energy loss due to the bound electrons and the energy loss due to the free electrons. The first process is called cold stopping whereas the latter is important when slowing down of an ion beam takes place in a pre-ionized (hot) material, such as plasma (plasma effects). Theoretical aspects of the cold electronic stopping will be addressed in the following section while the stopping power of hot matter due to free electron contribution is not described here, but can be found in reference literature [Jac95, Oga01].

2.1.1 Stopping power in cold matter

The theory of cold electronic stopping has been developed in many parts, since there are many physical processes which must be included in a complete description of the energy loss. Numerous review articles on this subject have been published over the past decades [Sch97, Sig98, Wei00, Wea02]. Theoretical and experimental papers on this subject are still being published [Sch98, Zhu00, Sig02], indicating that this field of research is still developing and attracting serious attention. In this section the theoretical aspects of these physical phenomena will be briefly addressed on a qualitative basis.

The overall form of an expression describing the electronic energy loss of an ion in a medium can be obtained from classical arguments [Jac75], considering the momentum transfer to a target electron in a Coulomb potential, or by integrating the differential Rutherford scattering cross section [Rut11]:

$$S = n_e \cdot \int d\sigma \cdot \Delta E$$

In SI units this expression for stopping power S can be written as:

$$S \equiv -\frac{dE}{dx} = \frac{e^4}{4\pi\epsilon_0^2} \cdot \frac{\overline{Z}_p^2 \cdot n_e^{bound}}{m_e \cdot v^2} \cdot L \quad (2.1)$$

Here \bar{Z}_p is the average charge of the projectile ion (in case of bare ions $\bar{Z}_p = Z_p$; where Z_p is the atomic number), $v = \beta \cdot c$ is the ion velocity, m_e and n_e^{bound} are the electron mass and number density of bound electrons, respectively. The minus sign on the left-hand side indicates that the formula gives the energy lost by the particle. The factor L is the so-called stopping logarithm or stopping number. This factor appears from integrating the Rutherford cross section over all impact parameters. Since the integrated Rutherford cross section is diverging for infinite impact parameters, the limiting value of b_{max} has to be chosen. Therefore the stopping logarithm is defined classically by:

$$L = \ln \left(\frac{b_{max}}{b_{min}} \right) \quad (2.2)$$

where b_{max} and b_{min} are the maximum and minimum impact parameters, respectively.

Qualitatively, the behavior of the stopping power as a function of ion energy is as follows. Starting from very low energies the stopping power is rapidly increasing with the increase in projectile velocity. When the velocity of the ion approaches the average orbital velocities of the target electrons, the momentum transfer is most efficient and the stopping power curve has a maximum at about $1 \div 10 \text{ MeV/u}$ (Fig.2.1). This velocity can be compared with the Tomas-Fermi estimate for the mean electron orbital velocity:

$$v_{TF} = Z_t^{2/3} \cdot v_0$$

where $v_0 = \frac{e^2}{4\pi\epsilon_0\hbar} = \alpha \cdot c$ – is the Bohr velocity, $\alpha \approx 1/137$ is the usual fine-structure constant and c is the speed of light in vacuum. At higher energies ($v > v_{TF}$) the electronic stopping power is decreasing again as:

$$S \propto v^{-2\mu} \quad \text{where } \mu \approx 0,6 \div 0,8.$$

At the ultra-relativistic limit of the projectile velocities ($E_0 \geq 100 \text{ MeV/u}$) the stopping power becomes energy independent due to the relativistic “finite nuclear size” effect which efficiently reduces the stopping number for ultra-relativistic energies [Lin96]. A typical $S(E)$ function for both electronic and nuclear components is plotted in Fig. 2.1 for a wide energy range in logarithmic scale.

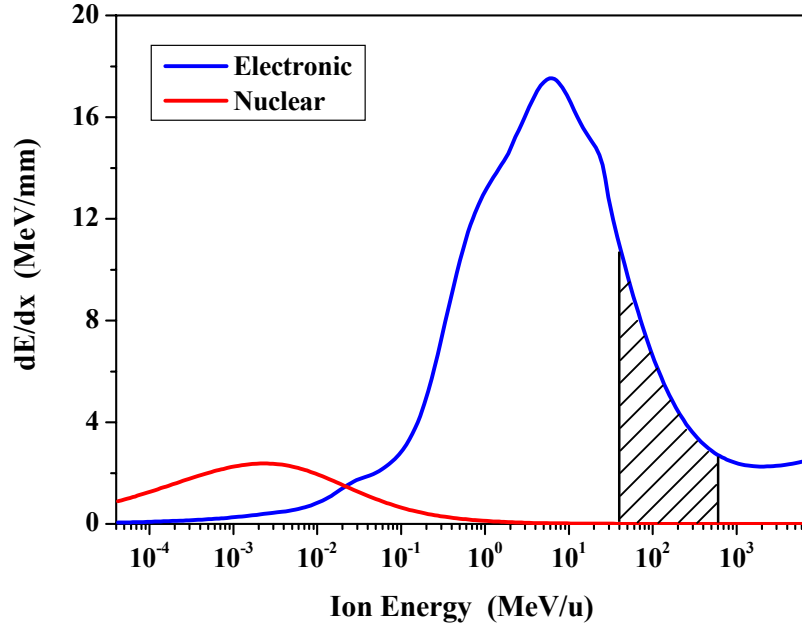


Figure 2.1: Electronic and nuclear energy losses of ^{238}U ions in 1 bar Ar gas over a wide energy range calculated with SRIM code. The energy region ($30 < E_0 < 500 \text{ MeV/u}$) is marked.

The penetration depth of an ion with initial energy E_0 in a medium until it is completely stopped is called the range. The range is related to the stopping power of the medium as:

$$R(E_0) = \int_0^{E_0} S^{-1} \cdot dE \quad (2.3)$$

If the stopping power $S(E)$ given by Equation 2.1 is known, a simple integration should yield the range as a function of the initial ion energy, E_0 . For sufficiently large energies the range-energy dependence can be approximated by a simple power relation: $R \propto E^{\mu+1}$

Specific energy loss of an ion as a function of its penetration depth in the target, $S(x)$ or the energy deposition profile can also be calculated by integrating equation (Equ.2.1), provided the stopping power is known:

$$S(x) \propto S(E(x))$$

where the energy of the ion E at the depth x can be obtained from:

$$x = \int_E^{E_0} \frac{dE'}{S}$$

The dependence $S(x)$ is called Bragg-curve. The specific energy loss $S(x)$ is increasing with the penetration depth until $x \approx R(E_0)$ where it has a characteristic sharp maximum, called the Bragg-peak and where an ion deposits the rest of its energy and is stopped.

If the initial energy of a heavy ion is below 1 MeV/u the charge exchange between the projectile ion and the target media becomes important. These effects are most pronounced for the heaviest ions: a uranium ion with the energy of several hundred MeV per nucleon still carries a few electrons while penetrating through matter. The equilibrium charge state of a heavy ion beam during the slowing down in a media will be changing from $\bar{Z}_p = Z_p$ at sufficiently high initial energies down to $\bar{Z}_p \approx 0$ near to the stopping maximum. Since the stopping power S scales with Z^2 , the charge-changing processes affect the stopping power significantly [Var02].

2.1.2 Calculation of “cold” stopping

For practical calculations of the cold stopping for heavy ions one of the available computer codes can be used. Two of the widely used codes and models: SRIM and ATIMA, which have been used for the experiment design (Chapter 3), are briefly described below.

SRIM:

The SRIM code designed by Ziegler is one of the most universal codes for stopping and range calculations in the world. Ziegler's stopping model [Zie03] is similar to that described above in this section for the intermediate energy region, although a number of advanced models for low (keV per nucleon) energy region are employed in the code to provide a good accuracy for low ion velocities. This makes using the SRIM popular especially in applied sciences and industry where precise knowledge about the ion ranges and details of the stopping near the Bragg peak are important. In addition, a Monte-Carlo code by the same authors, called TRIM, is able to calculate most of the details in the slowing down of low-energy ions (more detailed description of SRIM and TRIM codes is given in Chapter 3).

ATIMA:

The ATIMA code [ATIM] has been developed at GSI-Darmstadt to benchmark different stopping and charge-exchange theories against a large set of experimental data on slowing down of relativistic heavy ions, obtained

mostly at the fragment separator installation (FRS) at GSI. This code is widely used at GSI for preparation and calibration of nuclear physics experiments performed at the FRS. In the low-energy region the code is based on the Ziegler model [Zie03], whereas Lindhard and Sørensen theory [Lin96] is used for the high energy region. In addition to that, the code contains procedures permitting to calculate the evolution of the charge state distribution for bare (up to three electrons) heavy ions. The stopping power and ranges of heavy ions in the intermediate energy region calculated by ATIMA are in good agreement with SRIM calculations, except for the low energies around $10\div 30 \text{ MeV}/u$, which is simply an interpolation region between low- and high-energy stopping models in the ATIMA code.

The results of the stopping power calculations using modern computer codes (like SRIM and ATIMA) even for the heaviest ions such as uranium in the intermediate energy region from about $30 \text{ MeV}/u$ to $500 \text{ MeV}/u$ are in good agreement with each other and with available experimental data, especially for such frequently-studied target materials as plastic scintillators and emulsions. However, it is to be noted that this is not the case for other energy regions, such as at low projectile velocities (below the Bragg-peak) as well as at ultrarelativistic velocities.

It can be concluded that the deviations in the stopping power and ranges among different calculations and experiments in this energy region ($30\div 500 \text{ MeV}/u$) are usually not more than $\pm 2\%$. In the present work the SRIM and TRIM code were used for calculations of the stopping power, range-energy relation and ion beam straggling in the target material.

2.1.3 Energy deposition by the ion beam

In previous discussions it was implicitly assumed that there is no influence of the incident beam on the target. However, the energy that the beam ions lose resides in the target. In case of an intense beam and especially, an intense beam focused to a small (sub-millimeter) spot in a target, the amount of energy deposited by the beam in the target volume can modify matter properties significantly. Macroscopic amounts of the target material can be heated to high ($10^3\div 10^5 \text{ K}$) temperatures leading to a high energy density state. Matter in this state can have solid and super-solid densities and pressures in the range of megabars. The characteristic target properties therefore change dramatically: thermo-physical and hydro-dynamical effects such as phase transitions, penetration of shock and compression waves become

important. Matter under such extreme conditions is of special interest to many branches of pure and applied sciences including astrophysics, planetary sciences, inertial fusion energy research and physics of dense non-ideal plasmas [Var02].

In the present work the requirements for the ion beam spot size (Chapter 3) are softer (a few millimeters) because to reach high energy density states in matter was not a goal of the experiment. Nevertheless some materials (entrance window, cavity mirror and scintillator) supposed to be pierced by the heavy ion beam, and therefore could be heated to temperatures of several hundreds K (Chapter 3). This could cause destruction or damage. So it is important to take the heating power of the beam into consideration in order to choose proper parameters.

A relevant quantity to characterize the heating of matter by an intense heavy ion beam is the “specific deposited energy”, ε . This quantity gives the amount of energy deposited by the beam per unit mass of the target material, i.e. expresses the capability of a heavy ion beam to heat the matter. The specific deposited energy can be estimated using the following formula [Jac95]:

$$\varepsilon = \frac{S(E) \cdot N}{S_{beam} \cdot \rho} \quad (2.4)$$

where: N – number of ions in the beam,

S_{beam} – beam spot size

$S(E)$ – is the stopping power of the material with density ρ to the ions of energy E

This formula gives exact values of the specific energy deposition (ε usually measured in units: J/g) only for the case of instantaneous heating and a uniform transverse intensity distribution of the beam. In other cases $\varepsilon = \varepsilon(x;t)$, and Equation 2.4 should be used only for rough estimations.

2.2 Rare gas halogen excimers

Excimer molecules are excited molecules which form stable chemical bonds only in excited states. Any two-atomic molecule, one of the atom of which has a closed electronic shell, belongs to a class of excimer molecules [Smi83]. In the ground state of such system an exchange interaction between atoms, corresponding to the overlap of electron shells, is usually repulsive.

Thus, chemical bond in the ground state of the molecule is absent; however, it can appear via excitation of the closed shell atom. Thereby, the class of excimer systems is quite wide, it includes all kinds of dimer molecules which contain an atom of rare gas, dimers formed by two elements of Group II and element of Group II and alkali, as well as polyatomic molecules [Bra84].

The concept of bound-free excimer system as a laser medium was initially enunciated in 1960 [Hou60]. However, the first successful laboratory demonstrations were accomplished only at the beginning of the 1970-s [Bas70]. Further theoretical and experimental investigations have shown that the most promising candidates for a laser medium are two classes of excimer molecules: rare gas dimers and rare gas halides. Since the present work has been carried out with KrF^* excimers, the main features of the electron structure, reaction kinetics and spectroscopy of such excimer systems are considered on the example of this particular molecule.

In the rare gas halide lasers as a working medium usually a mixture of an excimer gas (heavy rare gas with small part of halogen premixed) and a buffer gas (light rare gas) is used in the ratio of 1 to 20. For example, the typical KrF^* laser mixture consists of Ar gas containing about 5% of Kr and 0,2% of F_2 premixed [Bra84]. This is connected with energy transfer and kinetic processes in the gas mixture and it will be discussed below in this chapter.

2.2.1 Electronic structure and binding parameters

In the ground state the atom of the rare gas has a closed electronic shell and thereby it does not chemically react with ground states of any other elements (atoms or molecules). But in the lowest excited state the rare gas atom has the same structure as an alkali metal. Indeed, the excited electron for this state of the rare gas atom occupies an S-orbital as the valence electron of an alkali metal. Thus it can form a strong chemical bond with a halogen atom.

The ionization potential of rare gas atoms in the lowest excited states is similar to the energy of the electron affinity² of halogen atoms [Smi83]. For instance, the lowest ionization energy of the excited Kr atom (in the state 1P_1) is **3,36 eV**, and the energy of the electron affinity for a fluorine atom is **3,40 eV** [Rad80]. In compliance with that, rare gas halides excimer molecules

² The electron affinity of an atom is the energy required to detach an electron from a singly charged negative ion.

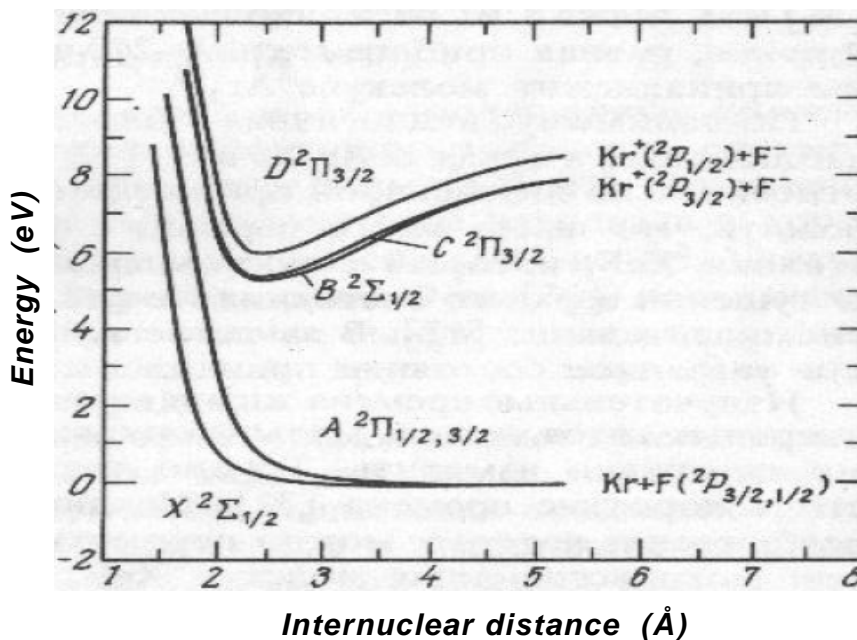


Figure 2.2: Potential energy diagram of KrF^* molecule [Bra84]

form a strong ionic bond so that the excited electron of the rare gas atom is partially transferred to the halogen atom.

In Figure 2.2 the electronic terms of the KrF^* excimer molecule are shown [Dun76, Hay77, Dun78]. In such molecules, in which the rare gas atom has a high atomic number, the excited state manifold is complicated by spin-orbit effects since the 2P rare gas ion state is split by spin-orbit coupling. The effects of this coupling one can see in Fig.2.2. The result of spin-orbit coupling is to split the $^2\Pi$ state into states with total axial angular momentum Ω of $1/2$ and $3/2$. The $\Omega = 1/2$ component lies higher, correlating with the higher lying $^2P_{1/2}$ rare ion state, and is referred to as the **D** state. The lower lying component ($\Omega = 3/2$) is referred to as the **C** state.

The laser transition in KrF^* is represented by the **B**→**X** band at $\lambda = 248$ nm. Parameters of the potential well of the **B** state are the following: a potential well depth D_e is around **5,3 eV** and the internuclear distance r_m corresponding to it is about **2,4 Å** [Dun76, Hay77, Tel76].

2.2.2 Spectroscopy and radiative parameters

The emission spectrum of the rare gas halides consists of several bands (Fig.2.3). The strongest band is assigned to the **B**→**X** transition ($^2\Sigma^+ \rightarrow ^2\Sigma^+$) and it is used as a laser transition. At high gas pressures this emission band is structured with successive peaks due to higher vibrational levels of the upper

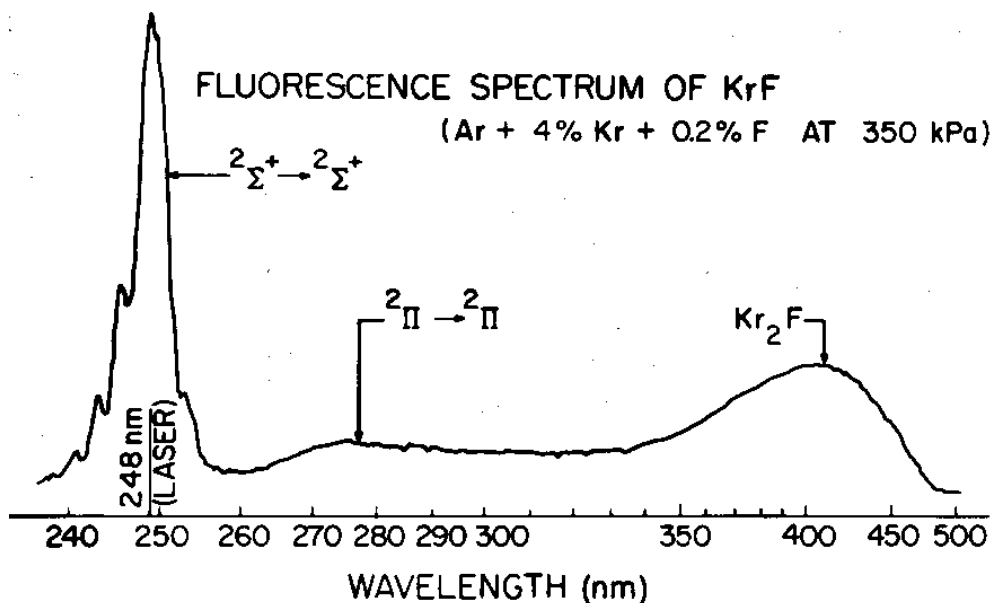


Figure 2.3: Fluorescent spectrum of Ar/Kr/F₂ laser gas mixture [Bra84].

electronic state [Ewi75, Bra75]. At low pressures the vibrational structure becomes smeared out and the band shifts to the blue [Gol75, Vel75]. This is due to emission from higher vibrational levels, which are not relaxed to lower levels at high gas pressures.

The fluorescence spectrum of the typical KrF* laser gas mixture (Ar + 4% Kr + 0,2% F) at a pressure of about 3,5 bar is shown on the Figure 2.3. The $B \rightarrow X$ transition is a strong sharp band with a central wavelength λ_c of 248 nm. The broad continuum which lies to the red of it with λ_c at about 275 nm corresponds to $C \rightarrow A$ and $D \rightarrow A$ transitions (${}^2\Pi \rightarrow {}^2\Pi$) to the repulsive lower electronic state. The broad continuum centered near 400 nm corresponds to an emission from triatomic Kr₂F* molecules. The experimental evidence supporting the identification of this band as Kr₂F* emission is the observation that this band becomes relatively strong, compared with the $B \rightarrow X$ band, as the pressure is increased [Nak76, Man77].

A radiative lifetime of the upper state is one of the most important parameters for excimer lasers. For KrF* it was investigated experimentally using different techniques: electron impact, excitation by photolytic source [Qui78b] and photodissociation of KrF₂ [Bur77, Tie90]. The lifetime of KrF* measured by these methods is about 9 ns, which is in good agreement with the theoretical value of 6,7 ns [Dun76, Hay77, Dun78].

Another parameter of central significance for lasers is the stimulated emission cross section σ_{st} . In addition to the lifetime, it depends on the shape and width of the emission band. For the $B \rightarrow X$ band of KrF^* the individual rotation-vibration lines overlap sufficiently strongly to be regarded as continua with no structure beyond (Fig.2.3). In the work of J.Tellinghuisen et al. [Tel76] careful analysis of the $B \rightarrow X$ bands of several excimer molecules including KrF^* has provided values of the product of the gain cross section and the lifetime for considered molecules. For KrF^* this value was amounted **17 ns·Å²**.

By assuming that near the peak the $B \rightarrow X$ band shape is approximately Gaussian, one could estimate the cross section-lifetime product using the formula [Bra84]:

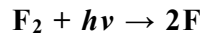
$$\sigma_{st} \cdot \tau = \frac{1}{4\pi} \cdot \left(\frac{\ln 2}{\pi} \right)^{1/2} \cdot \frac{\lambda^4}{c \cdot \Delta\lambda} \quad (2.5)$$

where: λ – central wavelength of the band,
 $\Delta\lambda$ – full width on a half maximum of the band,
 c – speed of light.

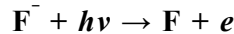
The effective width (FWHM) of the $B \rightarrow X$ band in KrF^* is about **2 nm** [Bra75], so the product of σ_{st} and τ estimated in this way is about **25 ns·Å²** which is in good agreement with the more accurate value of **17 ns·Å²** [Tel76]. Together with the measured lifetime of **9 ns**, the later value corresponds to a stimulated emission cross section σ_{st} of **2·10⁻¹⁶ cm²**.

A big role for excimer lasers is played by various photoabsorption processes at the laser wavelength in rare gas halides plasmas. The most important of them are the following:

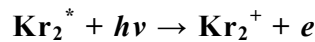
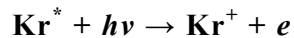
– *photodissociation of the halogen molecule:*



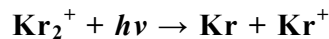
– *photodetachment of negative ions, formed in the plasma:*



– *photoionization of excited rare gas atoms and molecules:*



– *photodissociation of rare gas dimer ions:*



(the rates of these reactions as well as corresponded references are given in a Table 2.1). Photoabsorption by halogen molecules has been measured in the visible and near UV down to about 220 nm [Ste56, See64], and this could be a problem for a KrF^* laser. However, this problem could be avoided by using NF_3 , SF_6 or N_2F_4 in place of F_2 in the laser gas mixture [Bha76, Ish77, And77], but the performance will be reduced by unfavorable kinetics [Bra84]. The rare gas trimers, like Kr_2F^* and Ar_2F^* , may also absorb at the laser wavelength. Since these molecules are essentially ionic complex ($\text{Kr}_2^+ \cdot \text{F}^-$ and $\text{Ar}_2^+ \cdot \text{F}^-$), the absorption will be similar to rare gas dimer ions and halogen negative ions [Haw77].

2.2.3 Formation and quenching

During the propagation through a laser medium, the heavy ion beam creates a huge number of high energy secondary electrons, which efficiently induce ionization and excitation in the laser gas. About two thirds of the energy loss of ions is transferred into kinetic energy of the secondary electrons [Gro80, Bec96, Lac06]. The energy distribution function of the secondary electrons is inversely as the square of electron energy ($\sim \frac{1}{E^2}$) approaching a certain limit in low energy part (below 20 eV) [Bec96, Kra07]. The limit for maximum electron energy can be estimated from the mass and energy of the primary ion (see Chapter 5, Equ.5.4).

The main role in formation of excimer molecules is played not by primary ion beam, but by secondary electrons. There are two basic channels (branches) of formation of rare gas halides: neutral channel and ionic channel (as it is shown in a Fig.2.5 on the example of KrF^* excimer molecule) [Joh80, Mor81]. The reaction kinetics of the rare gas halide lasers however are rather complex, involving several ground state atomic and molecular species, several ionic species, and a large number of excited atomic and molecular species (Tab.2.1). Thus rare gas halides could be characterized as molecules with several entrance channels.

The formation of KrF^* states is via three main reactions:

- transfer of the outermost electron of the excited Kr atom to a halogen molecule and forming an ionic bond (“harpooning” reaction):



- replacement reaction:

$$ArF^* + Kr \rightarrow KrF^* + Ar \quad (\text{reac. 2 in Tab.2.1})$$
- neutralization reaction of Kr^+ and F^- ions in a three body interaction:

$$Kr^+ + F^- + M \rightarrow KrF^* + M \quad (\text{reac. 3 in Tab.2.1})^3.$$

The harpooning reaction is the strongest formation channel of KrF^* molecules since it requires only the excitation of Kr atoms. The excited atoms are initially formed in many excited states, at high pressures most of these states are rapidly quenched to lower states, so that the bulk of the excitation resides in the lowest excited levels of the various atomic and molecular species [Rho74]. Thus, the various rare gas species are assumed to have only one excited state. An excited rare gas atom has an electronic structure similar to that of an alkali metal as was mentioned above, so the chemical reaction of an excited rare gas atom with a halogen molecule is analogous to the reaction of an alkali metal with a halogen molecule. Let us consider this chemical reaction in details. While the Kr^* and F_2 particles approach each other, a transition of the system from term 1 to the ionic term (term 2 which corresponds to a positive krypton ion and a negative ion of the fluorine molecule) occurs (Fig.2.4). After the transition, the particles continue their approach due to the Coulomb interaction, and at some distance a system transition to the electronic term becomes possible. The electronic term corresponds to KrF^* molecule and fluorine atom. The last transition leads to a molecule restructuring and therefore it occurs at interparticle distances comparable with molecule sizes. The character of the described process is clarified in Figure 2.4, where electronic terms of initial and final states of the system are represented. The main feature of this process is that the transition to the ionic term occurs at large distances R_c between particles (significantly more than particle sizes), when the interaction in the initial channel is relatively weak. In the KrF^* case the calculated distance R_c is about **12,8 Å** [Smi83] while the radiuses of the Kr atom and the F_2 molecule are around **0,9 Å** and **0,7 Å**, correspondingly [Jam92]. The excited Kr atom transfers its outermost electron to the fluorine molecule, establishing thereby the Coulomb interparticle interaction, which brings particles together. So by this reason such mechanism of chemical reaction is called “harpooning”. This mechanism provides large cross sections and rate constants of the reaction which could exceed corresponding gas-kinetic characteristics [Vel76].

³ In the Table 2.1 the rate constants for reactions 3, 5, 40 and 65 is expressed as effective two-body rate constant for 2 bar gas pressure.

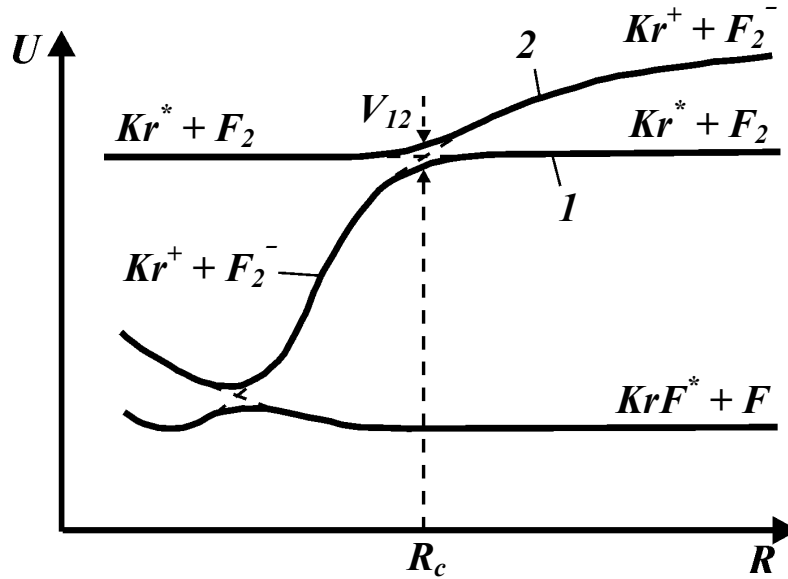


Figure 2.4: Electronic terms behavior under a chemical reaction of the excited Kr atom (Kr^) and fluorine molecule (F_2).*

In addition to the fluorine molecules, other fluorine-bearing molecules, like NF_3 or OF_2 , may be used to produce KrF^* states by the mechanism just described above [Vel76]. This is useful when it is necessary to avoid corrosive chemicals, such as F_2 , or photoabsorption of the laser radiation by the halogen species.

The mechanism for forming excited rare gas halides from ions and electrons begins with a dissociative attachment of the electrons to the halogen to form negative ions, for example:



Such reactions are effective with rate coefficients as large as $10^{-7} \text{ cm}^3 \cdot \text{s}^{-1}$ at room temperature [Bra84], but in the case of fluorine, the measured value is about $1,1 \cdot 10^{-9} \text{ cm}^3 \cdot \text{s}^{-1}$ [Man77, Che77]. Thus, in a typical KrF laser mixture (2 bar of Ar with 5% Kr and 0,2% F_2 premixed) the lifetime of an electron against attachment to fluorine molecule is on the order of 10 ns.

The dissociative attachment of an electron is followed by three-body recombination of the negative halogen ions with the positive rare gas ions, as in the following reaction:

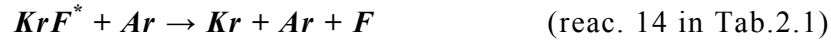


where M could be any molecule, taking away the rest of kinetic energy. In most cases this role is acted by Ar atoms, since in the typical KrF laser mixture Ar has the highest concentration (around 95%).

Just as the rare gas halides are formed by very rapid processes, they are quenched by very rapid processes as well. At low gas pressures (below 1 bar) the most important quenching process is direct quenching by the halogen-bearing species, typified by the reaction:



This reaction proceeds with a rate coefficient of $4,7 \cdot 10^{-10} \text{ cm}^3 \cdot \text{s}^{-1}$, that is, at every collision [Ede78, Man77]. Direct quenching by rare gas atoms, like in reactions:



is an order of magnitude slower. Thus, in a typical laser mixture the quenching lifetime of KrF^* molecules is on the order of 10 ns.

At high gas pressures (above 1 bar) quenching of the excited rare gas halide molecules by rare gas atoms in three-body reactions by forming triatomic excimer species, like in reactions:



becomes very important [Man77].

The species Kr_2F^* has been observed in the fluorescence spectrum of the KrF^* laser mixture (Fig.2.3), its formation reduces the intensity of the KrF^* emission. The species ArKrF^* has been observed directly by emission in Ar-Kr-Ne- F_2 mixture, it is represented as a broad band with FWHM of 65 nm centered near $\lambda = 305 \text{ nm}$ [Bra81]. The existence of ArKrF^* molecules explains the quenching of KrF^* emission and appearance of Kr_2F^* emission at high Ar pressures [Man77].

The last quenching reaction of KrF^* with forming of ArKrF^* species is followed by the very rapid exchange reaction:



Direct formation of the pure rare gas triatomics, like Kr_2F^* , is evidently quite fast, while formation of the mixed species as ArKrF^* is much (an order of magnitude) slower (Tab.2.1).

Table 2.1: Reactions and rates of various processes in an Ar-Kr-F₂ laser mixture

Pumping, quenching and stability reactions			
No	Reaction	Rate constant (s ⁻¹)	Reference
1	$\text{Kr}^* + \text{F}_2 \rightarrow \text{KrF}^* + \text{F}$	$8,1 \cdot 10^{-10} \text{ cm}^3$	[Nak76]
2	$\text{ArF}^* + \text{Kr} \rightarrow \text{KrF}^* + \text{Ar}$	$3,0 \cdot 10^{-10} \text{ cm}^3$	[Man77, Nak76]
3	$\text{Kr}^+ + \text{F}^- \rightarrow \text{KrF}^*$	$1,0 \cdot 10^{-6} \text{ cm}^3$	[Man77, Bar78]
4	$\text{Ar}^* + \text{F}_2 \rightarrow \text{ArF}^* + \text{F}$	$8,5 \cdot 10^{-10} \text{ cm}^3$	[Nak76]
5	$\text{Ar}^+ + \text{F}^- \rightarrow \text{ArF}^*$	$1,0 \cdot 10^{-6} \text{ cm}^3$	[Bar78]
6	$\text{Kr}^{**} + \text{F}_2 \rightarrow \text{KrF}^* + \text{F}$	$8,1 \cdot 10^{-10} \text{ cm}^3$	[Nak76]
7	$\text{Ar}^{**} + \text{F}_2 \rightarrow \text{ArF}^* + \text{F}$	$8,5 \cdot 10^{-10} \text{ cm}^3$	[Nak76]
8	$\text{Kr}_2^+ + \text{F}^- \rightarrow \text{KrF}^* + \text{Kr}$	$1,0 \cdot 10^{-6} \text{ cm}^3$	[Man77, Bar78, Jac78]
9	$\text{Ar}_2^+ + \text{F}^- \rightarrow \text{ArF}^* + \text{Ar}$	$1,0 \cdot 10^{-6} \text{ cm}^3$	[Man77, Bar78, Jac78]
10	$\text{ArKr}^+ + \text{F}^- \rightarrow \text{KrF}^* + \text{Ar}$	$1,0 \cdot 10^{-6} \text{ cm}^3$	[Joh80]
11	$\text{ArKr}^* + \text{F}_2 \rightarrow \text{KrF}^* + \text{Ar} + \text{F}$	$6,0 \cdot 10^{-10} \text{ cm}^3$	[Nak76]
12	$\text{KrF}^* + \text{F}_2 \rightarrow \text{Kr} + 3\text{F}$	$4,7 \cdot 10^{-10} \text{ cm}^3$	[Ede78]
13	$\text{KrF}^* + \text{Kr} \rightarrow 2\text{Kr} + \text{F}$	$2,0 \cdot 10^{-11} \text{ cm}^3$	[Nak76]
14	$\text{KrF}^* + \text{Ar} \rightarrow \text{Kr} + \text{Ar} + \text{F}$	$5,0 \cdot 10^{-12} \text{ cm}^3$	[Smi83]
15	$\text{KrF}^* + 2\text{Ar} \rightarrow \text{ArKrF}^* + \text{Ar}$	$8,0 \cdot 10^{-32} \text{ cm}^6$	[Man77, Shu77]
16	$\text{KrF}^* + 2\text{Kr} \rightarrow \text{Kr}_2\text{F}^* + \text{Kr}$	$9,7 \cdot 10^{-31} \text{ cm}^6$	[Ede78]
17	$\text{ArF}^* + 2\text{Ar} \rightarrow \text{Ar}_2\text{F}^* + \text{Ar}$	$5,0 \cdot 10^{-32} \text{ cm}^6$	[Nak76]
18	$\text{Kr} + \text{ArKrF}^* \rightarrow \text{Kr}_2\text{F}^* + \text{Ar}$	$2,0 \cdot 10^{-11} \text{ cm}^3$	[Man77]
19	$\text{Ar} + \text{ArKrF}^* \rightarrow \text{Ar}_2\text{F}^* + \text{Kr}$	$2,0 \cdot 10^{-11} \text{ cm}^3$	[Man77]
20	$\text{KrF}^* + \text{Kr} + \text{Ar} \rightarrow \text{Kr}_2\text{F}^* + \text{Ar}$	$6,5 \cdot 10^{-31} \text{ cm}^6$	[Rok78]
21	$\text{ArKrF}^* + \text{F}_2 \rightarrow \text{Ar} + \text{Kr} + \text{F} + \text{F}_2$	$1,0 \cdot 10^{-9} \text{ cm}^3$	[Nak76]
22	$\text{Kr}_2^* + \text{F}_2 \rightarrow \text{Kr}_2\text{F}^* + \text{F}$	$3,0 \cdot 10^{-10} \text{ cm}^3$	[Nak76]
23	$\text{Kr}_2^* + \text{F} \rightarrow \text{KrF}^* + \text{Kr}$	$3,0 \cdot 10^{-10} \text{ cm}^3$	[Nak76]
24	$\text{Kr}_2\text{F}^* + \text{F}_2 \rightarrow 2\text{Kr} + \text{F} + \text{F}_2$	$1,0 \cdot 10^{-9} \text{ cm}^3$	[Nak76]
25	$\text{Ar}_2^* + \text{F}_2 \rightarrow \text{Ar}_2\text{F}^* + \text{F}$	$2,5 \cdot 10^{-10} \text{ cm}^3$	[Nak76]
26	$\text{Ar}_2^* + \text{F} \rightarrow \text{ArF}^* + \text{Ar}$	$3,0 \cdot 10^{-10} \text{ cm}^3$	[Nak76]
27	$\text{Ar}_2\text{F}^* + \text{F}_2 \rightarrow 2\text{Ar} + \text{F} + \text{F}_2$	$1,0 \cdot 10^{-9} \text{ cm}^3$	[Nak76]
28	$\text{Ar}_2\text{F}^* + \text{Kr} \rightarrow \text{ArKrF}^* + \text{Ar}$	$1,0 \cdot 10^{-10} \text{ cm}^3$	[Nak76]
29	$\text{ArKr}^* + \text{Kr} \rightarrow \text{Kr}_2^* + \text{Ar}$	$1,0 \cdot 10^{-10} \text{ cm}^3$	[Nak76]
30	$\text{Kr}^* + 2\text{Ar} \rightarrow \text{ArKr}^* + \text{Ar}$	$1,0 \cdot 10^{-32} \text{ cm}^6$	[Nak76]
31	$\text{Ar}^* + \text{Kr} + \text{Ar} \rightarrow \text{ArKr}^* + \text{Ar}$	$1,0 \cdot 10^{-32} \text{ cm}^6$	[Nak76]
32	$\text{Kr}^* + \text{Kr} + \text{Ar} \rightarrow \text{Kr}_2^* + \text{Ar}$	$1,0 \cdot 10^{-32} \text{ cm}^6$	[Nak76]
33	$\text{Ar}^* + 2\text{Ar} \rightarrow \text{Ar}_2^* + \text{Ar}$	$1,14 \cdot 10^{-32} \text{ cm}^6$	[Nak76]
34	$\text{Ar}^* + \text{Kr} \rightarrow \text{Kr}^* + \text{Ar}$	$6,2 \cdot 10^{-12} \text{ cm}^3$	[Pip73, Nak76]
35	$\text{Ar}_2^* + \text{Kr} \rightarrow \text{Kr}^* + 2\text{Ar}$	$4,0 \cdot 10^{-10} \text{ cm}^3$	[Man77]
36	$\text{Ar}^+ + 2\text{Ar} \rightarrow \text{Ar}_2^+ + \text{Ar}$	$2,5 \cdot 10^{-31} \text{ cm}^6$	[McD70]
37	$\text{Ar}_2^+ + \text{Kr} \rightarrow \text{Kr}^+ + 2\text{Ar}$	$7,5 \cdot 10^{-10} \text{ cm}^3$	[Boh70]
38	$\text{Ar}^+ + \text{Kr} + \text{Ar} \rightarrow \text{ArKr}^+ + \text{Ar}$	$1,0 \cdot 10^{-31} \text{ cm}^6$	[Lac78]
39	$\text{Kr}^+ + 2\text{Ar} \rightarrow \text{ArKr}^+ + \text{Ar}$	$1,0 \cdot 10^{-31} \text{ cm}^6$	[Joh80]
40	$\text{ArKr}^+ + \text{F}^- \rightarrow \text{ArKrF}^*$	$1,0 \cdot 10^{-6} \text{ cm}^3$	[Joh80]
41	$\text{ArKr}^+ + \text{Kr} \rightarrow \text{Kr}_2^+ + \text{Ar}$	$3,2 \cdot 10^{-10} \text{ cm}^3$	[Joh80]
42	$\text{Kr}^+ + 2\text{Kr} \rightarrow \text{Kr}_2^+ + \text{Kr}$	$2,5 \cdot 10^{-31} \text{ cm}^6$	[McD70]
43	$\text{Ar}^+ + \text{Kr} \rightarrow \text{Kr}^+ + \text{Ar}$	$3,0 \cdot 10^{-11} \text{ cm}^3$	[Boh70]
44	$\text{Kr}^+ + \text{Kr} + \text{Ar} \rightarrow \text{Kr}_2^+ + \text{Ar}$	$2,5 \cdot 10^{-31} \text{ cm}^6$	[Man77, Jac78]
45	$\text{F} + \text{F} + M \rightarrow \text{F}_2 + M$	$1,0 \cdot 10^{-33} \text{ cm}^6$	[Joh80]

Table 2.1: (continued)

Electron reactions			
№	Reaction	Typical rate constant (cm ³ ·s ⁻¹)	Reference
46	ArKr ⁺ + e → Kr ^{**} + Ar	1,0·10 ⁻⁷	[Joh80]
47	F ₂ + e → F ⁻ + F	1,1·10 ⁻⁹	[Man77, Che77]
48	Kr + e → Kr [*] + e	4,1·10 ⁻¹¹	[Sha69,Egg75,Jac76b]
49	Kr [*] + e → Kr ^{**} + e	6,4·10 ⁻⁷	[Jac76a]
50	Kr + e → Kr ⁺ + 2e	1,5·10 ⁻¹⁵	[Rap65, Pet72]
51	Kr [*] + e → Kr ⁺ + 2e	4,8·10 ⁻⁸	[Vri65]
52	Kr ^{**} + e → Kr [*] + e	8,0·10 ⁻⁷	[Jac76a]
53	Kr [*] + e → Kr + e	8,0·10 ⁻¹¹	[Sha69,Egg75,Jac76b]
54	Kr ^{**} + e → Kr ⁺ + 2e	1,8·10 ⁻⁷	[Vri65]
55	Ar + e → Ar [*] + e	2,8·10 ⁻¹²	[Sha69,Egg75,Jac76b]
56	Ar [*] + e → Ar ^{**} + e	6,6·10 ⁻⁷	[Jac76a]
57	Ar + e → Ar ⁺ + 2e	1,4·10 ⁻¹⁹	[Rap65, Pet72]
58	Ar [*] + e → Ar ⁺ + 2e	2,8·10 ⁻⁸	[Vri65]
59	Ar ^{**} + e → Ar [*] + e	9,0·10 ⁻⁷	[Jac76a]
60	Ar [*] + e → Ar + e	5,4·10 ⁻¹²	[Sha69,Egg75,Jac76b]
61	Ar ^{**} + e → Ar ⁺ + 2e	1,9·10 ⁻⁷	[Vri65]
62	Kr ₂ ⁺ + e → Kr ^{**} + Kr	1,1·10 ⁻⁷	[Bio63, Che69, Bar70]
63	Ar ₂ [*] + e → Ar ^{**} + Ar	7,7·10 ⁻⁸	[Bio63, Che69, Bar70]
64	F ₂ + e → 2F + e	3,0·10 ⁻¹⁰	[Joh80]
65	F + e → F ⁻	1,0·10 ⁻¹²	[Joh80]
Radiative reactions			
№	Reaction	Rate (s ⁻¹)	Reference
66	KrF [*] → Kr + F + hν	1,5·10 ⁸	[Nak76, Dun78]
67	ArF [*] → Ar + F + hν	2,5·10 ⁸	[Dun78]
68	Kr ₂ [*] → 2Kr + hν	3,3·10 ⁶	[Nak76]
69	Ar ₂ [*] → 2Ar + hν	3,8·10 ⁶	[Nak76]
70	Kr ₂ F [*] → 2Kr + F + hν	6,7·10 ⁷	[Nak76]
71	Ar ₂ F [*] → 2Ar + F + hν	2,0·10 ⁸	[Nak76]
72	ArKr [*] → Ar + Kr + hν	3,0·10 ⁶	[Nak76]
73	ArKrF [*] → Ar + Kr + F + hν	5,0·10 ⁷	[Nak76]
Photoabsorption reactions			
№	Reaction	Cross section (cm ²)	Reference
74	F ₂ + hν → F + F	1,2·10 ⁻²⁰	[Cal66]
75	F ⁻ + hν → F + e	5,0·10 ⁻¹⁸	[Man71]
76	Kr ₂ ⁺ + hν → Kr ⁺ + Kr	1,5·10 ⁻¹⁷	[Mic78]
77	Ar ₂ ⁺ + hν → Ar ⁺ + Ar	1,0·10 ⁻¹⁷	[Mic78]
78	Ar ^{**} + hν → Ar ⁺ + e	2,3·10 ⁻¹⁸	[Joh80]
79	Kr ^{**} + hν → Kr ⁺ + e	4,5·10 ⁻¹⁸	[Joh80]
80	Ar [*] + hν → Ar ⁺ + e	1,0·10 ⁻¹⁹	[Joh80]
81	Kr [*] + hν → Kr ⁺ + e	3,2·10 ⁻²⁰	[Joh80]
82	Kr ₂ F [*] + hν → products	5,0·10 ⁻¹⁸	[Joh80]
83	Ar ₂ F [*] + hν → products	1,0·10 ⁻¹⁸	[Joh80]
84	KrF [*] + hν → Kr + F + 2hν	2,4·10 ⁻¹⁶	[Haw77]

In addition to the collision quenching by atoms and molecules of laser gas components, both excited rare gas atoms and rare gas halides can be quenched by electrons [Tra80, Pet87].

An interesting conclusion follows from the kinetic described above, that all processes of forming the excited rare gas halides begin with molecular halogen species such as F_2 , rather than atomic halogens. This suggests that oscillation should cease when the molecular halogens in the gas are consumed, since three-body recombination of halogen molecules in the rare gases is rather slow, with rate coefficients of the order of $10^{-32} \text{ cm}^6 \cdot \text{s}^{-1}$. For a typical halogen concentration of 10^{-17} cm^3 in two atmospheres of a rare gas this corresponds to a recombination time of the order of $20 \mu\text{s}$, which is long compared with the laser pulse lengths. This sets a limit on the available total laser pulse energy per unit volume corresponding to no more than one photon per initial halogen molecule.

Though reaction kinetics of rare gas halide lasers are rather complex and not completely understood at the present time, most of the reactions are well investigated and their rate constants are known. All known reactions for KrF^* laser, including pumping, quenching, stability, electron reactions as well as radiative and photoabsorption reactions, are summarized in the Table 2.1 together with measured rate constants and references on corresponding works.

Kinetics of forming and quenching of KrF^* excimer molecules in the laser gas pumped with a uranium beam is schematically shown on a Figure 2.5 with designation of the most important channels and species.

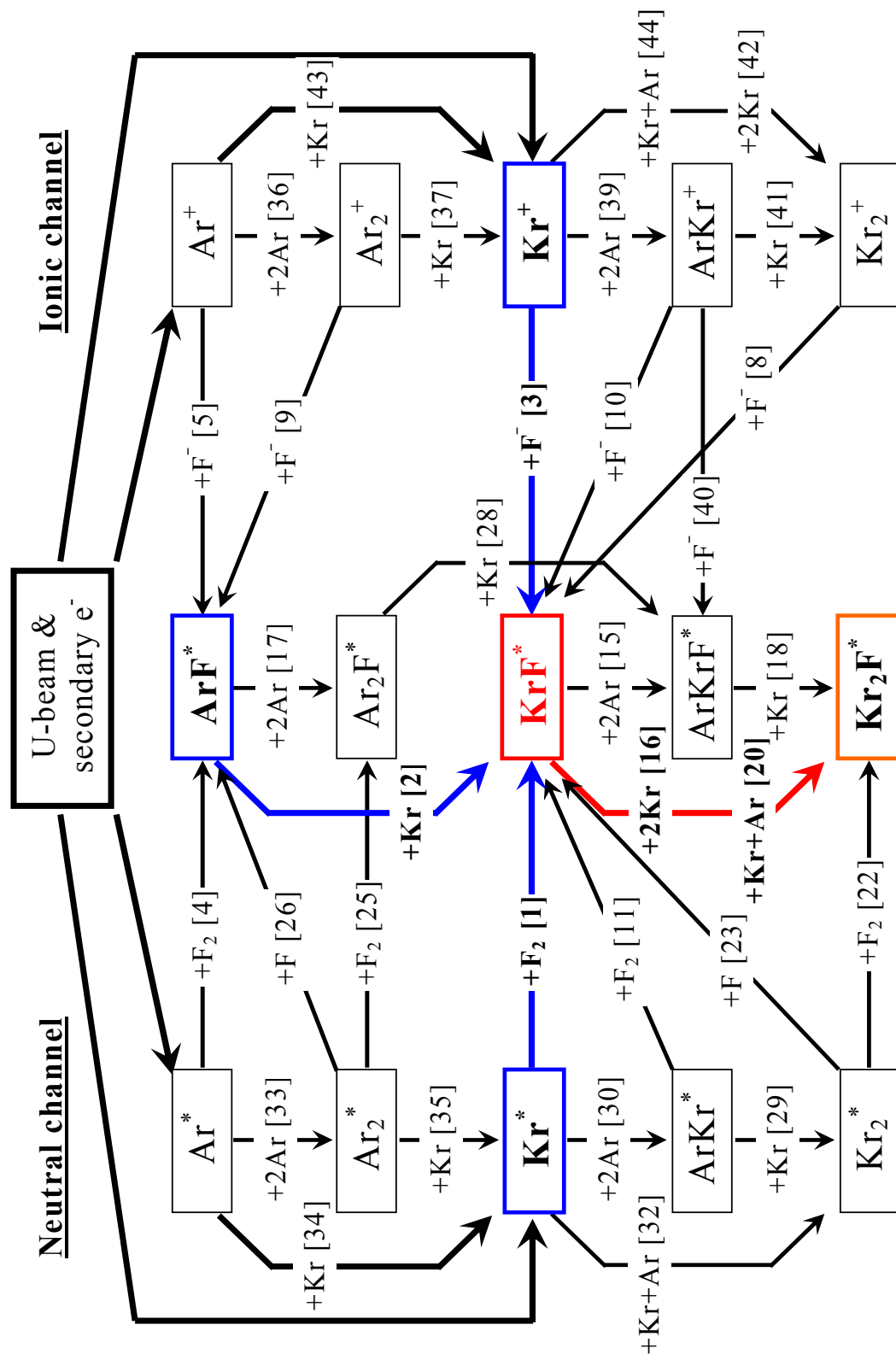


Figure 2.5: Kinetics of formation and quenching of KrF^* in Ar/Kr/ F_2 laser gas pumped with a Uranium beam (numbers in brackets correspond to reaction numbers in Table 2.1).

Chapter 3

Design of the Experiment and Numerical Predictions

This chapter is dedicated to choosing the main parameters of the experiment such as: sort of ions, initial energy of the ion beam, position and size of the beam focal spot, composition of the excimer mixture and working gas pressure range. The technical design of some parts of the setup depends strongly on the selection of these parameters. For example, optimal length of the laser cavity (distance between mirrors) depends on propagated range of ions in a gas (ion beam should not heat the output mirror) and on the parallelism of the ion beam (inside cavity it should be as parallel as possible). In turn, these parameters depend on the initial energy of ions, the laser gas composition, the gas pressure inside the cell and the transversal emittances of the ion beam. On the other hand, the length of the cavity determines the dimensions of the gas cell, curvature of output mirror, etc.

Some theoretical calculations and numerical predictions which are necessary for preparation of the experiment and the selection of its parameters will be described in this chapter as well.

3.1 Selection of the ion beam parameters

The main experimental goal is to test a heavy ion beam for pumping short wavelength lasers. There are a number of general requirements for such a laser driver:

- *high energy density deposited in the gas*
- *short interaction time*

- *high ionization ability*
- *homogeneous distribution of deposited energy along the laser axis*

The parameters of the ion beam were chosen according to these requirements.

The power density deposited in the laser medium is determined by the following characteristics of the driver: energy loss of a single particle, the number of particles in the beam pulse, the beam spot size and the pulse duration.

$$P_d = \frac{\Delta E / \Delta x \cdot I_{beam}}{S_{beam} \cdot \tau} = \left[\frac{W}{cm^3} \right] \quad (3.1)$$

- where:
- P_d – pumping power density produced by ion beam
 - $\Delta E / \Delta x$ – ion energy loss in matter
 - I_{beam} – number of particles in a beam pulse
 - S_{beam} – area of a beam spot
 - τ – duration of a beam pulse

Since ion energy loss in matter is proportional to the charge squared of the ion ($\Delta E / \Delta x \sim Z^2$), the ions should have as highest Z as possible for highest energy deposition. The ions with highest Z accelerated in the GSI facility are uranium $^{238}\text{U}^{73+}$. Maximization of the pumping power density requires also: maximum beam intensity, smallest beam spot area and shortest beam pulse duration. The maximum intensity for uranium beams in GSI achieves $3 \cdot 10^9$ particles per pulse. The duration of the ion beam is not shorter than 100 ns FWHM. Reasons for these limitations as well as a structure of the GSI accelerator facility will be described in details in Chapter 4.

For a homogeneous distribution of the pumping energy the ion beam need to be as parallel as possible along the whole laser cavity. But due to the finite values of the ion beam's transversal emittances there is a limitation for minimum reasonable area of the beam spot. An optimization of the ion beam spot size and a shape of a beam envelope will be described in the next paragraphs.

3.2 Ion beam envelope calculation

Parallelism of the ion beam is determined by values of transversal emittances ε_x and ε_y and by the beam's spot size in a waist. The transversal

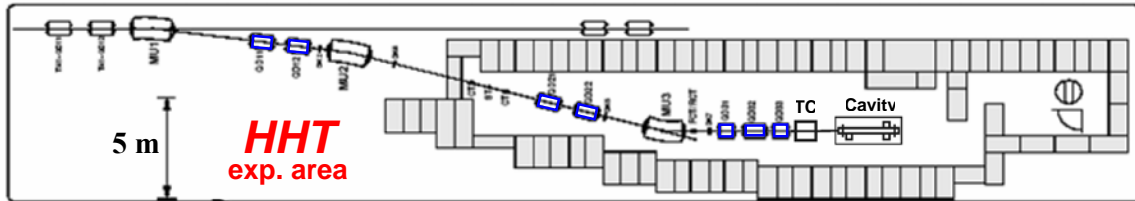


Figure 3.1: Scheme of the ion beamline in the HHT experimental area (quadrupole magnets marked in blue).

emittance of the ion beam is generally defined by the following factors [Do105]:

- geometry and type of the ion source
- final ion energy after acceleration
- collimation systems in the synchrotron and transfer line

For the multi-multiturn injection scheme, which was used for accumulating of a maximum number of ions in SIS-18, the initial emittances of the beam at injection energy into SIS-18 of $11,4 \text{ MeV}/u$ for all species of ions are determined by a full acceptance of the synchrotron. After acceleration up to $300 \text{ MeV}/u$ beam emittances are reduced several times. The typical values for an uncooled uranium beams are:

$$\varepsilon_x = 40\pi \text{ mm}\cdot\text{mrad} \text{ (horizontal)} \text{ and } \varepsilon_y = 10\pi \text{ mm}\cdot\text{mrad} \text{ (vertical).}$$

Applying an “electron cooling” technique on the SIS-18 before acceleration allows reducing the final emittances of the ion beam by one order of magnitude [Do105, Ste05].

Knowing the transversal emittances (ε_x and ε_y) of the beam one can calculate a minimum achievable beam spot size in the waist and a beam

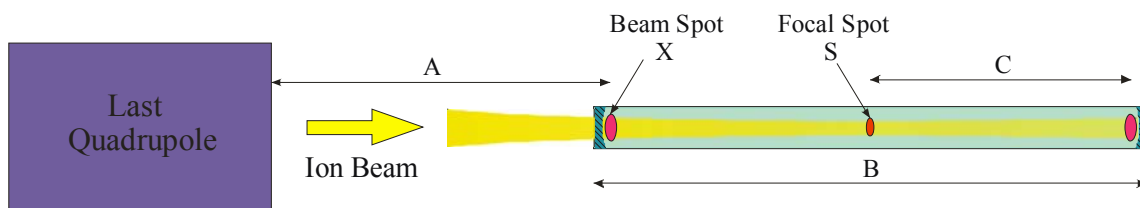


Figure 3.2: Ion beam focusing inside a laser cavity
 A – distance from the beamline to entrance of the cavity
 B – ion range inside the laser cell
 C – distance from the focal spot to the end of ions range
 S – beam spot size in the focal point

envelope in the space. The radius of the ion beam (r_x and r_y in the case of elliptical beam) is defining by the following formula [Wie93]:

$$r_{beam} = \sqrt{\varepsilon \cdot \beta} \quad (3.2)$$

where: ε – transversal emittance of the beam
 β – β -function of an ion optical system [Bru70, Wie93]

Figure 3.1 shows a schematic outline of the HHT beamline. This beamline involves seven quadrupole magnets: two duplets (QD11–QD12 and QD21–QD22) and one triplet (QD31–QD32–QD33) directly in front of the HHT target chamber (TC). Such an arrangement allows focusing the ion beam down to sub-millimeter size in FWHM on targets inside the target chamber.

To the first order approximation, ion scattering before and inside the laser cell is neglected, maximum parallelism of the ion beam could be achieved by locating the beam waist in the middle of the resonator (as shown in Fig.3.2). In this case the largest beam spots will be near the entrance of the cavity and in the end of ions stopping range. The size of this spot (X) will depend on the size of the beam focal spot (S), beam emittances (ε_x and ε_y) and the distance from the beam waist (C).

The WinAGILE code has been used for calculating the ion beam envelope inside the laser cell as well as for determining the magnet settings required for achieving the necessary geometry of the beam. WinAGILE is an interactive code dedicated to the alternating-gradient lattice design of synchrotron rings and transfer lines [WinA]. The HHT beamline was represented as a transfer

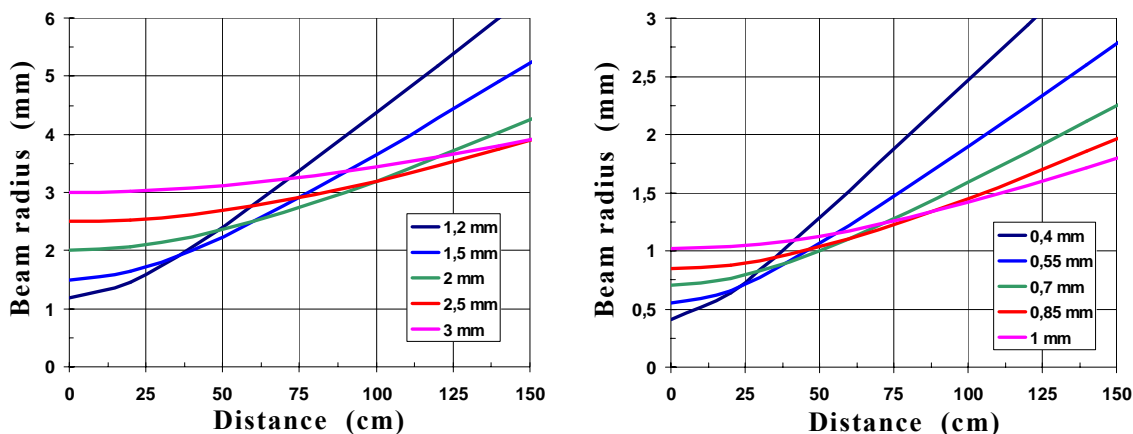


Figure 3.3: Behaviour of the ion beam envelope for different beam radii in the focal spot (in Horizontal plane – on the left and in Vertical plane – on the right).

line with more than 80 lattice elements including the magnets, diagnostics and intermediate drift distances.

Using WinAGILE code the β -functions of an ion optical system of the HHT beamline were matched to the desired values in a beam waist. The position of the beam waist was fixed at a distance of 2,5 m from the last quadrupole magnet of the beamline, which corresponds to the middle of the laser cell. The desired values for the β -functions were varied in order to obtain the different values for the ion beam radiuses in a range $1,2 \div 3$ mm for r_x and $0,4 \div 1$ mm for r_y (Fig.3.3). The matching process was performed by varying the magnet strength of the last five quadruples of the HHT beamline (Fig.3.1).

The larger the beam spot in the focus and the shorter length of the laser cell, the more parallel is the ion beam shape inside the cell. The Fig.3.3 shows how the beam envelope twists with decreasing beam focal spot size. Since the vertical emittance (ϵ_y) is approximately four times smaller than horizontal one (ϵ_x), it is reasonable to use an elliptical shape of the ion beam, elongated in the horizontal plane.

Before the most appropriate length of the laser resonator and the ion beam size will be chosen, it is necessary to determine how essential the divergence of the beam due to the ions scattering will be. An answer on this question is given in the next paragraph.

3.3 Selection of an entrance window to the laser cell

The entrance window of the gas cell will be used to be pierced by the heavy ion beam. At the same time it is supposed to withstand a high pressure (up to 10 bar) of the gas mixture containing Fluorine. These facts led to several important requirements for the windows material and thickness. Firstly, the material of the window should be chemically stable to pure halogens (F_2 , Cl_2 , etc.), their acids (HF , HCl , etc.)⁴ and, what is most dangerous, halogen radicals (F^\pm , Cl^\pm , etc.)⁵. Secondly, the mechanical stability of the material at minimum thickness has to be obtained. Thirdly, the window material has to be stable to ionizing (hard) radiation, such as neutrons, γ -rays, etc., and keep its mechanical properties during the heating by the ion beam. And finally, the window is supposed to be as thin as possible and have a

⁴ Even after multi-step evacuating of the gas cell there will be a certain part of water molecules inside which interacting with halogens will form acids.

⁵ After propagation of the ion beam through the gas they will be present as well.

material density as low as possible in order to reduce the energy loss of the ion beam and the beam angular straggling due to ions scattering.

In compliance with the requirements listed above the following materials were considered for the entrance window: Kapton, Teflon, Tantalum and Stainless Steel. In Table 3.1 the most important characteristics and properties of these materials are listed [Good, Jam92].

Teflon and Tantalum were ruled out. Teflon has very doubtful mechanical properties and a narrow working temperature interval. Tantalum has a very high density, which will cause high energy losses of the ions and large beam straggling.

Table 3.1: Comparison of physical properties of different materials for an entrance window.

Materials	Kapton (H-10,C-22,N-2,O-5)	Teflon (C-2, F-4)	Tantalum (Ta)	Stainless Steel (Fe/Cr18/Ni10)
Density, ρ (g/cm^3)	1,42	2,2	16,6	7,93
Melting point or max. working temp., T_m ($^{\circ}\text{C}$)	400	300	2996	1400
Specific heat, c ($^{\circ}\text{J}/\text{K}\cdot\text{g}$)	1,09	1,172	0,14	0,5
Thermal conductivity, λ ($^{\circ}\text{W}/\text{m}\cdot\text{K}$)	0,12	0,195	57,5	16,3
Tensile strength, (MPa)	231	21	485	460
Fluorine Resistance	Good	Excellent	Excellent	Good

A kapton foil of 125 μm thickness and 40 mm diameter as well as a stainless steel foil of 50 μm thickness and the same diameter have been successfully tested with 15 bar pressure in the material science laboratory at GSI [Der05]. Both materials have a very good resistance with respect to corrosion by strong chemical reagents like halogens and acids. A more difficult question is, how these materials would perform under extreme conditions during the heavy ion beam heating and could they retain the mechanical properties to keep a high pressure. Another question is, the limitation for ion beam parameters when it is still safe to use these materials as entrance window.

To get an answer to these questions the most extreme parameters of the ion beam, which could be reached during the experiment, were considered: heaviest ion species – Uranium, maximum beam intensity – $4 \cdot 10^9$ particles per bunch [Var04], minimum beam spot size – 0,05 cm^2 (this could occur only

accidentally during beam alignment. The planned working spot size on the window is larger than 0,2 cm²). The energy deposited in the material in this case will be calculated by the formula given below (Equ.3.3) [Jac95].

$$\mathcal{E}_{\max} = \frac{\frac{\partial E}{\partial x} \cdot I_{\max}}{S_{\min} \cdot \rho} \quad (3.3)$$

Using the specific heat of the material it is easy to get a maximum temperature increase for a single shot of the ion beam:

$$\Delta T_{\max} = \frac{\mathcal{E}}{c} \quad (3.4)$$

Results of these calculations for Kapton and Stainless Steel are given in Table 3.2.

Table 3.2: Comparison of materials for entrance window in conditions under uranium beam with initial ion energy of 250 MeV/u at max. intensity and min. beam spot size.

Window material	Kapton	Stainless Steel
Thickness, d (μm)	125	50
Stopping power, dE/dx (GeV/mm)	4,03	17,30
Ions energy lost in window, ΔE (GeV)	0,5	0,87
Max. specific deposited energy, ϵ (J/g)	364	280
Max. temperature increasing per single shot, ΔT_{\max} (K)	335	560

Kapton reaches a temperature very close to its maximum working temperature and in addition the kapton tensile strength will reduce in more than two times. Stainless steel at less than 600°C has almost the same mechanical properties as at room temperature. A stainless steel foil of 50 μm thickness is therefore a good choice for the entrance window to the laser cavity.

3.4 Ion beam stopping in the gas mixture

For calculating the stopping power of heavy ions in cold matter the SRIM code has been used. SRIM (Stopping and Range of Ions in Matter) is a group of programs which calculates the stopping and range of ions (in an energy

region from 10 eV per ion up to 2 GeV per nucleon) in matter using a quantum mechanical treatment of ion-atom collisions. During interaction, the ion and atom have a screened Coulomb collision, including exchange and correlation interactions between the overlapping electron shells. The ion also has long range interactions with target atoms creating electron excitations and plasmons within the target. These features are described by including a description of the target's collective electronic structure and interatomic bond structure when the calculation is set up. The charge-state of the ion within the target is described using the concept of effective charge, which includes a velocity dependent charge state and long range screening due to the collective electron sea of the target [Zie03].

Before the heavy ion beam can reach the laser cavity, it has to propagate through a set of various materials. It exits the beamline through a thin (150 μm) Al-foil, traverses a wide (210 cm) layer of air between the beamline and the laser installation, passes through an Al_2O_3 scintillator (600 μm), enters to the gas cell through the stainless steel window (50 μm) and, finally, goes through a first resonator mirror made from fused silica (3,175 mm).

In Tab.3.3 the energy loss of Uranium ions in the various materials on the way to laser resonator is listed for different initial ion energies. The initial energy of ions is one of the beam parameters which could be varied, therefore it is important to choose the most suitable one.

Table 3.3: Energy loss of U-ions in intermediate materials after exiting the beamline and before entering the laser cavity.

Propagated Material	Thickness	Ion Energy after propagation (GeV)			
		200 MeV/u 47,6 GeV	250 MeV/u 59,5 GeV	300 MeV/u 71,4 GeV	350 MeV/u 83,3 GeV
beamline exit Al-window	150 μm	46,50	58,52	70,51	82,47
air drift	210 cm	37,61	50,84	63,61	76,35
Al_2O_3 -scintillator	600 μm	29,79	44,24	57,75	70,99
stainless steel pressure window	50 μm	28,52	43,22	56,87	70,20
entrance quartz mirror	3,175 mm	0	16,89	35,30	51,54
<hr/>					
Ion energy at the entry of the cavity		–	16,89 GeV	35,30 GeV	51,54 GeV

As can be seen from Tab.3.3 “the lion’s share” of the ions energy is lost in intermediate materials. Only the remaining energy is used for pumping the laser medium. This energy, obviously, depends on the initial ion energy and

amounts: 62%, 49% and 28% for primary 350 MeV/u , 300 MeV/u and 250 MeV/u , correspondingly. For an initial energy of 200 MeV/u the rest is even zero because all ions are stopped in the entrance mirror of the cavity.

Calculations of the ion beam straggling in the intermediate materials before entering the laser cavity as well as in the laser gas mixture inside the cavity have been performed using the TRIM code. TRIM (the Transport of Ions in Matter) is the most comprehensive program included in the SRIM software [Zie03]. It is a Monte-Carlo calculation which follows the ion through the target, making detailed calculations of the energy transferred to every target atom collision. Using TRIM one can calculate complex targets made of compound materials with up to eight layers, each of different material. The material library of SRIM software is very wide; in addition to all chemical elements it consists more than 240 compound materials including various gases, liquids, metal alloys, plastics, polymers, implantation compounds (like glass, quartz, etc.), biological (like bone, skin, muscle, etc.) and nuclear physics materials (various scintillators and crystals used in detectors). TRIM allows calculating both the final 3D distribution of the ions and also all kinetic phenomena associated with the ion energy loss: target damage, sputtering, ionization, and phonon production.

The straggling of the ion beam due to ion collisions and scattering on atoms of the intermediate materials on the way to the laser cavity is shown in Tab.3.4. Each intermediate material was added to the TRIM as a separate target layer with certain width and density. Calculations were performed for three different initial particle energies: 59,5 GeV, 71,4 GeV and 83,3 GeV which corresponds to 250, 300 and 350 MeV/u . In each case the accumulated statistics was 500 ions. As resulting beam parameters, beam radius and angular spread have been obtained which were valid for more than 90% of particles.

Table 3.4: Ion beam parameters after propagation through all intermediate materials for different initial energies of ions.

Initial ion energy	Exit beam parameters		
	Ion energy	Beam radius	Angular spread
250 (MeV/u)	16,89 GeV	2,0 mm	0,745 °
300 (MeV/u)	35,30 GeV	1,7 mm	0,458 °
350 (MeV/u)	51,54 GeV	1,4 mm	0,344 °

In the gas cell the heavy ion beam should stop before reaching a second resonator mirror otherwise it could damage its thin multi-layer reflective coating (Chapter 4). The ion range in the laser gas should be shorter than the length of the resonator. The range depends on following parameters: initial ion energy, gas pressure inside the cell and gas composition. It was planned to use a commercial excimer laser premix: 95,5% Kr and 0,5% F₂ (this is a standard mixture used in commercial KrF-lasers) and a buffer gas (pure Ar) with different mixing ratios as a laser gas.

If we assume a length of the resonator of **1,3 m** (to be safe the range of ions should not exceed **1,2 m**) and the gas ratio of 50% of buffer gas and 50% of excimer laser premix, this will result in the following values for minimum working pressure: **0,9 bar**, **2,65 bar** and **4,7 bar** corresponding to initial ion energies of **250**, **300** and **350 MeV/u** respectively. Since the range of the ions is proportional to $\Delta E/\rho$ [Var02], the value for minimum gas pressure could be simply recalculated for any gas mixing ratio as well as for any ion range.

The blowing of the ion beam during the stopping in the laser gas for all three cases is shown in Fig.3.4. The calculation was performed using the TRIM code without taking into account the sizes of the ion beam due to the beam focusing. All intermediate materials as well as the laser gas were added

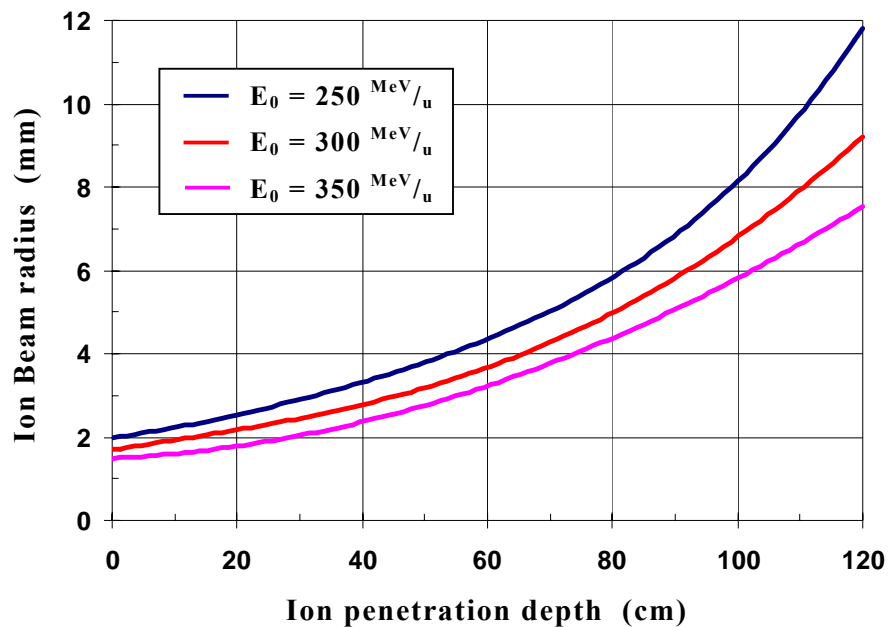


Figure 3.4: Ion beam straggling in the laser gas for the ion range of 1,2m for different ions energy and consequently different gas pressure.

to the TRIM as one multi-layer target.

The ion beam straggling in the laser gas for different penetration depths from 0 to the maximum of 120 cm with 20 cm steps were calculated by setting different thickness of the gas layer. The beam sizes for each “reference point” was concluded from the spatial distribution of the ions at the end of the layer (the size is valid for 90% of particles). The sizes between two nearest reference points was concluded from linear regression.

As can be seen from Fig.3.4 for higher ion energy the total beam straggling is smaller. But in order to stop the ions within the same range (to keep the same resonator length) it is necessary to increase the pressure inside the gas cell which will cause a negative impact to upper state population of excimer molecules as it will be shown later in this chapter.

The beam straggling due to ion-atom collisions is around one order of magnitude higher than beam self dispersion due to finite transversal emittances. So this will be a determining factor in the selection of laser cavity length.

Let us see how the ion beam envelope will look if one takes into account the ion scattering and how the situation could be improved by varying a beam

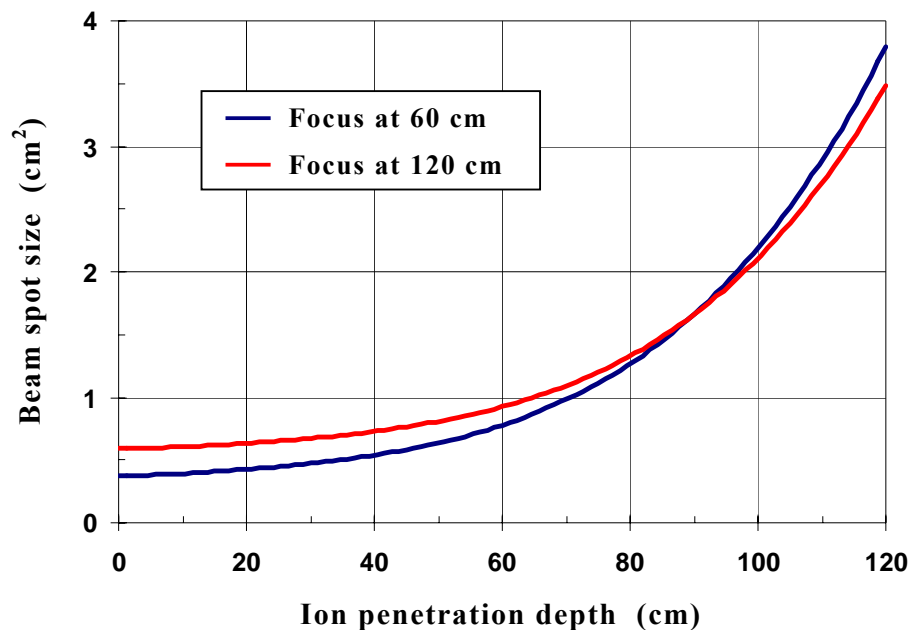


*Figure 3.5: Ion beam spot size as a function of depth inside the laser cavity for two focusing options:
 blue – focus in the middle of the laser cavity
 red – focus near the end of the cavity.*

focus position inside the resonator. In Fig.3.5 the ion beam spot size depending on the penetration depth of ions into the laser gas is shown ($x = 0$ – resonator entry, $x = 120$ cm – complete stopping of ions). The beam spot size (S_{beam}) was calculated on the basis of the elliptical beam shape taking into account dimensions of the ion beam in both horizontal (a) and vertical (b) planes:

$$S_{beam} = \pi \cdot a \cdot b \quad (3.5)$$

The calculation has been performed for Uranium ions with 300 MeV/u initial energy and with beam widths of 4 mm and 1,4 mm respectively in the focus in horizontal and vertical planes correspondingly (Fig.3.3) for two different positions of the beam focus. In one case the ion beam focus is placed in the middle of the resonator and in another case the beam focus is at the Bragg-peak region of ions (near the cavity exit).

By shifting the beam focus from the middle to the end of the laser cavity, one could improve parallelism of the ion beam, but it will increase an average spot size of the beam and consequently reduce the deposited power density on the axis. Therefore it is unreasonable to shift the focus beyond ion beam stopping range.

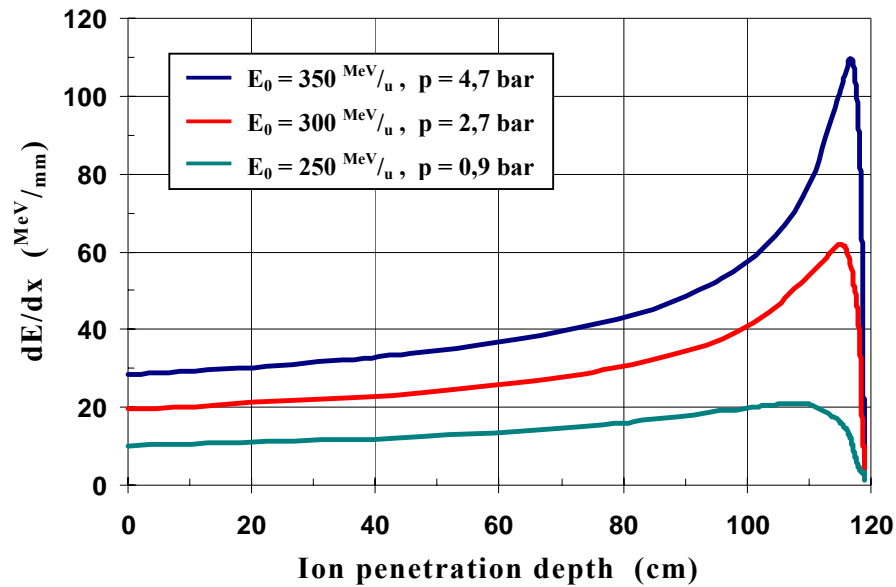


Figure 3.6: Energy loss of U-ions in the laser gas for different initial particle energies and target densities, calculated with the SRIM code.

The distribution of energy deposited in the gas mixture strongly depends not only on the ion beam shape inside the cavity but also on the stopping power of the gas mixture. The specific energy loss of an ion in turn depends on the ion's energy and target density (Chapter 2). Energy loss of Uranium ions in the laser gas (50% Ar and 50% excimer mixture) as a function of traversed range is shown in Fig.3.6 for three different cases (as for Fig.3.4) corresponding to initial particle energies: **250**, **300** and **350** MeV/u and the following gas pressures: **0,9 bar**, **2,65 bar** and **4,7 bar**. Thus the target densities were: **2,48** mg/cm³, **7,31** mg/cm³ and **12,97** mg/cm³ correspondingly.

As obvious from Figure 3.6, the Bragg-peak is more pronounced for the case with highest ion energy and highest pressure. So increasing the initial particle energy and target density is one of the ways to compensate large beam spread in order to obtain a more homogenous power deposition in the laser gas.

It is necessary to have the distribution of the pumping power density along the beam axis as homogeneous as possible in order to avoid possible defocusing of the laser light due to changing of the refraction coefficient along the axis. Figure 3.7 shows the power density deposited by a uranium beam in the laser gas versus the traversed range. It was calculated using Equation 3.1. The following ion beam parameters were used for calculations:

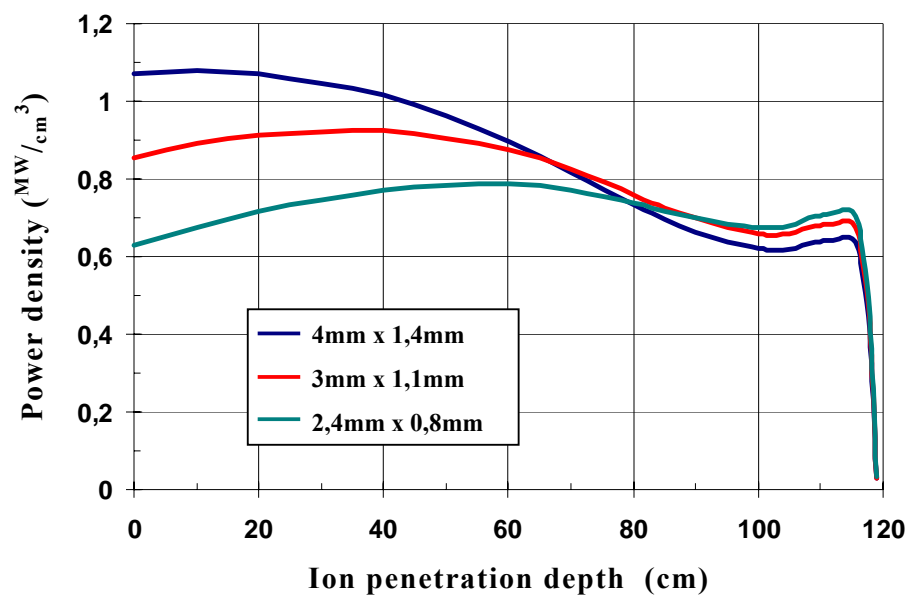


Figure 3.7: Distribution of the power density deposited by uranium ion beam along the laser cavity for different focal spots.

initial ion energy – $300 \text{ MeV}/u$, total number of particles in the beam – $2 \cdot 10^9$ and beam pulse duration – 100 ns , which is quite typical for compressed uranium beams on SIS-18 (see Chapter 4). Three cases of the ion beam focusing with different sizes of the beam in a waist (like in Fig.3.3) were considered. The position of the beam focus was placed at the end of the ion range (120 cm from cavity entry) for all three cases. Target parameters were the same as for $300 \text{ MeV}/u$ in figures 3.4 and 3.6.

A possibility to vary the size of the ion beam spot in the focus and consequently the shape of the beam envelope gives one more way to achieve uniform energy deposition in the laser gas. As one can see from Fig.3.7 the most homogeneous distribution for deposited power density is reached for ion beam widths in the waist of $2,4 \text{ mm}$ and $0,8 \text{ mm}$ in horizontal and in vertical planes correspondingly. The average power density on the beam axis in this case is $0,67 \text{ MW}$ per cm^3 which gives a specific deposited energy of $9,2 \text{ J/g}$ according to the pressure 2,65 bar and gas consistent mainly of 50% Ar and 50% Kr.

3.5 Energy deposition in the entrance mirror

The optical axis of the laser cavity should be coaxial to the ion beam axis in order to maximize the optical gain along the laser axis. In this case an entrance mirror of the laser cavity will be traversed by intense beams of heavy ions. Thus it is indispensable to estimate the energy deposited by the beam into the mirror and temperature increasing per single shot for certain ion beam parameters (beam spot size, intensity, ions sort, etc.). From these data one can conclude a limitation for a minimum ion beam spot size on the mirror.

For the first experiment it was decided to use a Al-MgF₂ coated quartz substrate as the entrance mirror. A SiO₂ or quartz has been chosen as a substrate material for certain reasons. It has a good chemical resistance, good thermal shock resistance and a low thermal expansion coefficient. Moreover, it has quite low density for solid material which is very important for ion beam propagation: the lower the density the smaller the energy losses of the ion beam in the mirror and the less beam straggling after the mirror. The most important material and physical properties of SiO₂ [Good, Jam92] is listed in a table below.

Table 3.5: Physical properties of SiO₂.

Density, ρ	2,32 g/cm ³
Melting point, T_{mel}	1715 °C
Specific heat, c	670-740 J/kg·K (at 25°C)
Thermal conductivity, λ	1,46 W/m·K (at 20°C)
Coefficient of thermal expansion, α	5,4·10 ⁻⁷ 1/K (20-1000°C)
Resistance to Fluorine	Good

In order to estimate “the worst” case for the mirror the “most extreme” parameters of the Uranium beam (which was planned for the experiment) have been taken into account:

$$\text{ion energy: } E_0 = 250 \text{ MeV/u (min planned)}$$

$$\text{beam intensity: } I = 4 \cdot 10^9 \text{ particles per pulse (max achieved)}$$

$$\text{beam spot size: } S = 0,2 \text{ cm}^2 \text{ (min planned)}$$

Maximum energy deposited into the mirror in this case will be **170 J/g** (concerning Equ.3.3), which gives an increasing of temperature of the mirror on **254 K** per a single shot (Equ.3.4).

In a thin Al reflective layer of the mirror, an ion beam with the just listed parameters will deposit approximately **160 J/g**, which will cause the increasing of temperature on **180 K**. Thus the layer temperature will be determined by the substrate temperature.

It seems quite harmless for the mirror substrate as far as the melting point of quartz is 1715 °C and its mechanical properties do not change to much at that temperatures (less than 300 °C). But for the Aluminum reflective layer it could be dangerous due to the low temperature of its melting point (660 °C). With heating up to 300 °C Al mechanical properties strongly decrease and this could cause intense evaporating of the Al coating from the mirror surface [Der05]. This estimation has been done for the most extreme case. The real (expected in the experiment) parameters of the Uranium are weaker (less intensity, bigger spot size) and therefore the real temperature of the mirror after a shot should be less than just estimated.

3.6 Calculation of the laser spot sizes

The spot sizes of the laser beam are determined by the type and characteristics of the optical resonator. Every two-mirror optical resonator can

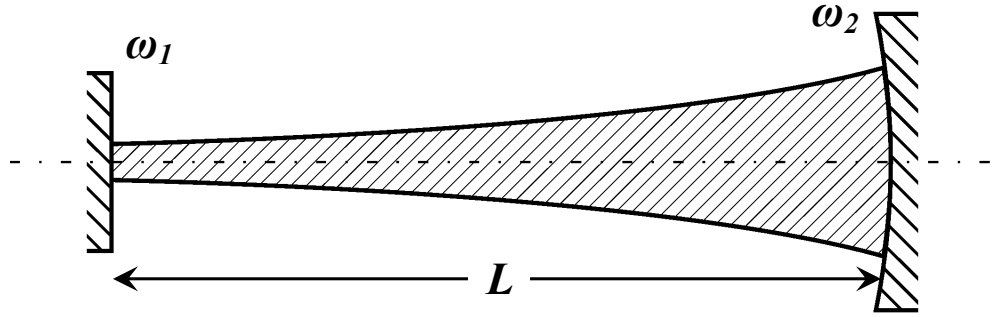


Figure 3.8: Laser beam in a half-symmetric resonator

be characterized by a pair of “resonator g parameters” which are determined by the mirror curvatures (R_1 and R_2) and the resonator length (L) [Sie86]:

$$g_1 \equiv 1 - \frac{L}{R_1} \quad \text{and} \quad g_2 \equiv 1 - \frac{L}{R_2}.$$

In our case we will deal with half-symmetric stable resonator⁶, which is formed by a planar ($R_1 = \infty$) and a curved ($R_2 = 3$ m) mirrors placed in a distance of 1,3 m from each other (a detailed description of the mirrors used in the experiment is given in Chapter 4). Thus the parameters of the resonator are following: $g_1 = 1$ and $g_2 = 0,567$.

The beam waist in the case of half-symmetric resonator will be located on the flat mirror as it is shown on Figure 3.8. The sizes of the beam spot ω_1 and ω_2 on both mirrors could be calculated using the following formulas [Sie86]:

$$\omega_1^2 = \frac{L \cdot \lambda}{\pi} \cdot \sqrt{\frac{g_2}{g_1(1 - g_1 g_2)}} \quad \text{and} \quad \omega_2^2 = \frac{L \cdot \lambda}{\pi} \cdot \sqrt{\frac{g_1}{g_2(1 - g_1 g_2)}}.$$

Therefore, the expected laser spot sizes will be **0,34 mm** and **0,46 mm** in the waist and on the curved mirror respectively.

3.7 Optical gain calculations

To determine the optical gain, which could be achieved in the cavity, it is necessary to know the upper state population N_u or the number of KrF* molecules permanently available in the pumping area during the ion beam

⁶ Such a resonator is equivalent to a half of a symmetric system (with two identical curved mirrors) that is twice as long [Sie86].

propagation. Let us consider the main processes for formation and dissociation of KrF^* molecules in the dynamic balance equation for N_u :

$$\frac{\partial N_u}{\partial t} = R_{lu} - A_{ul} \cdot N_u - B_{ul} \cdot N_u - C_{ul} \cdot N_u \quad (3.6)$$

where: R_{lu} – pumping rate per unit volume [$1/s \cdot \text{cm}^3$]
 A_{ul} – spontaneous emission rate [$1/s$]
 B_{ul} – stimulated emission rate [$1/s$]
 C_{ul} – collision decay rate [$1/s$]

The evolution of the upper state population N_u with time is mainly defined by the following processes: formation of excimer KrF^* molecules due to pumping the gas mixture by heavy ions with constant rate R_{lu} ; dissociation of the molecules due to relaxation process accompanied by spontaneous emission at $\lambda = 248$ nm with the rate A_{ul} ; dissociation of excimer molecules due to stimulated emission with the rate B_{ul} ; and finally, dissociation of KrF^* or formation another molecules due to kinetic collisions with other components of the gas mixture with so-called collision decay rate C_{ul} . The situation was considered only for a case of dynamical balance when: $\frac{\partial N_u}{\partial t} = 0$.

This balance can be achieved during the ion beam propagation when the pumping rate is maximum and constant⁷. Thus in the balance conditions N_u will be defined by following formula:

$$N_u = \frac{R_{lu}}{A_{ul} + B_{ul} + C_{ul}} \quad (3.7)$$

The pumping rate per unit volume R_{lu} can be calculated using Equation 3.8. The average along the beam axis power density P_{ave} of $0,67 \text{ MW}/\text{cm}^3$ deposited to the laser gas by the ion beam has been taken into account. This value corresponds to the assumed case of a homogeneous energy distribution along the laser axis which is described above in Paragraph 3.4 and shown in Fig.3.7. The energy of a single photon E_{1ph} with laser wavelength (248 nm) is 5 eV or $8 \cdot 10^{-19} \text{ J}$.

To predict what part of the ion energy deposited in the gas goes to pump a specific laser level in KrF^* is not a trivial task due to a complex reaction

⁷ This assumption can be done since the pumping pulse duration is in the order of magnitude longer than the time constants of various dissociative processes.

kinetics (see Chapter 2). Existing commercial KrF* excimer laser have a total conversion efficiency (laser output power divided by supplied power) of more than 2%. Therefore it was decided to take into account 1% of the energy deposited in the laser gas stored in KrF* molecules:

$$R_{lu} = \frac{P_{ave}}{E_{1ph}} \cdot 0,01 = 8,38 \cdot 10^{21} \text{ } \frac{1}{s \cdot cm^3} \quad (3.8)$$

The spontaneous emission rate A_{ul} is basically determined by a lifetime τ of the excimer level (theoretical value $\tau = 6,8 \text{ ns}$ [Ede78]):

$$A_{ul} = \frac{1}{\tau} = 1,47 \cdot 10^8 \text{ } \frac{1}{s} \quad (3.9)$$

The stimulated emission rate B_{ul} is proportional to the stimulated transition cross section σ_{st} and to the optical signal intensity I passing through the laser medium:

$$B_{ul} = \sigma_{st} \cdot I \quad (3.10)$$

But for the estimation a small signal gain coefficient g , signal intensity I supposed to be very small and consequently B_{ul} is negligible ($B_{ul} = 0$).

The last part in differential equation (Equ.3.6), the collision decay rate C_{ul} , describes one of the most important processes in excimer lasers – quenching of excimer molecules by atoms and molecules of mixture components. These processes could pass through different channels and finally lead to dissociation of the excited state of the molecule. Quenching rate constants k of KrF* by certain atoms and molecules, part of the laser gas mixture, are listed in a table below [Rok77, Ede78, Qui78a, Che79].

Table 3.7: Quenching rate constants of KrF molecule for different colliding particles (at $T = 300 \text{ K}$).*

Excimer molecule	Colliding particle	Quenching rate constant k , ($\cdot 10^{-12} \text{ cm}^3/\text{s}$)
KrF*	Ar	5
	Kr	3,6
	F ₂	650
	KrF*	370

A contribution of different gas components to the collisional decay rate is determined not only by the quenching rate constant but also by the concentration N of these components in the mixture:

$$C_{ul} = k_{Ar} \cdot N_{Ar} + k_{Kr} \cdot N_{Kr} + k_{F_2} \cdot N_{F_2} + k_{KrF^*} \cdot N_{KrF^*} \quad (3.11)$$

In the case considered here (Paragraph 3.4, Fig.3.7), the laser gas has the following parameters: pressure – 2,65 bar and the composition – 50% Ar, 49,75% Kr and 0,25% F_2 . This in terms of concentration means:

$$\begin{aligned} N_{total} &= 7,12 \cdot 10^{19} \text{ at./cm}^3 & N_{Ar} &= 3,56 \cdot 10^{19} \text{ at./cm}^3 \\ N_{Kr} &= 3,54 \cdot 10^{19} \text{ at./cm}^3 & N_{F_2} &= 0,02 \cdot 10^{19} \text{ mol./cm}^3 \end{aligned}$$

As far as the concentration of KrF^* molecules is supposed to be much (several orders of magnitude) less than others, the contribution of the last part in Equation 3.11 will be negligibly small. Thus, the collisional decay rate will be:

$$C_{ul} = 4,35 \cdot 10^8 \text{ 1/s}$$

As one can see, at these target parameters the quenching processes will be dominant since the collision decay rate is almost 3 times higher than the spontaneous emission rate.

The upper state population in the considered case will be:

$$N_u = 1,44 \cdot 10^{13} \text{ 1/cm}^3$$

From the value for upper state population one can obtain a small signal gain coefficient g_{ss} :

$$g_{ss} = N_u \cdot \sigma_{st} = 2,88 \cdot 10^{-3} \text{ cm}^{-1} \quad (3.12)$$

Thus, considering the length of the pumping region l along the beam axis of 118 cm (see Fig.3.7), an optical gain coefficient for a single trip of laser light inside the cavity could be obtained: $g_{single} = l \cdot g_{ss} = 0,34$.

If we assume the losses α on cavity mirrors around 10% for a round trip (see Chapter 4), the net gain for a round trip will be:

$$g_{net} = 2 \cdot g_{single} - \alpha = 0,58$$

For 100 ns pumping pulse we can assume approximately 12 round trips. Thus, the signal amplification of: $e^{0,58 \cdot 12} = 1,1 \cdot 10^3$ can be expected. So this is clearly the laser action.

3.8 Conclusions

Summarizing this chapter, it can be concluded that the design of the experiment with heavy ion beams is not a trivial task. A lot of parameters, connected with each other, have to be taken into consideration carefully, because varying one parameter will affect the others. So, optimization of one parameter can lead to degradation of the others, and therefore it is important to vary the parameters in a way to get the optimal net effect. For example, in order to make the gas volume, pumped with the ion beam, smaller and more cylindrical (reduce the effect from ions scattering in the intermediate materials keeping the same ion range), in order to increase the pumping power density, it needs to increase the initial ions energy. But this will require an increasing laser gas pressure inside the cavity, in order to fit the ions into the same resonator length. Increasing the gas pressure will increase collision frequency of the gas atoms and therefore collision quenching rate of the excited excimer molecules. In principle, this should be compensated by increasing the pumping power density with pressure. However, the net effect on the upper state population could be negative due to complex kinetics of KrF^* (at high pressures the three-body processes, which efficiently quench excited KrF^* states are activated). Moreover, the increase of initial ion energy will make the difference in energy deposition near entrance of the cavity and in the Bragg-region more pronounced (Fig.3.6) and thereby the heating of the laser gas less homogeneous, which can cause undesirable diffraction effects.

Chapter 4

Experimental Setup and Diagnostics

This chapter is dedicated to the detailed description of the experimental setup. The main elements and systems of the laser cavity are discussed. Attention is paid to different diagnostic techniques and instruments used in the experiment. Main advantages and disadvantages of some existing diagnosing methods are discussed as well. A short overview of the experimental area and on the accelerator facility at GSI (Gesellschaft für Schwerionenforschung) for experiments with heavy ion beams is also given.

4.1 GSI accelerator facility

The accelerator facilities at GSI provide many possibilities for experiments on high-energy-density in matter induced by heavy-ion beams. Intense beams of high energy heavy ions, that are delivered by the heavy ion synchrotron (SIS-18), are used at the HHT ("High energy High Temperature") experimental area to heat large volumes of matter at solid density to extreme conditions of temperature and pressure. The accelerator related aspects of the GSI facilities important for the experiments at the HHT area are described below.

The beams of heavy ions are first produced and pre-accelerated at the ion source area (see Fig.4.1). Two different high-current ion sources can be used simultaneously. There are several different ion source types, e. g. PIG (PennInG ion source), MEVVA (MEtal Vapour Vacuum Arc), MUCIS (MUlti Cusp Ion Source) and others [Kel88, Spä98]. For the Laser experiments a source which provides the heaviest ions and the maximum current of a given

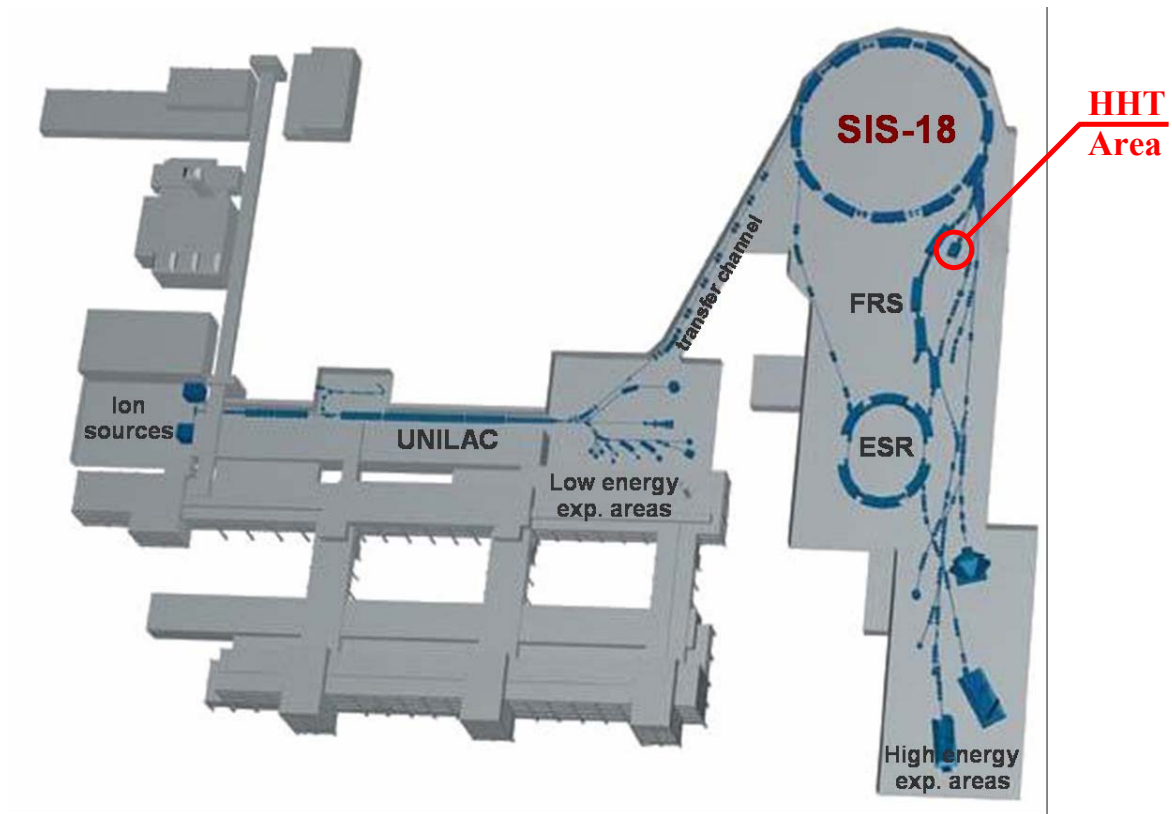


Figure 4.1: GSI accelerator facility

ion species is preferable (see Chapter 3). The particles produced by the ion source (in the laser experiment PIG ion source was used) are then accelerated in the linear accelerator UNILAC (UNIversal Linear Accelerator). The UNILAC has two acceleration stages with different RFQ-accelerating structures. It can deliver intense beams of heavy ions on the energy range from $1,4 \text{ MeV}/u$ to $20 \text{ MeV}/u$. After acceleration in the UNILAC, these beams can either be extracted for experiments at the "low energy" experimental hall or can be guided into the transfer channel to SIS-18 for further acceleration (Fig.4.1). A stripper is installed inside the transfer channel which allows increasing the charge state of ions before injection into the synchrotron.

After acceleration in the UNILAC linear accelerator, the heavy ion beam is injected into the synchrotron SIS-18. The injection energy is about $11,4 \text{ MeV}/u$. In the heavy ion synchrotron SIS-18 which has a circumference of 216 m, a maximum bending power of 18 Tm and RF acceleration with $0,8 \div 5,6 \text{ MHz}$ at 16 kV, intense beams of heavy ions can be accelerated up to $2 \text{ GeV}/u$ energy ($1 \text{ GeV}/u$ for uranium ions) [Var02]. To accumulate the beam intensity in the ring, a multi-turn injection scheme is used, where the ions are

injected over several revolution periods and fill the entire transverse phase space acceptance of the ring.

Since 1998 an electron cooler became available at SIS-18. Using the electron cooler it is now possible to increase the intensity of the ion beam in the ring several times. For this purpose a multi-multi-turn injection scheme is employed [Spi06]. The transverse emittance of the ion beam is reduced due to interaction with a coaxial low-emittance electron beam in the electron cooler. This takes place between successive multi-turn injections from the UNILAC. Electron cooling increases the phase space density of the beam and therefore the number of particles that can be accumulated at a given acceptance of the synchrotron. For instance, in the year 2003 with 25 injections using the multi-multi-turn scheme, $4,5 \cdot 10^9$ of $^{238}\text{U}^{73+}$ ions were accumulated in the SIS-18 which were accelerated and delivered to the HHT area for experiments [Var03]. Currently the SIS-18 synchrotron is able to deliver beams of more than $2 \cdot 10^{10}$ ions of ^{86}Kr , $7 \cdot 10^{10}$ ions of ^{40}Ar and more than 10^{11} ions of lighter species [Var02, Spi05]. But with further commissioning of the SIS-100 ring the intensity of the ion beams will be significantly increased in the near future [Hof05].



Figure 4.2: Beam transport line at the HHT experimental area

After the acceleration in the SIS-18 synchrotron, the beam is extracted and guided to the high energy experimental areas (Fig.4.1). For the experiments at the HHT the fast extraction mode is required. In this mode the beam is bent from its synchrotron orbit by a fast magnetic kicker ($\tau < 90$ ns) to an extraction channel in the septum magnet. All particles are extracted within one revolution period [Ree06].

High energy, high intensity heavy ion beams extracted from the synchrotron are transported to the HHT experimental area in a special beamline (Fig.4.2). The total length of this beamline from SIS-18 to the target chamber is about 75 m and the maximum bending power of its magnets is 10 Tm [Var02]. The last 30 m long part of the beamline is used only for the HHT experimental area and consists of three bending dipole magnets, two quadruple doublets and one quadruple triplet. Various beam diagnostic instruments and vacuum control devices (not shown in Fig.4.2) are also built into the beamline.

Typically, in the experiments at HHT, the heavy ion beams with energies of $200\div 400$ MeV/u are used and bunch compression down to 100 ns (FWHM). Using the final focusing system of HHT beamline it is possible to obtain a beam spot around 0,6 mm (FWHM) [Var03].

4.2 Setup of the optical cavity

The laser setup consists of a stainless steel tube, vacuum system, high pressure gas filing system, mirror adjustment units and a number of different instruments for controlling and diagnosing the experiment.

The cavity setup was placed at a distance of **2 m** (Fig.4.3) from a last quadruple magnet of the HHT-beamline due to the following reasons. Firstly, to make the ion beam more or less parallel along the cavity and at the same time reduce the beam spot up to the certain level, it was necessary to shift the beam focus position a few meters out of the last magnet. Secondly, it was necessary to have some air gap between the gas cell and a beamline vacuum system for safety reasons. If the cavity cell were directly connected to the beamline, or the gap were too small (couple of centimeters), then in the case of some accident with an entrance ion beam window, high pressure from the gas cell could blow off the exit Al-window (150 μm thickness) of the beamline and a shockwave produced by a pressure difference could destroy diagnostic elements in the beamline.

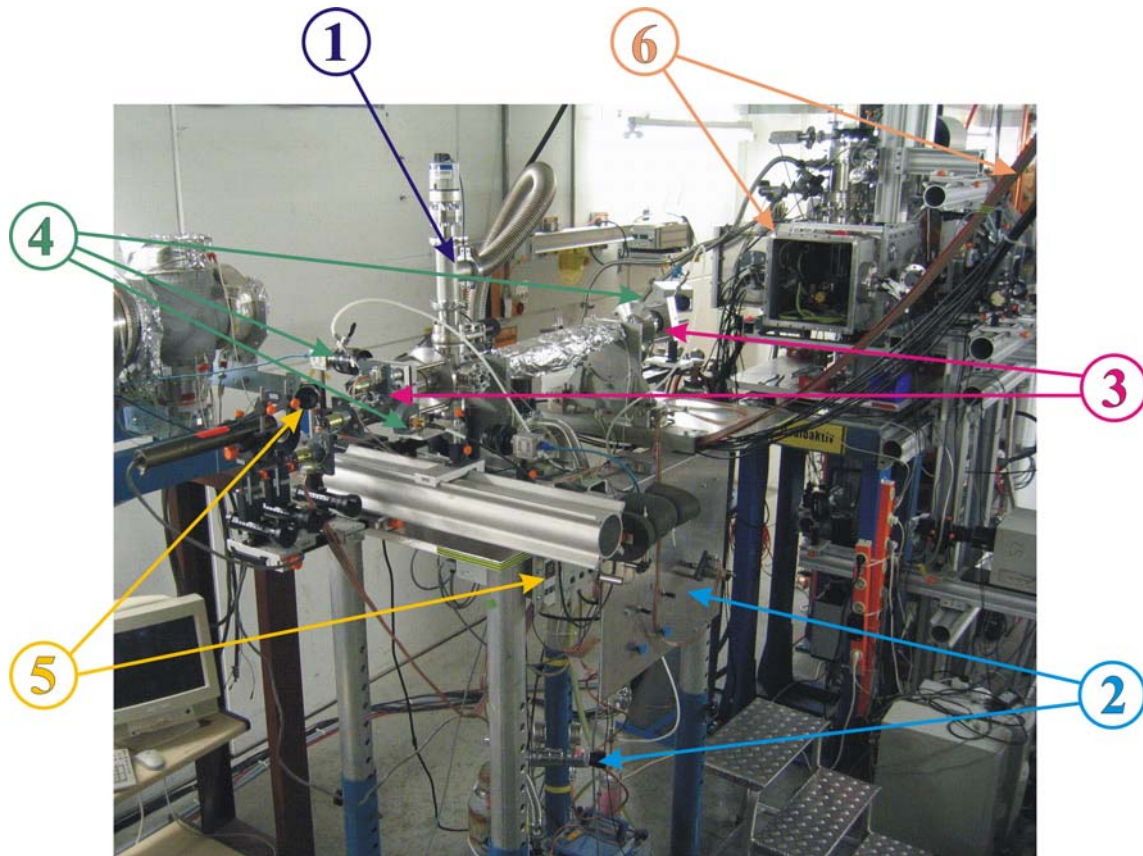


Figure 4.3: Heavy-ion-beam laser setup:

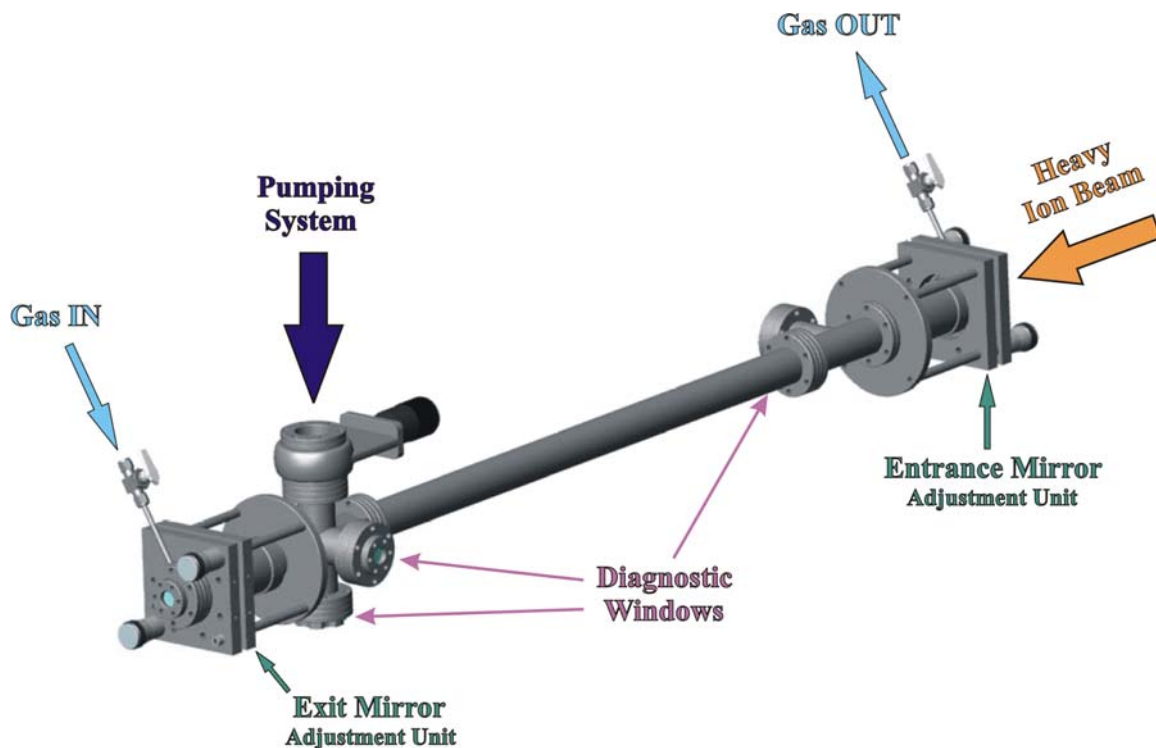
- 1 – evacuating system;*
- 2 – high pressure gas and filtering system;*
- 3 – optical resonator; 4 – diagnostics;*
- 5 – monitoring system; 6 – HHT beamline and target chamber.*

4.2.1 Vacuum System

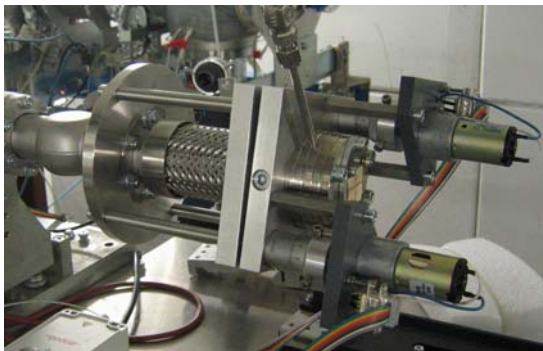
As a vacuum system a combination of an oil-free diaphragm prepump and a turbomolecular pump has been used. Due to the fluorine contained in the laser gas mixture, water had to be removed from the walls of the gas cell. For this purpose the walls were heated up to **130°C** with a special “heating wire” wound around the laser cell. The vacuum inside the gas cell was measured with a full range gauge PKR-251 (Pfeifer Vacuum) and during the preparation a pressure down to **$1 \cdot 10^{-6}$ mbar** was reached. During the experiment, when the gas cell was filled with more than **2 bar** of the excimer mixture, the vacuum system was shut by a CF-40 gate valve.

4.2.2 High Pressure Gas System

The gas system was connected to the cell at two points (IN and OUT) using special flanges and 6 mm diameter teflon tubes which are fluorine resistant and strong enough to allow pressures up to 10 bar to be used. The gas system was operated in a flow mode. The geometry of the connection points was chosen in a way to maximize the volume inside the laser cell which was included in the gas flow. To make sure to have a constant concentration of fluorine in the gas mixture and to prevent depletion of fluorine by impurities, a steady flow was established in the gas cell.



a)



b)

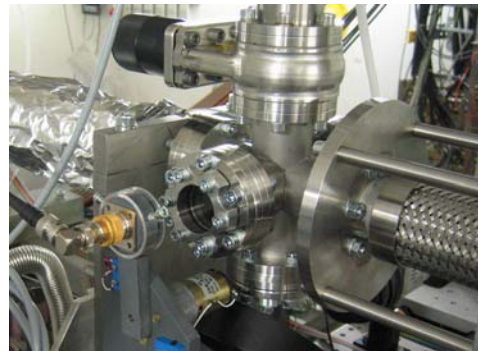


Figure 4.4: Scheme of the heavy-ion-beam laser setup.
 a – remotely controlled adjustment unit for the entrance mirror
 b – double-cross unit with diagnostics near the end of the cavity

Gas bottles containing an Excimer laser gas mixture (95,5% Kr + 0,5% F₂ premix) and pure Ar (Ar 4.8) as a buffer gas, respectively were connected to the system to be able to prepare various mixing ratios. To prevent a gas leakage in the case of some accident (depressurizing of the cavity, for example) two remotely operated electro-mechanical valve actuators (HOKE 0112L2) with ball valves (HOKE 7142G6Y) and a remote control unit were installed on the inlet and outlet of the cavity. Metering needle valves (HOKE 1335G6Y) were installed on each gas-bottle in order to control the flow rate. The possibility of remotely controlling the outlet orifice was realized by installing a metering valve with electrical motor. This allowed varying the pressure inside the cavity remotely. High pressure values in the gas cell were measured with a piezo gauge APR-267 (Pfeifer Vacuum) which can measure up to 55 bar with an accuracy of 2%. In the output of the system the gas flow passed through special fluorine filter which absorbs F₂ and prevents it get into the atmosphere.

4.2.3 Opto-Mechanical System of the Laser Cavity

The optical resonator was formed by two mirrors. The first was an Al-coated flat mirror on a fused silica substrate (d = 25 mm; thick.= 3,2 mm) placed near the ion beam entrance to the gas cell. A second – dielectrically coated highly reflective mirror for the wavelength of 248 nm based on plane-concave fused silica substrate (d = 25 mm; thick.= 6,35 mm) with 3 m radius of curvature was placed at a distance of 1,3 m from the first one. This exit mirror was also used as a pressure window for the cell and for decoupling the laser light from the resonator. For precise alignment of the optical cavity specially designed adjustment units were attached to each mirror (Fig.4.4a). These units allowed turning each mirror around two perpendicular axes in a mirror plane with high accuracy. The accuracy of alignment was attained by using leveling screws with micron steps (BS 30.10, Newport). A basis of the adjustment unit was a flexible bellow braided with stainless steel (Pfeifer vacuum) which can withstand pressures up to 10 bar. Each leveling screw had been equipped with remotely controlled electrical motor in order to provide mirror alignment on-line.

4.2.4 Pressure and Diagnostic Windows

For proving laser action as well as for obtaining spectra and recording light profiles of the ion beam is it necessary to have several diagnostic windows at different places of the gas cell. Here we had very specific

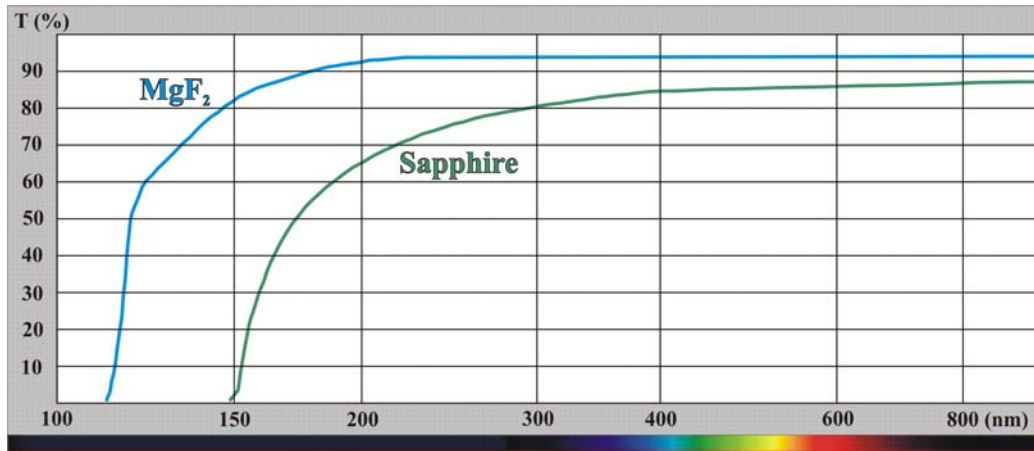


Figure 4.5: Transmission curves for Sapphire and MgF₂ in UV-VIS range

requirements for the windows. First of all, they have to withstand a high pressure in the gas cell up to 10-15 bar. Secondly, they should be stable to strong chemical reagents such as: halogens (F₂, Cl₂, etc.), halogen acids (HF, HCl, etc.) and halogen radicals (F⁺, Cl⁺, etc.). And finally, all diagnostic windows should have a good transparency for visible and UV light.

Two kinds of material were chosen due to requirements described above: MgF₂ (d = 38 mm, thick. = 6,5 mm) and Sapphire (d = 25 mm, thick. = 2,3 mm). MgF₂ has better transmission for UV-light but it is very fragile and demands better care during handling. Sapphire, on the other hand, is more elastic and stronger but its transmission for UV-light is lower (Fig.4.5).

As an ion beam entrance window to the gas cell a 50 μm thick stainless steel foil has been used (see Chapter 3).

4.3 Diagnostic tools

In this paragraph various diagnostic tools used in the experiment for observing and proving of the laser action in the cavity are described.

4.3.1 Ion beam diagnostics

For obtaining the laser effect in the cavity cell as well as for precise calculations of the deposited energy, pumping power density, laser efficiency, etc. it is very important to measure and control the following characteristics of the ion beam:

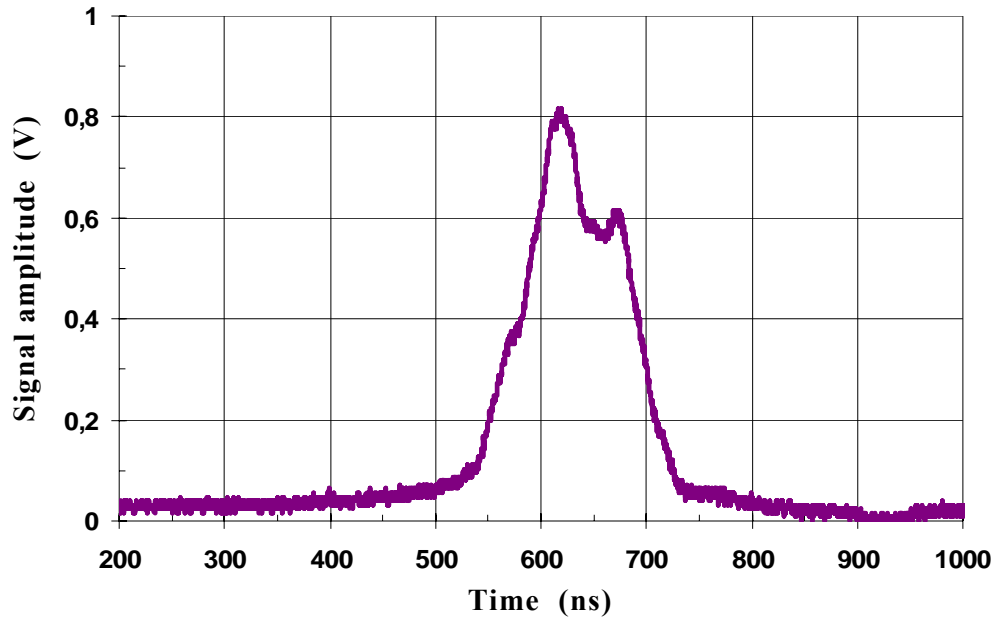


Figure 4.6: Time structure of the ion beam pulse recorded with FCT for experimental shot with beam intensity of $2,34 \cdot 10^9$ particles per bunch.

- *beam intensity* (the total number of particles in the beam pulse)
- *duration and temporal shape of the ion beam pulse*
- *spatial shape of the ion beam inside the cavity cell* (beam envelope along the laser axes and spot size)

The intensity of the ion beam and its temporal profile were measured by a number of different beam current transformers installed in the HHT beamline. These are the Fast Current Transformer (FCT), the Integrating Current Transformer (ICT) and the Resonant Current Transformer (RCT). The FCT transformer [Ber91a] is used for precision measurements of the time shape of the beam pulse. It allows measuring the temporal beam profile with better than 5 ns resolution. The ICT transformer [Ber91b] has a slower response (30 ns time resolution) and is more convenient for the beam intensity measurements. The RCT current transformer [Sch96, Ree01] does not provide any time resolution but it was especially designed for precision measurements of the total number of particles over a very wide range from 10^5 to 10^{12} .

In this experiment the signal from the FCT (HHTDT7) placed behind the exit window of the HHT beamline was recorded by an oscilloscope for every shot. Logged data from the RTC in the extraction line (TE1DT1) provided information about the total number of particles in the beam pulse with

accuracy better than 2% [Ree01]. A typical signal from the FCT is shown in Fig.4.6. The zero point on a time scale corresponds to a timing signal from the main trigger provided by the accelerator.

Diagnosing the space distribution of the ion beam is more complicated, especially when dealing with very intense beams (more than $2 \cdot 10^9$ particles per bunch) of very heavy ions (like ^{238}U) focused in a narrow spot (around 0,5 mm of FWHM). Usual methods for diagnosing transversal intensity distribution of the beam such as “solid scintillators” or “electrical conductive wires” [For06a, For06b] are not suitable for this case. Because the energy density of such beams is so high that any scintillating materials could be not only saturated but also damaged by the ion beam. The same is the case with conductive wires, any solid material placed into the beam with characteristics

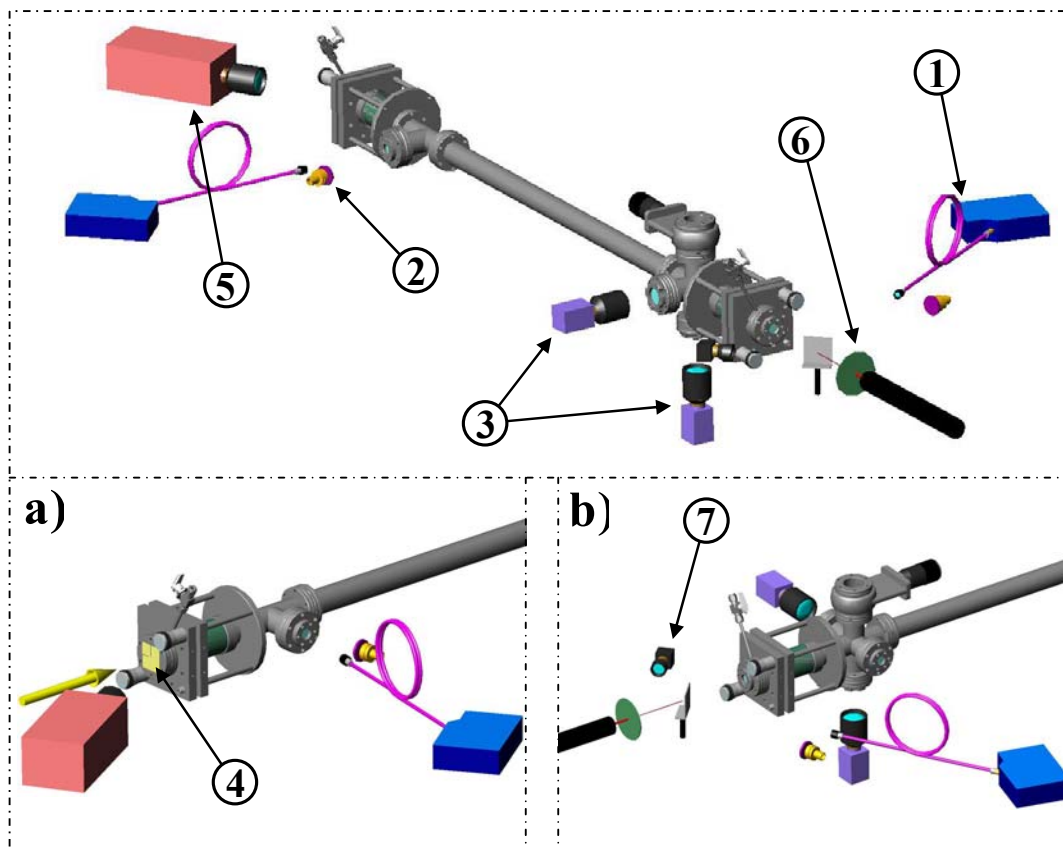


Figure 4.7: Experimental setup with diagnostics:

- 1 – compact USB-spectrometer with fiber optic input;*
- 2 – high speed UV-photodiode with interference filter for 248 nm;*
- 3 – gated CCD-cameras; 4 – entrance scintillator;*
- 5 – scintillator camera; 6 – adjustment He-Ne laser with diaphragm; 7 – video camera for mirror alignment.*

described above could be damaged or even destroyed. Therefore for diagnosing space characteristics of such kind of beams it requires to use non-destructive methods. As such a method gas scintillation has been used [Plu02, For04, Pet04, For05].

In order to estimate an ion beam envelope inside the cavity cell, the beam was observed at two points: near the entrance of the gas cell and near the end, in the Bragg-peak region of the ions. A thin (600 μm) Al_2O_3 -scintillator was installed just before an entrance window to the laser cavity for visual control of the beam position and spot size during positioning and focusing of the ion beam. A gated video camera observed the scintillator at an angle of approximately 40° to the beam axis (Fig.4.7a). The alignment of the ion beam was performed with reduced intensity down to 1 injection (around 10^8 particles per bunch) in order to save the entrance mirror and the scintillator from unnecessary damages.

The ion beam size and space distribution of the intensity in the Bragg-peak region were estimated using the gas scintillation. During the propagation of the ion beam through gas each ion produces excitation and ionization processes. Excited gas atoms and ions partly give off their excitation energy by emitting the light [Wie01]. The emitted light was registered by two high-resolution gated CCD-cameras (Pixel Fly, PCO) installed in perpendicular planes (Fig.4.7) in order to provide horizontal and vertical light profiles of the ion beam. An analysis of the recorded images via light profiles [Ado05] provides necessary information about intensity distribution of the ion beam, beam position, beam envelope in observed region, position of the Bragg-peak and therefore the range of ions which together with gas pressure and gas composition information provides a value for initial ion energy at the entrance of the laser cell (see Chapter 5).

Both cameras were installed near the cavity exit and observed a region from a distance of approximately **102 cm** to the entrance stainless steel window to the laser cell (Fig.4.7). A camera installed in the horizontal plane was looking for a vertical light profile of the ion beam. It observed an area of **32 mm** along the beam axis and **26 mm** perpendicular to the beam axis with mounted lens Soligor (f.50/app.1,3). The second one, in a vertical plane, has mounted lens Cosmocar (f.75/app.1,4) and it was viewing **34 x 27 mm** area. The resolution of both cameras was 1280 x 1024 pixels with a pixel size of 6,7 x 6,7 μm which results in 39,9 pixels per mm for the horizontal camera (the first one) and 37,6 pixels per mm for the vertical camera (the second one). The spatial resolution achieved with these cameras was **25 μm** and

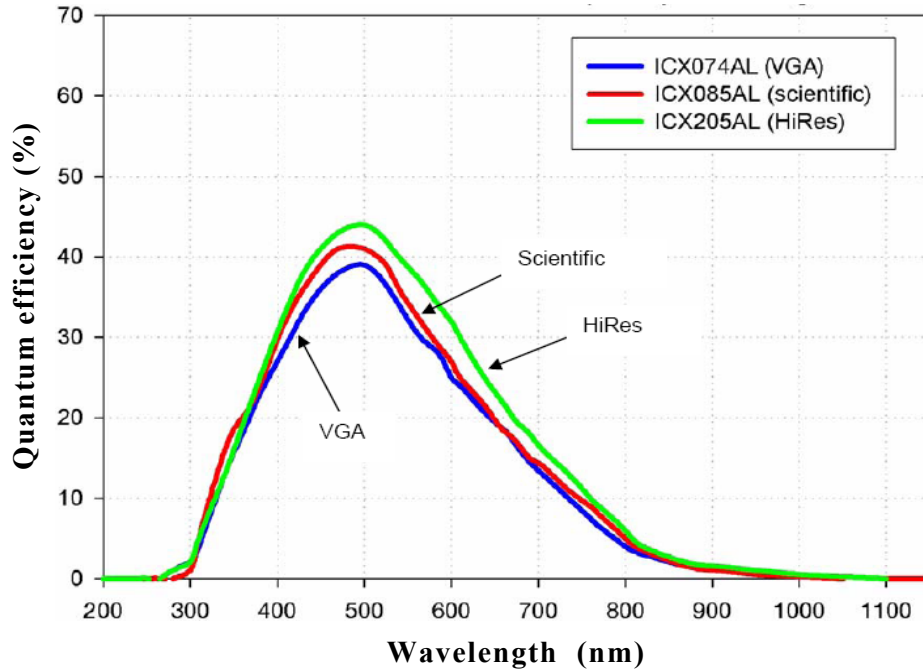


Figure 4.8: Spectral response of PixelFly CCD image sensors for different versions (red – version used in experiment)

27 μm horizontally and vertically respectively. The integration time of 10 μs was used for both cameras during experimental shots. So afterglow processes were registered equally with direct fluorescence.

A typical spectral response of PixelFly CCD-detectors is shown in Figure 4.8. As one can see, emission of KrF^* on the laser line (248 nm) could not be detected with PixelFly cameras.

PixelFly camera acquires **12 bit** images resolved with 4096 ($2 \cdot 10^{12}$) grey levels between black and white, however the data could only be saved on a hard disk in 8 bit or 16 bit format, respectively.

Note, that during the beam propagation in the gas target, a lot of high energetic secondary electrons are produced. They can fly out of the ion beam region and excite/ionize gas atoms outside the beam hit area. Thereby the light profile, recorded with a CCD camera is broadened by secondary electrons, which does not allow obtaining a real ion beam spot size. However, this broadening could be estimated and taken into account, since it is determined by the electron range in the gas and depends on gas pressure. More detailed discussion of this topic will be given in the next chapter.

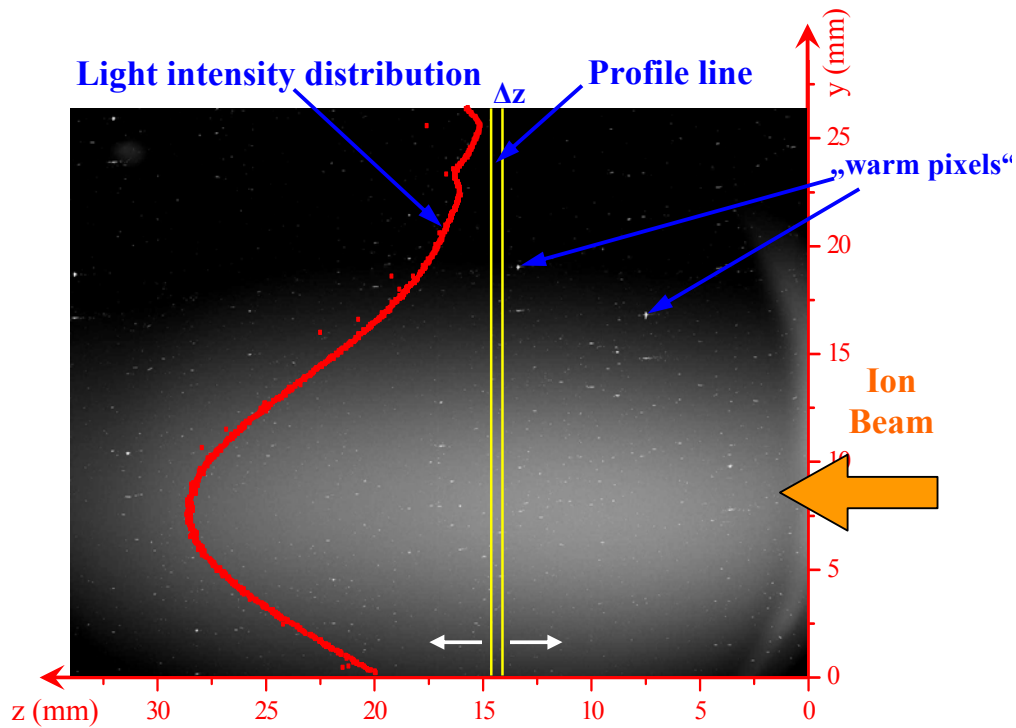


Figure 4.9: Measurement of a light intensity distribution by processing a gas scintillation image recorded with vertical PixelFly camera.

An example of a gas scintillation image recorded with the PixelFly camera is shown in Fig.4.9. The beam of heavy ions comes from the right hand side and is stopped in the field of view of the camera. The vertical profile line shows the light intensity distribution perpendicular to the ion beam axis (shown in Fig.4.9.) The width of the profile line Δz was optimized in order to reduce an influence of “warm pixels” (see next section). The horizontal profile line (not shown in the Figure) gives the distribution of the light intensity along the beam axis (z -axis on the Figure). Thus one could obtain the position of the Bragg-peak maximum. The ion beam shape in the field of camera view could be obtained by scanning of the image with the vertical profile line along the ion beam axis.

Concluding this section it can be noted that the gas scintillation method of ion beam profile diagnostics has the disadvantage that it is based on the observation of non-direct processes (processes, which could be stimulated not only by ions) and it does not provide real beam sizes. On the other hand, a great advantage of this method is that it is non-destructive and it gives a unique possibility for diagnosing highly intense ion beams, when other

methods are not applicable. Also, using the gas scintillation method we can make sure not to hit the end cavity mirror with the ion beam.

4.3.2 Spectral measurements

A compact USB-spectrometer (HR4000, Ocean Optics) has been used to observe the appearance of the laser light as well as to compare spectral characteristics of spontaneous and stimulated emission. The spectrometer consists of three main parts which determine its optical resolution: entrance slit, diffraction grating and linear CCD-array detector. The spectrometer used in the experiment described here had an optical resolution of **2,32 nm**. An electronic shutter of the spectrometer allows decreasing an integration time down to 10 μs [Ocea].

The spectrometer has a fiber optic input. To avoid the optical damping in the long fiber (several tens of meters) between the target area and an experimental room it was decided to apply a light collecting optics with a short (2 m) UV-fiber. This solution required an installation of spectrometer in the HHT-cave close to experimental setup. Due to hard radiation background at HHT during the ion beam shot a lot of “warm pixels” appear in the spectra (Fig.4.10). This could be explained by the following reason: neutron, x-ray or γ -ray fluxes from the ion beam produce charge particles inside single elements of CCD-array detector. This additional charge of the CCD-element is observed as a strong single-pixel (with FWHM ≈ 1 pixel) line in the spectrum. The

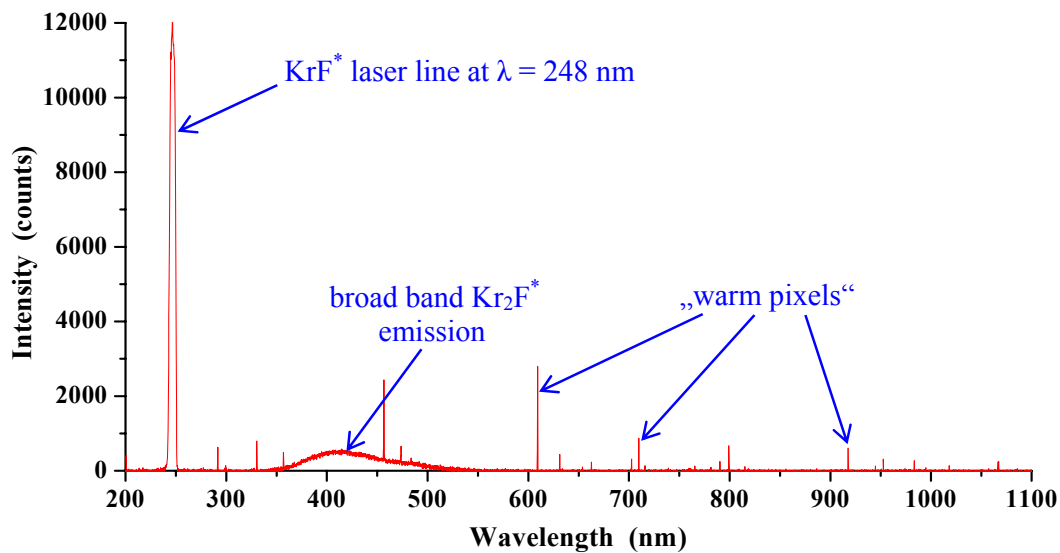


Figure 4.10: Example of a spectrum of a light emitted along the laser axis, recorded with compact USB-spectrometer HR4000

closer the spectrometer is placed to the ion beam axis, the higher the flux of ionizing particles and consequently the more “warm pixels” are present in the spectrum. The distinctions of these lines are that they have no real line shape (just single pixels) and they are not reproducible from shot to shot and this allows splitting them from true spectral lines.

An example of the fluorescence spectrum the laser gas acquired along the optical axis of the laser cavity is shown in Figure 4.10. A sharp band at $\lambda = 248$ nm corresponds to the KrF^* laser emission, and a broad band centered near 420 nm corresponds to the Kr_2F^* emission (see Chapter 2).

4.3.3 Laser and spontaneous emission measurements

To measure the intensity and time structure of the light emitted by KrF^* excimer molecules perpendicular to the laser axis (spontaneous emission) and along the laser axis (stimulated emission) as well as for obtaining quantitatively a dependence of this light intensity from pumping power density, two high speed photodiodes (AXUV20HS1BNC, IRD Inc.) have been used. These are silicon diodes with a sensitive area of 20 mm^2 .

The diode response time is determined by the resistance and capacitance of the detector and the measuring circuit and the charge carrier transit time. The capacitance C of the diode is given by the silicon permittivity ε , area A , and the p-epitaxial layer thickness D :

$$C = \frac{\varepsilon \cdot A}{D} \quad (4.1)$$

The AXUV20HS1BNC diode has a $25 \mu\text{m}$ thick silicon sensitive layer, the capacitance C is **700 pF**.

The diode resistance is determined by the distance electrons need to travel in the front field free n region towards the $n+$ electrode. The resistance of AXUV20HS1BNC is only 1 Ohm. Using the 50 Ohm scope impedance, 1 Ohm diode resistance and 700 pF capacitance, the rise time given by $2,2 \cdot RC$ is **1,7 ns** [AXUV].

Worst case carrier transit time is a hole traveling across the entire depletion layer thickness. The time is given by the thickness D divided by the hole drift velocity v which depends on the applied bias voltage. In order to avoid the influence of electromagnetic noises from the power network to the diode reading a special bias power supply has been constructed. It consists of the 12 batteries (9V, Krona) and provides **-117 V** bias voltage. The electric

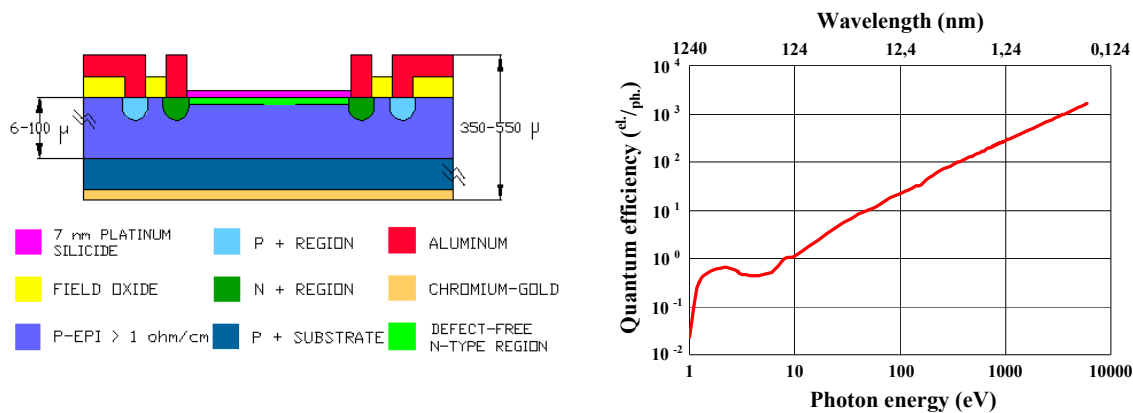


Figure 4.11: Structure scheme (left) and quantum efficiency curve (right) of Absolute XUV photodiodes.

field for the diodes is $4,7 \cdot 10^4$ V/cm in this case and the corresponding drift velocity is $1,2 \cdot 10^6$ cm/sec which gives a theoretical rise time of **2 ns**.

Diodes of the AXUV-series were specially designed for absolute measurements of photons with wavelength from NIR (1200 nm) and down to the X-rays range (0,2 nm) [Gul96, Can98]. When these diodes are exposed to photons of energy more than 1,12 eV (wavelength less than 1100 nm) electron-hole pairs (carriers) are created. These photo-generated carriers are separated by the p-n junction electric field and a current proportional to the number of electron-hole pairs created flows through an external circuit. For the majority of XUV photons, about 3,7 eV energy is required to generate one electron-hole pair. Thus more than one electron-hole pair is generally created by these photons. This results in device quantum efficiencies (electrons seen by an external circuit per incident photon) much greater than unity (Fig.4.11), which increase linearly with photon energy.

Two unique properties of the AXUV photodiodes provide previously unattainable stable, high quantum efficiencies for XUV photons [AXUV]. The first property is the absence of a surface dead region i.e. no recombination of photo-generated carriers in the doped n-region or at the silicon-silicon dioxide interface. As absorption depths for the majority of XUV photons are less than 1 μm in silicon, the absence of a dead region yields complete collection of the photo-generated carriers by an external circuit resulting in 100% carrier collection efficiency and near theoretical quantum efficiency.

The second unique property of the AXUV diodes is their extremely thin (3 to 7 nm), radiation-hard silicon dioxide junction passivating, protective entrance window. Owing to these two properties, the quantum efficiency of

AXUV diodes can be approximately predicted in most of the XUV region by the simple expression:

$$\varepsilon_{quant.} \left(\frac{\text{electrons}}{\text{photon}} \right) = \frac{E_{ph.}}{3,7eV} \quad (4.2)$$

where: E_{ph} – photon energy (eV).

To be sensitive only to the light which corresponds to the KrF* excimer transition (${}^2\Sigma \rightarrow {}^2\Sigma$) at a wavelength of 248 nm and to cut off any other light, for example, broad band Kr₂F* light emission in the region 350÷500 nm (Fig.4.10) or Ar-I and Kr-I lines in the region 600÷900 nm, bandpass interference filters (254FS40-25, Lot-oriel) had been mounted in front of each photodiode. The central wavelength of the transmission band is at **254 nm** (Hg-line) and the FWHM is **40 nm**. This type of filters has a second order transmission at $\lambda \approx 508$ nm but the transmission for this region is about two orders of magnitude lower than for the main band.

4.3.4 Remote adjustment of cavity mirrors

As was mentioned above the adjustment units for both cavity mirrors were remotely controlled with good precision. A pre-alignment of the cavity

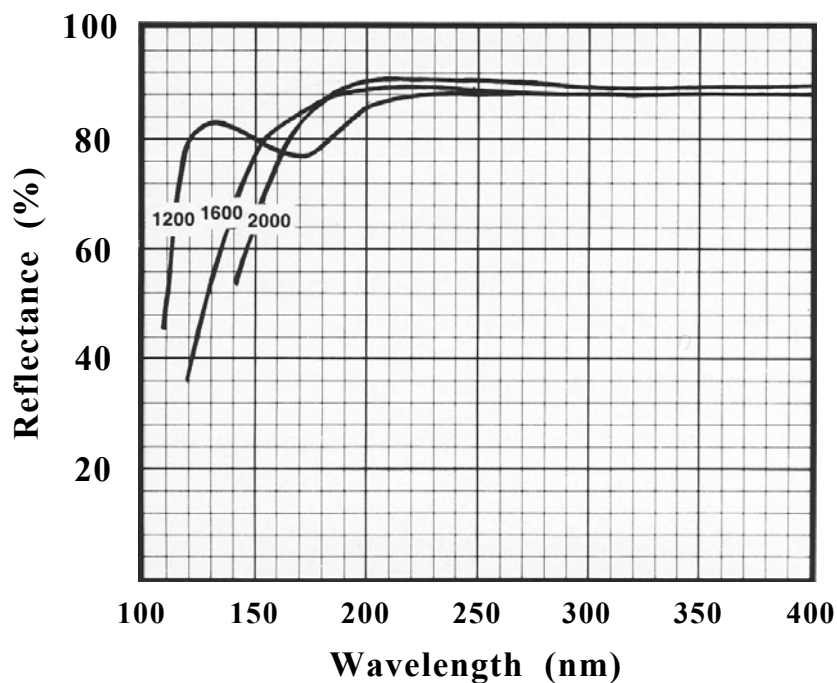


Figure 4.12: Reflectivity curves for Al-MgF₂ mirror for different types of coating optimized for maximum reflectivity at 120, 160 and 200 nm respectively [ARCo].

mirrors was performed manually just before the experiment using a He-Ne laser with a 1 mm diaphragm installed on the laser axis (Fig.4.7). Cavity alignment by the He-Ne laser beam was possible because the Al-coated entrance mirror was approximately 90% reflective both for UV and for visible light (Fig.4.12) and the highly reflective exit mirror for 248 nm based on fused silica substrate was transparent for visible light. Reflectivity curves for typical Al-coated mirrors protected with MgF₂ layer are shown in Figure 4.12. The reflectivity of the end mirror for 248 nm light was better than 99,5 % [CVIL].

But since the exit mirror was used also as an optical window, manipulations of the gas pressure inside the laser cell could disadjust the cavity. Therefore, it was necessary to make sure that the resonator mirrors were well realigned after changing the pressure. A video CCD-camera was used for this purpose as well as for performing on-line readjustment. It was installed near the exit mirror at an angle of approximately 35÷40° with respect to the laser axis and observed a back reflection of the adjustment laser (Fig.4.7).

Chapter 5

Experiment and Results

As mentioned in Chapter 1 the main aim for this work was to test heavy ion beams for pumping short (UV-VUV) wavelength lasers. For this demonstrational experiment the following goals were assigned: to obtain laser effect on the KrF^* excimer laser transition ($\lambda = 248 \text{ nm}$), to prove laser action by various methods and to study the basic laser parameters, such as: laser threshold for this specific setup, optical gain, and conversion efficiency of the ion beam power to the laser output power.

5.1 Ion beam and target parameters

The experiment was performed at the HHT target area at GSI on December 7 and 8, 2005 [Ulr06a, Ulr06b, Ado07a]. Pulses of Uranium ions provided by linear accelerator (UNILAC) were accumulated in the heavy-ion-synchrotron (SIS-18) using multi-multi-turn injection scheme [Dol05, Spi05], cooled down using electron cooling technique and then accelerated up to the particle energy of **59,5 GeV** (250 MeV/u). The four beam bunches existing in the SIS-ring during the acceleration phase were merged into one pulse of about 110 ns (FWHM) duration using adiabatic rebunching and fast bunch rotation techniques, extracted, guided in the beam transport line at the HHT area and delivered to the laser cavity.

The beam pulses were applied as single pulses for quantitative measurements or with a repetition rate of up to about **0,1 Hz** for beam alignment respectively. The accumulated intensity of the Uranium beam was varied from 1 injection (approximately 10^8 particles) up to the maximum of 25 injections which gave a maximum intensity of **$2,5 \cdot 10^9$** particles per bunch. Using electron cooling, transversal emittances of the ion beam was reduced

approximately one order of magnitude (see Chapter 3) which allowed to focus the beam to a more narrow spot and to made it more parallel [Ste93, Dol05, Ste05].

As was already mentioned in Chapter 3 the most part of the ion energy is lost in intermediate materials between beamline and laser cavity. Only the final **16,9 GeV** (71 MeV/u) of the particle energy were actually deposited in the laser gas, which for the maximum intensity of the beam corresponds to a maximum pulse energy of:

$$E_{beam}^{\max} = E_{ion} \cdot I_{beam}^{\max} = 6,7 J \quad (5.1)$$

The beam power deposited in the laser gas is proportional to the number of particles in the beam. Its temporal structure followed to the temporal structure of the ion beam pulse (see Fig.4.6). Thus, the amplitude of the signal from the FCT is proportional to the ion beam power. The relation between these values can be found considering the total beam pulse energy and the integral of the FCT signal. The signal amplitude of **0,1 V** corresponds to the beam power of approximately **6 MW**. The maximum beam power achieved in the experiment was **51 MW**, corresponding to the maximum intensity of the ion beam.

Positioning and focusing of the ion beam was performed with reduced intensity in order to protect the entrance mirror and the beam scintillator from possible damages as mentioned in Chapter 4. Pure Ar (Ar 4.8) was used as a target gas during beam alignment. At the beginning the gas pressure inside the laser cell was set to 4 bar and then reduced step-by-step until the ions range reached the double-cross unit with the diagnostic windows (Fig.4.4b). This occurred at a pressure of approximately **1550 mbar**, and allowed observing and diagnosing the uranium beam in the Bragg-peak region. This topic will be discussed in details below.

As laser gas for the experiment a mixture of the laser excimer premix gas (95,5% Kr + 0,5% F₂) and a buffer gas (Ar 4.8) has been used. Both gases were supplied to the laser cell separately through orifices with changeable diameter and a steady flow was formed in the cell (Chapter 4). The working gas pressure inside the cavity was varied in the range between 1,2 and 2 bar to maximize the laser effect.

Two different mixing ratios of the excimer laser premix and buffer gas have been used in the experiment. One mixture contained **65%** of Ar gas and **35%** of the premix gas. Another mixture was consisted of **40%** of Ar gas and

60% of the premix gas. A procedure of establishing a steady flow in the gas cell as well as detailed calculations of the gases concentration is described in Supplement A.

5.2 Calculation of the ion beam sizes at the cavity entrance

Since the diagnosing of the space distribution of the ion beam intensity was performed only at the end of ion range (Chapter 4), the information about the ion beam sizes near the cavity entrance and they evolution inside the laser cell can be obtained only from simulations.

There are two effects which influence on the ion beam spot size: the beam transporting and focusing in the HHT beamline and the beam straggling due to the ion scattering before and inside the laser cell. These effects are independent from each other and therefore can be calculated separately.

According to the beam transport simulation for the HHT-line [Var05], the ion beam in the experiment was nearly round with diameter (FWHM) of **2,1 mm** at the cavity entrance and **1,2 mm** in the waist, respectively. The focus of the beam was placed at **60 cm** from the cavity entrance.

The ion beam straggling due to ion-atom collisions in the intermediate materials and in the laser gas was calculated using the TRIM code (Chapter 3). All the materials between the HHT-beamline and a laser cell as well as the laser gas (40% of Ar and 60% of excimer laser premix) were added to the TRIM as one multi-layer target. Each layer had the thickness and the density corresponding to the traversed material. The ion beam sizes in this case were **4,2 mm** at the cavity entrance and **17,6 mm** at the end of the ion range respectively (for initially parallel beam with zero-diameter). The sizes were concluded from the spatial distribution of the ions transmitted through the intermediate materials and of the ions stopped in the laser gas⁸. The statistics was 1000 ions and the sizes were valid for more than 80% of particles.

Unfortunately, for multi-layer targets the TRIM can provide incorrect calculations of the ion energy losses, which will result on the total ion range. This occur when the target consists of the layers with a big difference in thicknesses (a few orders of magnitude) and an appreciable difference in densities (for example, gas and solid layers) at the same time. In our case the

⁸ There were two separate calculations, one excluding and one including the laser gas as a target layer.

difference in thicknesses between some layers is more than 4 orders of magnitude (for instance, the air gap of 210 cm and the entrance stainless steel window of 50 μm , see Chapter 3) and the difference in densities is more than 3 orders of magnitude. Thus, the TRIM calculation of all intermediate materials as a multi-layer target (“cascade” calculation) gives the ion energy after propagation these materials (ion energy at the cavity entrance) of 14,1 GeV. While the “layer-by-layer” calculation⁹ gives the ion energy of 16,9 GeV (Chapter 3). So the ion ranges in the laser gas are 66 cm and 84 cm for the “cascade” and the “layer-by-layer” calculations respectively (more than 20% difference).

The “layer-by-layer” calculations also provide us the data about the ion beam straggling in each intermediate material. In a Table 5.1 the increase of the ion beam diameter and the angular spread of ions after propagation of certain material are shown.

Table 5.1: Straggling of Uranium ions with particle energy of 250 MeV/u in the intermediate materials between the beamline and the laser cavity.

Traversed Material		Ion beam diameter (FWHM)	Angular spread of ions ¹⁰
Beamline exit Al-window,	150 μm	54 nm	0,031°
Air gap,	210 cm	1,7 mm	0,076°
Al ₂ O ₃ -scintillator,	600 μm	0,63 μm	0,097°
Stainless steel pressure window,	50 μm	33 nm	0,057°
Entrance quartz mirror,	3,175 mm	8,3 μm	0,328°

From this table one can conclude that the biggest contribution to the straggling of the ion beam is made by the air gap between the beamline and the laser cell and by the thick entrance cavity mirror. This situation can be strongly improved in future experiments (see Chapter 6).

Taking together the beam focusing and the beam straggling in the intermediate materials, one can assume that at the entrance to the laser cavity the ion beam was round with the diameter (FWHM) of **6,3 mm** and the spot size of **0,31 cm²**. The estimated beam diameter at the end of the ion range was **18,8 mm (2,78 cm² spot size)** for the laser gas contained 40% of Ar and 60% of excimer laser premix.

⁹ Each target layer (material) is considered as a separate target with taking into account the energy losses in the previous materials.

¹⁰ Angle of deflection from initial direction of the ion (valid for 80% of particles).

5.3 Ion beam diagnosing with CCD-cameras

As mentioned, it was very important to make sure that the ion beam will be completely stopped in the gas mixture and will not reach the exit cavity mirror. It was also important to measure the beam spot size at the end of ion range or in the Bragg-peak region. From the other hand, one should not place anything on the optical axis of the laser cavity and ion beam diagnostics should not disturb a laser action. Due to just listed reasons gas fluorescence under the ion beam, registered with two CCD-cameras (PixelFly) has been used as a main diagnostic method (see Chapter 4).

5.3.1 Ion energy at cavity entry

Shooting to a pure Ar-gas, the pressure inside the laser cell was set to a value when the uranium beam was stopped in the area observed with both cameras. So one could clearly define the stopping range of the ions inside the resonator with precision better than 1%. In Chapter 3 it was estimated what energy uranium ions should have at the cavity entry, after propagation through all intermediate materials including the entrance mirror (Tab.3.3), using SRIM-code. For the case of our experiment (with initial ion energy of $250 \text{ MeV}/u$) this energy is: $E_0^{ion} = \mathbf{16,9 GeV}$. By knowing the ion range in the laser gas (102 cm), gas composition (here, pure Ar) and gas pressure (1535 mbar) one can calculate the initial ion energy at the cavity entry by another, independent way using libraries of the same code (SRIM). This calculation gives: $E_0^{ion} = \mathbf{17,6 GeV}$ with an accuracy of $\Delta E_0^{ion} = \pm 0,7 GeV$ if we assume an error in the pressure measurement of $\Delta p = \mathbf{50 mbar}$ and the error for the ion range of $\Delta r = \mathbf{1 cm}$. As one can see, both results are very close to each other although the methods are independent. Thus one can conclude: $E_0^{ion} = \mathbf{17 \pm 1 GeV}$ (or $\mathbf{71,4 MeV}/u$) as very reliable value for ion energy.

5.3.2 Ion beam spot size

From the images of gas scintillation induced by the ion beam and recorded with the PixelFly cameras one can obtain a light intensity distribution in a plane lateral to the beam axis (Fig.4.9). An example of such a profile is shown in Figure 5.1 (it was taken at the brightest point on the z-axis

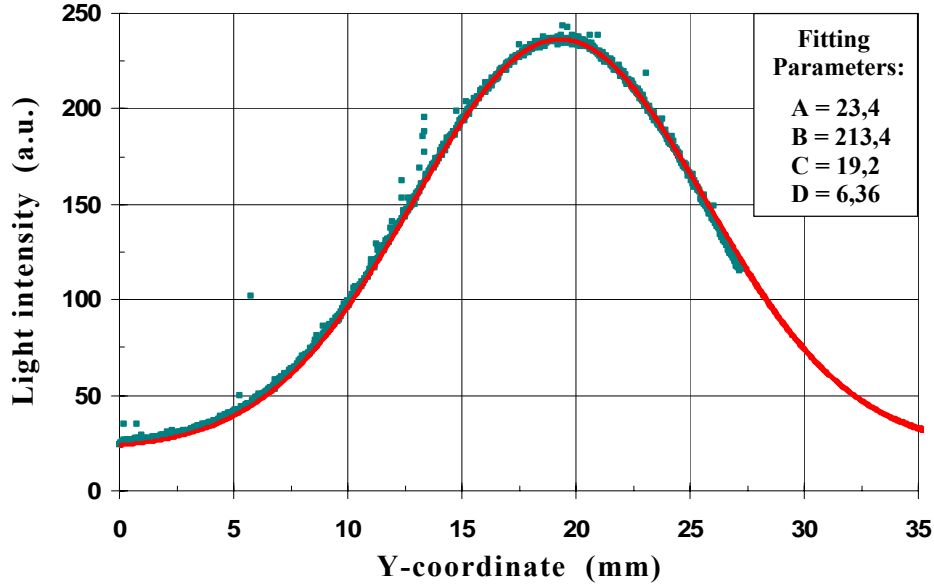


Figure 5.1: Light intensity profile of a uranium beam in Ar recorded by vertical PixelFly camera (green) and Gaussian fitting (red).

and corresponds to the Bragg-peak region). It looks similar to a Gaussian distribution. Fitting the light profiles with Gaussian functions (Equ.5.2) provides information about ion beam position inside the cavity. Before the experiment, images of special alignment lasers, installed on the ion beam axis (Chapter 4), had been recorded with both cameras. This provided exact coordinates of the optical cavity axis for all images. Thus it is possible to check whether the real ion beam axis coincides with the optical axis of the resonator or not.

$$y(x) = A + B \cdot e^{-\frac{(x-C)^2}{2 \cdot D^2}} \quad (5.2)$$

where: A – background level,
 B – signal amplitude in maximum,
 C – position of maximum,
 D – standard deviation (σ).

The width W (full width at half maximum) of the vertical and horizontal profiles could be obtained from standard deviation (σ) using following formula:

$$W = 2 \cdot \sigma \cdot \sqrt{2 \cdot \ln 2} . \quad (5.3)$$

It was measured for the case of pure Ar as well as for the case of the laser gas mixture (40% Ar and 60% excimer laser premix).

In the Ar case, when the gas pressure inside the cell was 1535 mbar, the width W of the horizontal light profile was **15 mm** and of the vertical **13 mm**, respectively. In the second case, when the pressure was 1200 mbar, it was **16 mm** and **14 mm** horizontal and vertical, respectively, which is relatively close to the estimated value for the ion beam size (18,8 mm, see the previous paragraph).

To draw conclusions about the actual ion beam diameters (horizontal and vertical) from these measured widths is not trivial. During propagation through dense gas, uranium ions produce a lot of energetic secondary electrons, which could fly out from the beam region and, in turn, make excitation and ionization processes in the gas. Thus the intensity distribution of the fluorescent light could be appreciably wider than for the ion beam. A real connection between ion beam profile and light profile is unknown. There are a number of experiments performed recently at GSI [Wie01, Ban03, Bec06] related to the ion beam diagnostics in gases. But they dealt with low-pressure or residual gases and some of them with light gases (He_2 , N_2 , etc.). For heavy gases, like Ar and Kr, at high pressures (more than 1 bar) the situation could be different since electron density is much higher.

In the experiment on ion beam profile diagnostics in Ar, performed at the HHT target area in 2004 [Ado05] the light profiles of Ar-I and Ar-II lines have been compared. The main idea was that the cross section of double process, to produce simultaneously ionization and excitation in one collision with the gas atom, for secondary electrons is much (few orders of magnitude) smaller than just of a single process (ionization or excitation). While for heavy ions cross sections of single and double processes are nearly the same. So Ar-II atoms should be produced mostly by the ion beam (in the region of the ion beam) while Ar-I atoms will be produced both by ions and by secondary electrons. And, theoretically, the light intensity profile width of Ar-II is supposed to be more narrow than of Ar-I, but practically, this difference was quite small, less than **0,1 mm**.

However, in our case we can assume the maximum kinetic energy of the secondary electrons produced by uranium ions in the Bragg-peak region using

the following formula¹¹:

$$E_e^{max} \simeq 4 \cdot \frac{m_e}{m_i} \cdot E_i \quad (5.4)$$

where, m_e and m_i are the electron and the ion masses respectively, and E_i is

¹¹ The maximum kinetic energy an electron can obtain in the case of central elastic collision with an ion. This formula can be used only for the non-relativistic case (when the ion velocity v is much less than c).

the ion energy in the Bragg-peak. The energy of an uranium ion corresponding to the Bragg-peak in the Ar gas is about **1,5 GeV** ($6,3 \text{ MeV}/u$)¹², so the maximum energy that electrons can obtain is **12,6 keV**. The range of the secondary electrons with the maximum energy in 1535 mbar of Ar gas was estimated using a CASINO-code (monte CARlo SIMulation of electron trajectory in sOLids) [CASI]. As a result, 90 % of electrons (total statistics was 10000 electrons) with initial energy of 12,6 keV were stopped in a distance of **1,36 mm** from the point where they were created.

Thus, one can conclude that the broadening of the light profile of the ion beam by the secondary electrons does not exceed an accuracy of the profile measurements. So in our case, the width W of the light intensity profile could be assumed as an ion beam diameter. By approximating a transverse shape of the beam as elliptical, one can obtain the size of the ion beam spot (Equ.3.5) in the Bragg-peak region: **1,53 cm²** in pure Ar at 1535 mbar and **1,76 cm²** in the laser gas mixture at 1200 mbar. The estimated beam spot size for the last case was almost 1,6 times bigger (**2,78 cm²**, see Paragraph 5.2).

5.4 Spectrometer data

5.4.1 Demonstration of the laser effect

A first indication of the laser action in the cavity was obtained with the compact spectrometer, observing light emission along the ion beam axis. As soon as the ion beam intensity becomes higher than a certain value and therefore ion beam power density, deposited in the laser gas, becomes higher than the laser threshold for the cavity, strong laser emission on the line at $\lambda = 248 \text{ nm}$ appeared in the spectrum [Ulr06a, Ulr06b, Ado07a]. Examples of on-axis spectra for beam intensities of **1,09·10⁹** (below the threshold) and **1,34·10⁹** particles per bunch (above the threshold) are shown in Fig.5.2. This was also a demonstration of the laser threshold for the resonator. So the ion beam intensity for which the threshold value in the cavity is reached could be approximated as **1,2·10⁹** particles per bunch. Dedicated measurements of the threshold value of the beam intensity have been performed with photodiodes and will be discussed later in this chapter.

As one can see from Fig.5.2, the intensity of broad-band Kr_2F^* spontaneous emission was not changed too much. It increased approximately on 20% with 20% increasing of the ion beam power.

¹² This corresponds to the ion velocity of $\approx 0,12c$ which could be considered as a non-relativistic case.

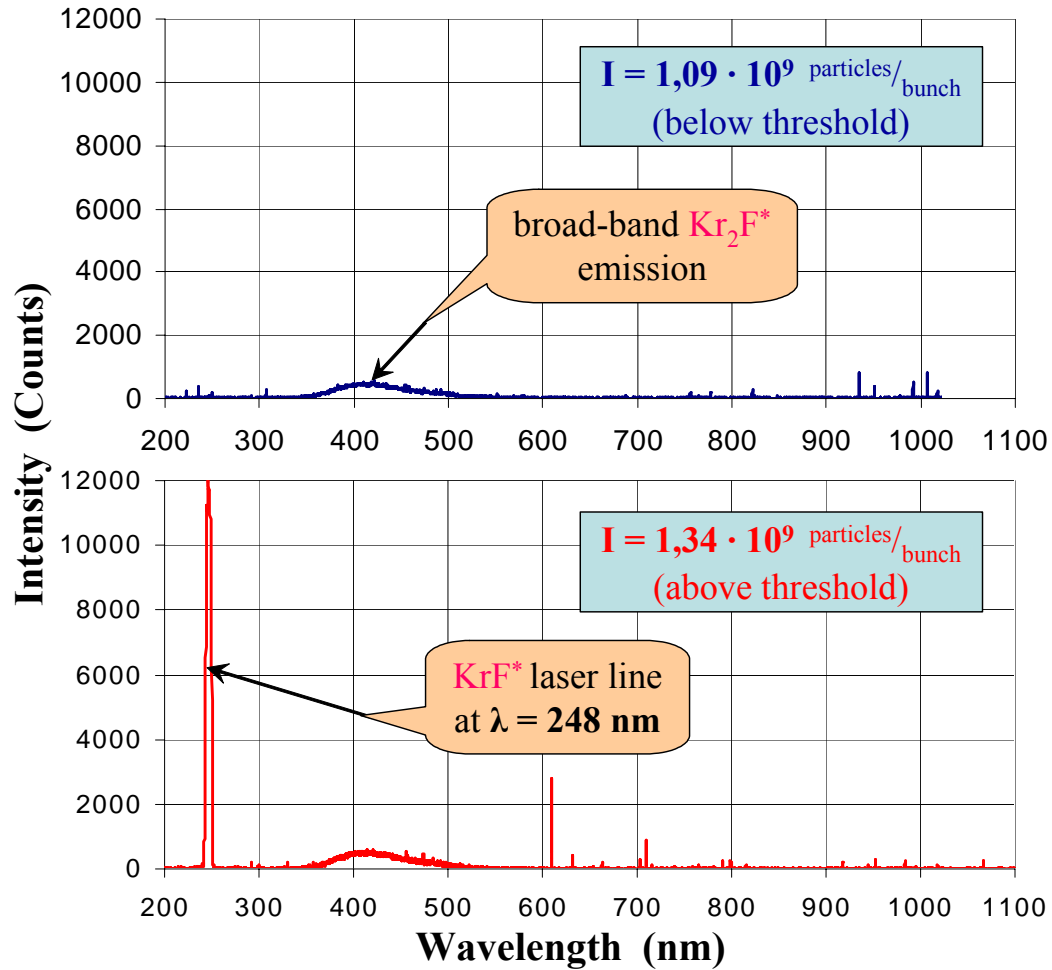


Figure 5.2: Appearance of the laser line on the on-axis spectrum with increasing of the beam intensity above the threshold value.

The laser effect has not only been successfully demonstrated via these spectra, but also proven by various methods:

- *spectral narrowing of the laser line*
- *temporal narrowing of the laser signal*
- *threshold behavior of the laser output intensity*
- *cavity dealignment effect*
- *different response of the light intensity of spontaneous and stimulated emission on the pumping power*

In this section the first method is discussed as it could be observed only with spectrometers. Other methods will be described in a paragraph, dedicated to photodiodes.

5.4.2 Spectral narrowing of the laser line

One of the features, distinguishing laser action from just amplified spontaneous emission, spectral line narrowing, has been observed in the experiment [Ulr06a, Ulr06b, Ado07a]. Spectra of spontaneous emission from the laser gas (observed perpendicularly to the beam axis) as well as laser output spectra were recorded with the same spectrometer. By comparing both spectra one can clearly see a difference between widths of the KrF^* line ($\lambda = 248 \text{ nm}$) in on-axis and in side spectra.

Figure 5.3 shows two spectra (on-axis and side) in a region of laser line. They correspond to pulses with almost the same beam intensity of $1,31 \cdot 10^9$ (side) and $1,33 \cdot 10^9$ (on-axis) particles per bunch, respectively. Obviously, the spontaneous emission line is wider than the stimulated emission line. Unfortunately, relatively low ($2,32 \text{ nm}$) optical resolution of the spectrometer (see Chapter 4) does not allow us to measure this difference quantitatively with good precision.

A natural width of transitions in rare gas halides excimer molecules like KrF^* is very broad (more than 2 nm) in comparison with atomic lines due to the fact that the ground state corresponds to Coulomb repulsion of separated atoms [Bra75, Bra84]. Moreover this broadening is increased by existence of rotation-vibrational states in KrF^* . The width of the laser line is generally

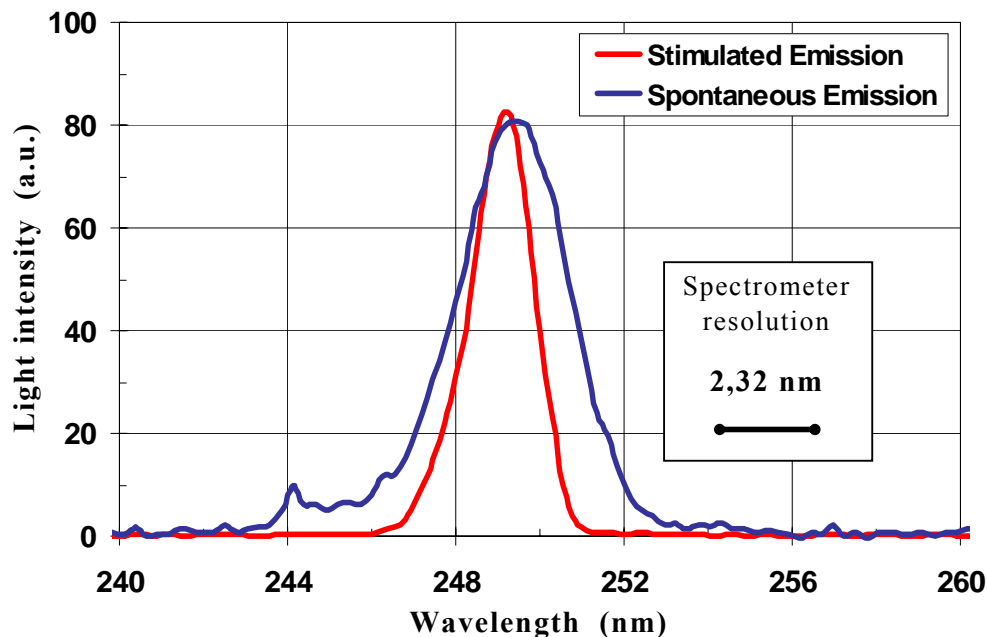


Figure 5.3: Spectral narrowing effect: laser line width is narrower than spontaneous emission line.

narrower than the spontaneous emission line width due to the “gain narrowing” effect and this narrowing increases with increasing amplifier gain [Sie86]. Thus one can expect dependence of the laser line width on the ion beam intensity due to this effect. Unfortunately, low optical resolution of the spectrometer did not allow us to observe this dependence in the experiment.

5.4.3 Dependence of spontaneous emission on gas pressure

The spectrum of spontaneously emitted light from the laser gas contains three main components: emission of the KrF^* band at $\lambda = 248 \text{ nm}$ (laser transition), broad-band emission of Kr_2F^* molecules in a wide region at $\lambda = 350\div 550 \text{ nm}$ and atomic lines of Ar-I and Kr-I in the region $\lambda > 750 \text{ nm}$ (see Fig.5.4). The KrF^* emission has the highest peak amplitude, more than 80% of total light intensity belongs to broad-band Kr_2F^* emission. Atomic lines of Ar-I and Kr-I have two orders of magnitude lower integral intensity than Kr_2F^* . This is due to gas kinetic processes (see Chapter 2).

The main parameters of the most intense atomic lines, observed in spontaneous emission, as well as eventual producers of these lines, taken from NIST atomic database [NIST], are listed in Supplement B.

In order to obtain information about an influence of kinetic processes in the gas on laser activity, pressure dependence of spontaneous emission has

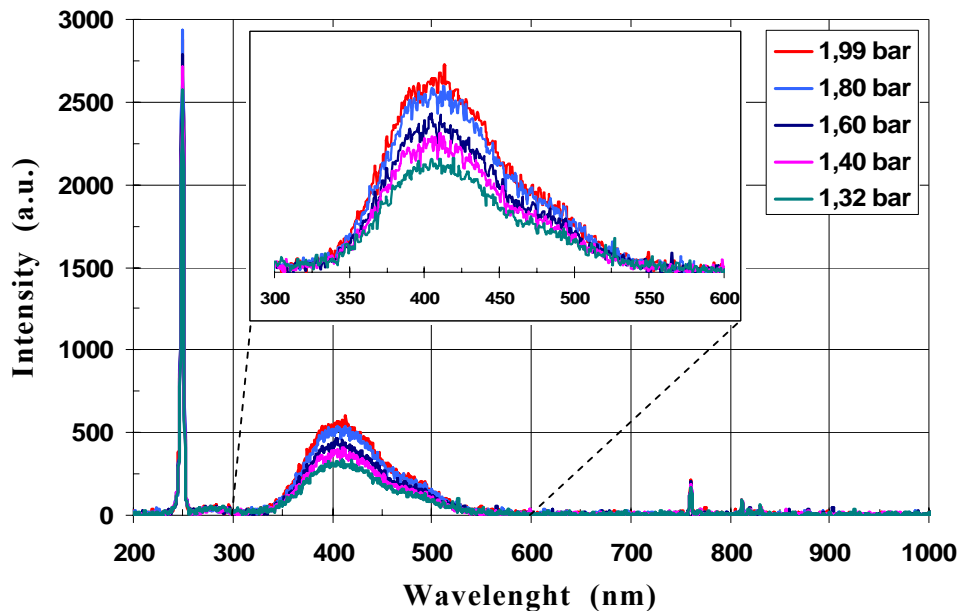


Figure 5.4: Spectra of spontaneous emission at different gas pressures.

been investigated in the experiment [Ado07b]. Unfortunately, direct absolute measurements of the laser emission as a function of the gas pressure was limited by precision due to its strong non-linear dependence on the ion beam intensity.

A mixture of pure Ar gas and excimer laser premix with ratio 40/60 was used as a laser gas. The gas pressure inside the cavity was varied in a region between **1,3** and **2 bar**. In Figure 5.4 examples of spectra, recorded with the spectrometer observing the light emitted perpendicular to the laser axis, for various gas pressures are shown (the insert shows the broad-band Kr_2F^* emission). To avoid “warm pixels” (Chapter 4) and to reduce noise, “medianization on five points” procedure has been performed for each spectrum. Ion beam intensity for each shot was approximately the same, the difference between minimum and maximum total number of particles in the bunches was less than 8%.

A comparative analysis of light intensity changing of three main components of the spectrum has been carried out. As the third component, the atomic line of Kr-I at $\lambda = 760 \text{ nm}$ has been taken, since it is the most intensive of all observed atomic lines (Supplement B). Results of this analysis are represented by the histogram in Figure 5.5. “Emission intensity” is the

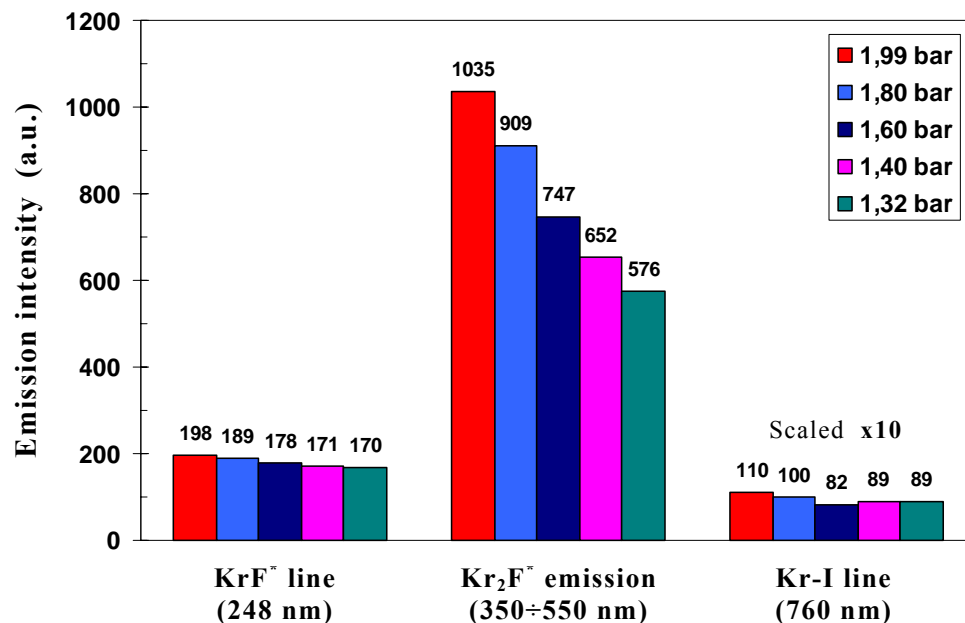


Figure 5.5: Relative emission intensities of the main spectral components (KrF^ , Kr_2F^* and Kr-I) depending on the gas pressure.*

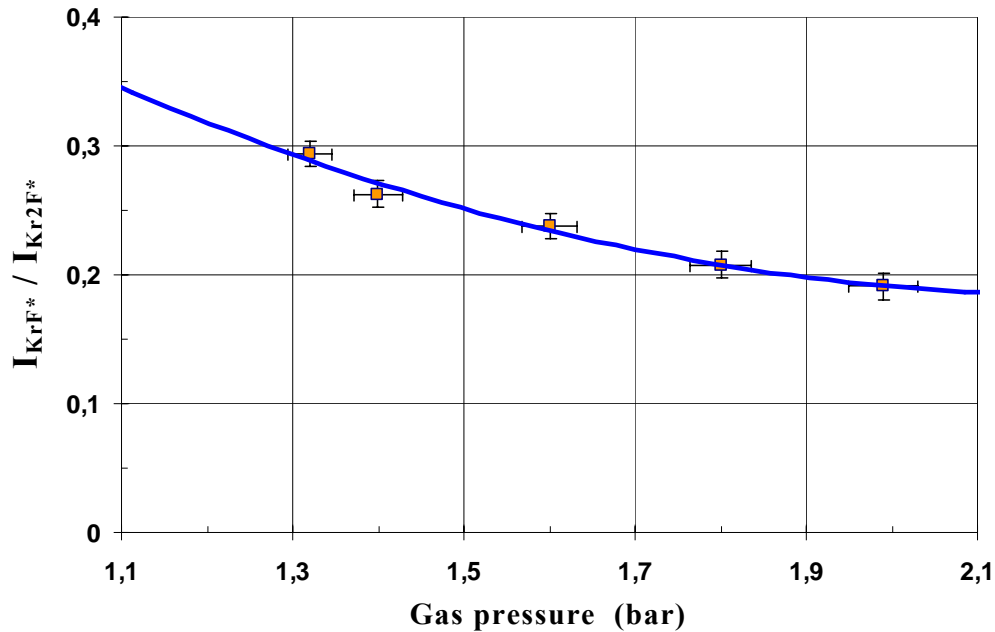


Figure 5.6: Intensity ratio of the KrF^ and Kr_2F^* emissions as a function of gas pressure.*

integrated area under the peaks of the spectra. To correct for ion beam intensity variations, the emission intensity for each shot was corrected for beam intensity, assuming a linear dependence.

As one can clearly see from Fig.5.5, the intensity of Kr_2F^* emission decreases with gas pressure much faster than KrF^* , and light intensity of atomic lines almost does not change. The dependence of the ratio of emission intensities of KrF^* and Kr_2F^* on laser gas pressure is shown on Fig.5.6. The lower the gas pressure inside the cavity, the more intense becomes KrF^* emission in comparison with Kr_2F^* . From this effect one can draw the conclusion that in the pressure region between **1,3** and **2 bar**, laser effect will be maximum for lowest gas pressure.

5.5 Measurements with photodiodes

Measurements of the light intensity of spontaneous and stimulated emission on the laser line ($\lambda = 248 \text{ nm}$) have been performed with two fast UV-sensitive photodiodes. Both of them were equipped with band-pass interference filters for this wavelength ($254 \pm 20 \text{ nm}$) to cut off any accompanying light. One diode was installed near the entrance to the laser cavity, perpendicular to the beam axis at a distance of 29 cm, and observed spontaneously emitted light. Another one was placed near the light collecting

system of on-axis spectrometer, and observed laser light, reflected from a diffusing Al-plate from a distance of 50 cm in order to attenuate the signal and to avoid saturation. A more detailed description of the photodiodes and their characteristics was given in a Chapter 4.

Due to a short rise time (less than 2 ns) these diodes provide data about the temporal structure of spontaneous and laser emission and about time delays between these emissions and the ion beam pulse with high precision. The results of these measurements as well as physical treatments of them are discussed in this paragraph.

5.5.1 Light output from the ion beam intensity

As the second proof of laser action, it was observed the different dependences of spontaneous and stimulated emission intensities from the pumping power [Ulr06a, Ado07a].

In Fig.5.7 the intensity of the spontaneous emission is shown as a function of the number of particles in the ion beam pulses. The experimental points are nicely fitted with linear regression. That indicates that, in the region of ion beam intensity changing, no hydro-dynamical effects, lead to appreciable changes in gas emissivity and gas transparency, appears. The

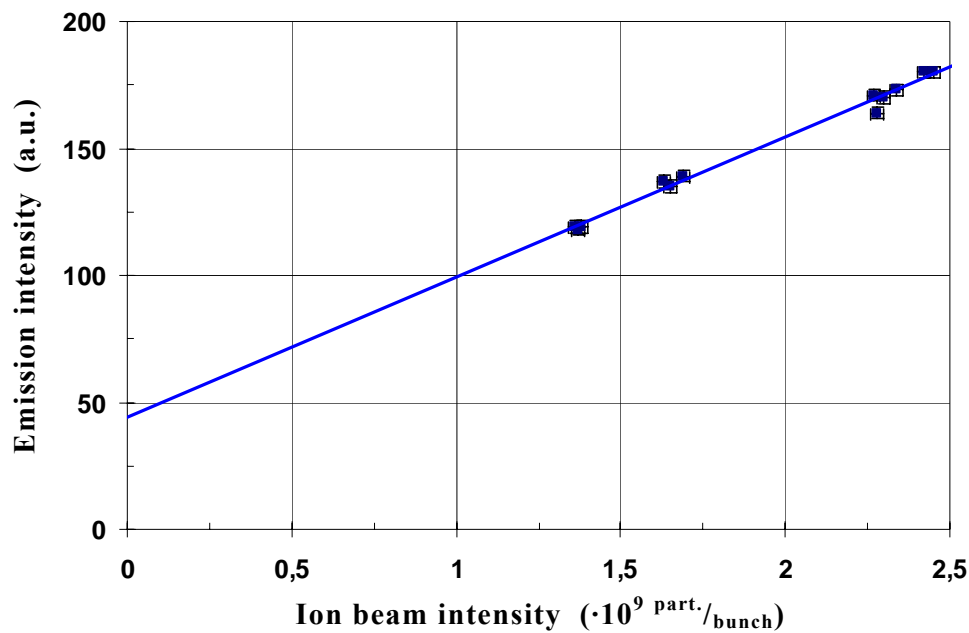


Figure 5.7: Dependence of spontaneous emission on the ion beam intensity with linear fitting.

linear regression starts from a certain value (not from zero-point), this could be explained by the presence of the nuclear- and radiation background registered by the photodiodes during the measurements. The values of X-errorbar for the data points were defined by the accuracy of a current transformer (see Chapter 4), namely $\Delta x = \pm 2 \cdot 10^7$ particles per bunch. A value of standard deviation of each experimental point from the linear regression (σ) has been taken as Y-errorbar values. This deviation was determined by the well-known formula:

$$\sigma = \sqrt{\frac{1}{N-1} \cdot \sum_{i=1}^N (y_i^{exp} - y_i^{lin})^2} = 2,35 \quad (5.5)$$

where: N – number of experimental points
 y_i^{exp} – experimental value for certain x_i
 y_i^{lin} – linear regression value for the same x_i

In contrast to the spontaneous emission, the laser emission has a non-linear dependence of the light output on the ion beam intensity and therefore on the energy deposited in the gas (Fig.5.8). First of all, this dependence has threshold behaviour, which is a clear indication of the laser effect. The value for laser threshold, estimated from the photodiode data, is $1,2 \cdot 10^9$ particles per bunch. Theoretically, this dependence can be expected to be a superposition of

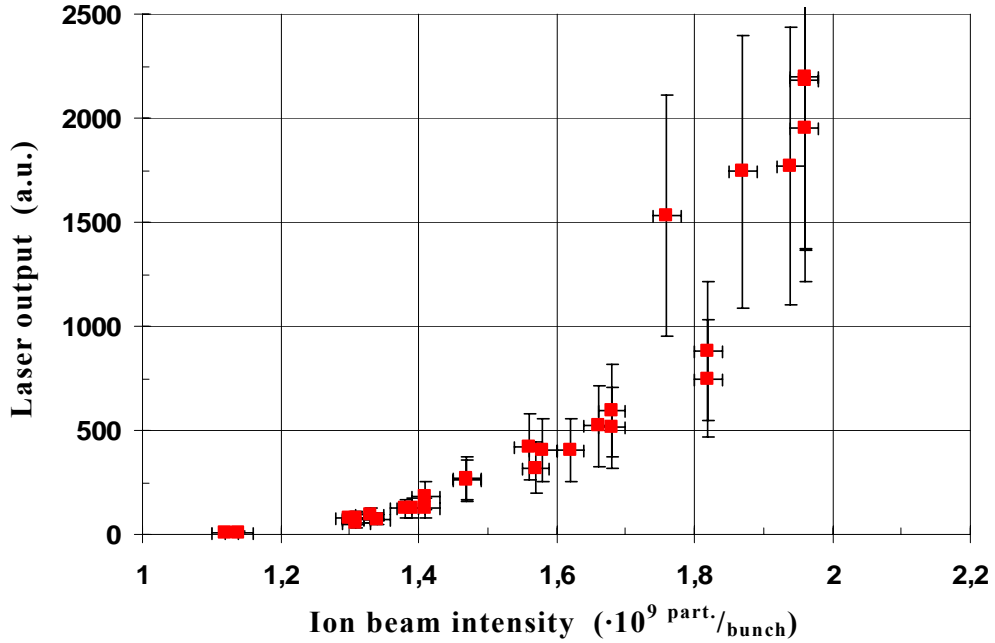


Figure 5.8: Laser output intensity as a function of ion beam intensity.

an exponential growth at the beginning (right above threshold) and a linear dependence, starting from some value for ion beam intensity, where the saturation of laser intensity is reached. Saturation, basically, means that almost all upper states, excited by the ion beam, are depopulated by stimulated emission. In this case, the emission intensity can not increase faster with the number of ions in the beam pulse than the upper states population. To define the exact point (intensity value) of such saturation is not possible for a multi-coherent mode laser. Generally speaking, this dependence should be exponential starting from the threshold value and then transform to linear growth.

It is very difficult to estimate physical errorbars for experimental points, since except the instrumental error of the oscilloscope, which is very small, there are many outside effects, influencing on measurements. So it was decided to take into account a statistical error of the measurements. But, as far as, the statistic of shots with the same beam intensity was very pure, all shots were combined in groups with certain intensity. A single group includes all shots, corresponding to the same number of injections into SIS, for which the beam intensity difference was smaller than the accuracy of intensity measurements. Thus each group involved from 2 to 4 experimental points. As an error for experimental points from a certain group, a standard deviation from the average value inside this group has been used.

Thereby, from Figures 5.7 and 5.8, appreciably different behaviour of emission intensities of spontaneous and laser emissions with pumping power provided by a heavy ion beam could be concluded. Emission intensity and laser output is defined here as the total quantity of light registered over all the emission duration (integrated area under the peak from diode signal). That is clear proof of the laser action in the cavity.

5.5.2 Temporal narrowing of the laser emission

Another proof of laser action is based on the different time structures of spontaneous and stimulated emissions, observed with photodiodes [Ulr06a, Ado07a]. Spontaneous emission lasts around 40 ns longer than the ion beam pulse, which means that afterglow processes in the laser gas play a considerable role. And the rising edge of the spontaneous emission pulse has the same steepness as the leading edge of the ion beam pulse. The duration of the laser output pulse is shorter than for the ion beam and the steepness of its rising edge is higher (Fig.5.9).

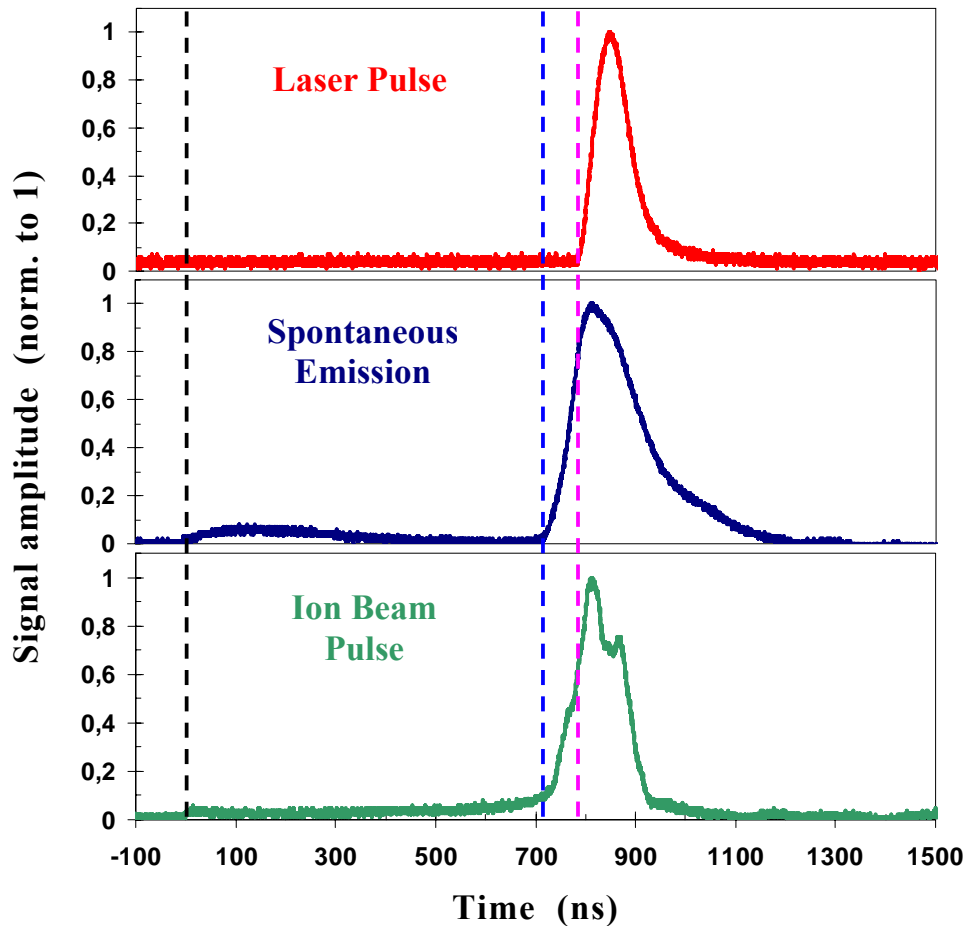


Figure 5.9: Time structures of the ion beam pulse (FCT), spontaneous emission (side diode) and laser emission (front diode). Black dashed line corresponds to the onset of the ion beam pre-pulse, blue – the onset of the main pumping pulse, and pink – the onset of the laser emission.

The time structure of the ion beam pulse, registered with the fast current transformer, as well as the structures of spontaneous and laser emissions are shown in Figure 5.9. Maximum amplitudes of signals were normalized to unity in order to provide a better comparison of the structure. The ion beam pulse has a complex time structure with two maxima, long tails (at the beginning and at the end) and a small pre-pulse at the beginning. This is due to the bunch compression scheme in SIS [Dol05], which allows compressing the ion beam to a very short (110 ns FWHM) pulse. The ion beam pre-pulse was also observed with spontaneous emission (Fig.5.9). This allowed us to associate (link up) in time the signals from the FCT and from the side photodiode since the spontaneous emission starts with the ion beam pre-pulse. The signal from the front photodiode (laser emission) was linked up with the signal from the

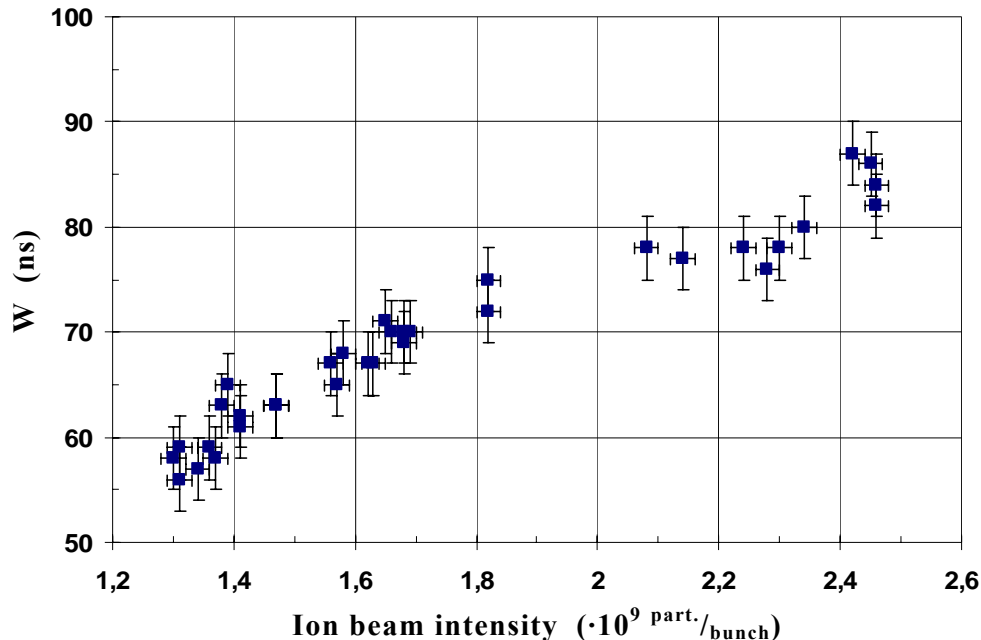


Figure 5.10: Laser pulse duration W (FWHM) as a function of ion beam intensity.

side diode with taking into account time delay due to different cable lengths between the detectors and an oscilloscope. This delay was measured after the experiment and was on the order of **9 ns**. Thus, the procedure described above allowed us to associate in time the ion beam and the laser pulses, and consequently to define the delay of the laser emission with respect to the pumping pulse (see next section).

The effect of laser pulse elongation in time with increasing of the pumping power has been observed in the experiment. The Figure 5.10 shows the dependence of the duration of the laser pulse W (signal from the front photodiode) on the ion beam intensity. As one can see, this dependence is not linear and it could converge to a certain limit with increasing beam intensity. It is important to note that the ion beam pulse duration was around 110 ns for all shots, independent of the number of particles.

The duration of the laser pulse W ranged from **56 ns** near laser threshold to **87 ns** for pumping pulses with maximal intensity ($2,46 \cdot 10^9$ particles per bunch). The data processing error by oscilloscope pictures of the diode signals was around ± 3 ns (ΔY in Fig.5.10). The duration of the spontaneous light emission, registered with the side diode, did not change with ion beam intensity and was on the order of **150 ns** (FWHM). Actually, the length of spontaneous emission was even longer due to a long tail (Fig.5.9), determined

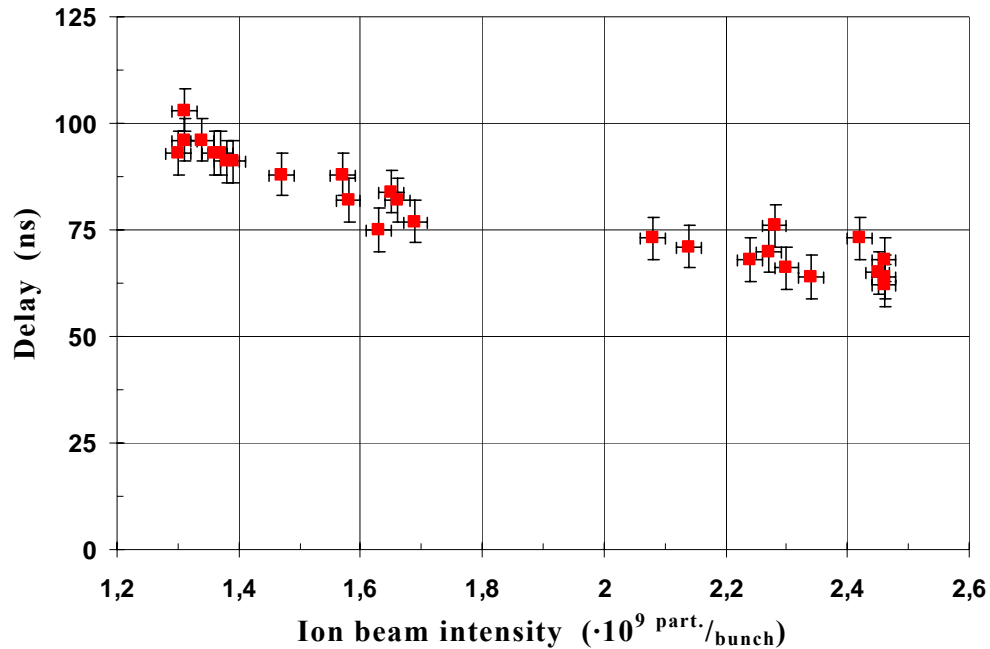


Figure 5.11: Time delays of the laser emission from the ion beam pulse depending on the beam intensity.

by the ion beam's tail from one side and afterglow processes in the gas from another side.

5.5.3 Time delays of the laser emission

As an interesting result, the dependence of the delay of laser light with respect to the pumping pulse as a function of beam power has been observed in the experiment. In Figure 5.11 time delays between signals from FCT and front photodiode are plotted for different ion beam intensities. As far as the ion beam pulse has a complex temporal structure (Fig.5.9), all delays have been calculated not between signal maximums but between onsets of the signals.

The delay of the laser emission was decreasing with increasing ion beam power (number of particles in the pulse). It has amounted about **100 ns** (± 5 ns) for beam intensities slightly above the laser threshold, and it decreased down to **65 ns** (± 5 ns) for maximal available beam intensities (Fig.5.11).

5.5.4 Calculation of the laser output power

Absolute (direct) measurements of the laser output power as well as the total energy of the laser pulse were not possible in this pioneering experiment.

So, it was decided to conclude this information from the data obtained with photodiodes. For this purpose, the front photodiode has been calibrated using a commercial KrF* excimer laser with known beam parameters.

Measurements have been performed at Coherent company (formally TuiLaser). The photodiode and Al diffuser were installed in the same geometry relative to the laser as in the ion beam experiment (keeping the same angles between diode, diffuser and laser axis and the same distance between diode and diffuser). Thus, one could compare diode signals from the ion beam experiment and from the commercial laser in amplitude and conclude the output power of the experimental laser. The commercial laser produced **15 ns** pulses with an average output power of **200 kW**.

An estimated output power of the ion beam pumped laser is **20 kW** over **100 ns** pulse duration for experimental shots with ion beam intensities of $2 \cdot 10^9$ particles per bunch. That means the total energy of the laser pulse was around **2 mJ** versus **3 mJ** for the commercial laser [Ado07a]. The value obtained for the laser pulse energy provides the possibility to calculate a conversion efficiency ε of the ion beam energy into the laser light:

$$\varepsilon = \frac{E_{laser}}{E_{pump}} \cdot 100\% \quad (5.6)$$

where: E_{laser} – total energy of the laser pulse [J]

E_{pump} – total energy of the ion beam pumping pulse [J]

(a detailed calculation of the ion beam energy is given in the next paragraph).

Thus, for ion beam intensities of $2 \cdot 10^9$ particles, the laser efficiency was **0,04%**. For the commercial excimer laser the conversion efficiency of the electrical energy, stored in capacitors, to the laser light is around **2%**. However, an optimization of the laser efficiency was not the goal for this demonstrational experiment. And there are a number of steps for improvement of the laser cavity planned for future experiments, which will increase the laser efficiency several times.

5.6 Calculations of the Laser efficiency from the Threshold value

By a laser threshold it is meant a minimal value of the power density, deposited in the laser medium, when optical gain of this medium is equal to the sum of all losses experienced by light for one round trip in the laser

cavity. In the experiment the laser threshold was reached at an ion beam intensity of $1,2 \cdot 10^9$ particles per pulse (see previous paragraphs) [Ulr06a, Ado07a]. The power density deposited in the gas corresponding to this intensity value of the ion beam is calculated in the next section. Also this paragraph is dedicated to information about pumping efficiency, optical gain and losses in the cavity, which could be concluded from the threshold value.

5.6.1 Laser threshold value

The total energy of the uranium beam deposited in the laser gas was **3,3 J**, with beam intensity of $1,2 \cdot 10^9$ particles and particle energy of **17 GeV** (see Paragraph 5.3). Taking the ion beam pulse duration of **110 ns** (measured with fast current transformer) into account can result in an average beam power of $P_{beam} = 30 \text{ MW}$.

So far as a diagnosing of ion beam spot size was available only near cavity exit, basically in the region of the ions Bragg-peak, the spot size along the cavity were estimated with TRIM code (Chapter 3) with taking into account beam straggling due to ions scattering in all intermediate materials before laser cavity as well as in the laser gas. Thus, gas volume inside the laser cavity heated by the ion beam could be estimated as a volume of a “blunted cone”:

$$V_{beam} = \frac{\pi}{3} \cdot H \cdot (r^2 + r \cdot R + R^2) \quad (5.7)$$

where: H – ions stopping length in the laser gas (**69,3 cm**)

r – beam radius at cavity entry (**0,31 cm**)

R – beam radius at the Bragg-peak region (**0,7 cm**)

So, the uranium beam has deposited its energy in the gas volume of **58,3 cm³**. The specific energy deposited in this case is **16,2 J/g**. The average power density p_d deposited in the gas along the beam axis is **0,51 MW** per cm³ at laser threshold. Thus, as soon as the deposited power density becomes higher than $0,51 \text{ MW/cm}^3$, a net gain per round trip g_{net} (optical gain minus losses) will become positive and the laser effect will appear.

5.6.2 Threshold conditions

As mentioned above, threshold conditions for laser light means that the optical gain per round trip is equal to losses in the cavity. Since, a ground state for KrF^* molecules corresponds to the Coulomb repulsion of Kr and F

atoms (see Chapter 2), the laser gas is transparent for UV-radiation at $\lambda = 248$ nm. Thus one can assume that the light experiences intensity losses only on cavity mirrors. The entrance resonator mirror, coated with Al, has a reflectivity for UV-light around 90% (see Chapter 4). The exit mirror was multi layer coated, highly reflective for $\lambda = 248$ nm, it has more than 99,8% reflectivity for the light with this wavelength. So, one can expect around 10% of intensity losses of the laser light for a round trip inside the cavity and, consequently, optical gain per round trip g_{round} of 10%. By taking into account a single pass length l of the light in active medium of 69,3 cm (the same as ions stopping length, calculated with SRIM code), one can obtain an average value for small signal gain g_{ss} :

$$g_{ss} = g_{round} / 2l = 7,2 \cdot 10^{-4} \text{ cm}^{-1}$$

which corresponds to a value of upper state population N_u (concentration of KrF* molecules):

$$N_u = g_{ss} / \sigma_{st} = 3,6 \cdot 10^{12} \text{ molec./cm}^3,$$

where $\sigma_{st} = 2 \cdot 10^{-16} \text{ cm}^2$ is stimulated emission cross section [Bra84].

For equilibrium conditions, when $\partial N_u / \partial t = 0$, the upper state population is defined by the ratio of pumping rate in a volume unit R_{lu} to total

(summarized) decay rate:
$$N_u = \frac{R_{lu}}{A_{ul} + B_{ul} + C_{ul}}$$

where:

- A_{ul} – spontaneous emission rate [$1/s$]
- B_{ul} – stimulated emission rate [$1/s$]
- C_{ul} – collision decay rate [$1/s$]

(a detailed discussion of the balance equation as well as of all rate values was given in Chapter 3). Since B_{ul} is proportional to the laser intensity I_{las} inside the resonator (Equ.3.10) and in the threshold conditions, when optical gain equal to losses, there is no accumulation of the laser intensity, it could be assumed that B_{ul} is much less than A_{ul} (or $B_{ul} = 0$). Out of this, one can obtain the pumping rate in a cubic unit: $R_{lu} = 1,47 \cdot 10^{21} \text{ s}^{-1} \cdot \text{cm}^{-3}$. A pumping power density p_{pd} could be concluded from pumping rate value by multiplying it on a value of photon energy for $\lambda = 248$ nm ($8 \cdot 10^{-19}$ J): $p_{pd} = 1,18 \text{ kW/cm}^3$.

5.6.3 Laser Efficiency

A conversion efficiency ε of deposited in the gas energy into the laser light, in general, could be split in two independent parts: pumping efficiency ε_{pump} and cavity efficiency ε_{cav} :

$$\varepsilon = \frac{P_{laser}}{P_{beam}} = \frac{P_{laser}}{P_{pump}} \cdot \frac{P_{pump}}{P_{beam}} = \varepsilon_{cav} \cdot \varepsilon_{pump} \quad (5.8)$$

The pumping efficiency is defined as a ratio between pumping power P_{pump} (part of the deposited in the gas energy, which is stored in KrF^* states) and ion beam power. The cavity efficiency is a ratio of laser output power P_{laser} to the pumping power P_{pump} . In principle, ε_{cav} could be also represented as a ratio of stimulated emission rate to the pumping rate, or to the sum of all decay rates (which is the same for equilibrium conditions):

$$\varepsilon_{cav} = \frac{B_{ul}}{A_{ul} + B_{ul} + C_{ul}} \quad (5.9)$$

The reason for such parting is the following: the pumping efficiency depends only on energy transfer and kinetic processes in the gas and does not depend on resonator quality and laser intensity, reached inside the cavity. In contrast to ε_{pump} , the cavity efficiency strongly depends on accumulated laser intensity (parameter B_{ul}) as well as on thermodynamic and physical parameters of the laser gas such as temperature, pressure and mixing ration of excimer laser premix and buffer gas (parameter C_{ul}).

On the basis of threshold conditions ($g_{ground} = 10\%$, $B_{ul} = 0$) the pumping efficiency could be estimated as a ratio of the pumping power density to the total power density, deposited in the laser gas by the ion beam:

$$\varepsilon_{pump} = \frac{P_{pd}}{P_d} = 2,3 \cdot 10^{-3} \quad (5.10)$$

Generally speaking, the value of ε_{pump} could change depending on the ion beam intensity. With increasing the beam intensity, more energy is deposited to the same gas volume and, as a consequence, gas temperature in the heated area increases. This could effect on the rates of various channels of forming and quenching of KrF^* states and consequently on the pumping power. A dependence of the pumping efficiency on the ion beam intensity could be indicated by observing spontaneous emission intensity versus beam intensity, since the intensity of spontaneous emission is proportional to the KrF^* population. But regarding the measurements data (see previous paragraph, Fig.5.7), spontaneous emission intensity was linearly depended on the ion beam intensity. This means that ε_{pump} was not significantly changed with ion beam intensity.

Hereby, knowing measured value of conversion efficiency ε ($4 \cdot 10^{-4}$) for beam intensity of $2 \cdot 10^9$ particles per bunch and assuming the same value for pumping efficiency as for threshold beam intensity value ($1,2 \cdot 10^9$) one can obtain the cavity efficiency value: $\varepsilon_{cav} = 0,17$. Hence it follows the value for stimulated emission rate (from Equ.5.9): $B_{ul} = 1,19 \cdot 10^8 \text{ s}^{-1}$. An equilibrium value for laser intensity, accumulated in the cavity during propagation of ion pumping pulse, could be defined from B_{ul} (Equ.3.10): $I_{las} = 476 \text{ kW/cm}^2$.

The real values for both ε_{pump} and ε_{cav} as well as for the laser intensity I_{las} could be different since the entrance mirror was damaged with the ion beam during the experiment (see next Paragraph) and its reflectivity for 248 nm light is unknown.

5.7 Observation of transversal structure of the laser light

light

In order to observe a transversal distribution of the laser light intensity, a special luminescent screen had been mounted on a diaphragm of adjustment He-Ne laser (Fig.4.7). Under UV-radiation from the excimer laser, the screen emitted fluorescent light in the visible range. This light was observed with a gated video camera, installed near the screen at the angle of about 40° to the laser axis.

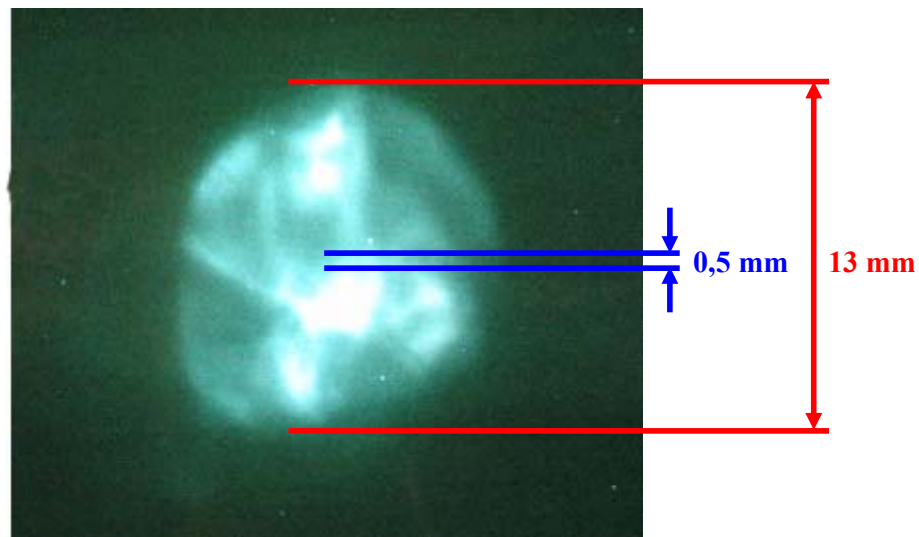


Figure 5.12: Transversal structure of the laser light, recorded with video camera from luminescence screen. Blue – expected laser spot size, Red – size of the illuminated area.

Figure 5.12 shows an example of the transversal structure of the laser beam. A diameter of the illuminated area on the luminescent screen is about **13 mm**, while the expected size of the laser spot was less than **0,5 mm** (Chapter 3). The screen was placed at the distance of 20 cm from the exit cavity mirror. Such a structure was repeated from shot to shot, and it changed only by slight disalignment of the cavity mirrors. Bright spots on the illuminated area correspond to various orders of reflection of the laser light inside the cavity. Quantitative comparison of the light intensity of these spots is not possible, since captured picture was just a “screen copy” of an analog signal from the gated video camera.

One of the possible reasons for such transversal structure of the laser beam could be a damaged spot on the reflective surface of the entrance cavity mirror due to ion beam heating. A detailed discussion of this topic is given in the next paragraph.

5.8 Entrance cavity mirror under the ion beam

As was mentioned in the previous chapter, the optical axis of the laser cavity was coaxial with the ion beam axis and during the experiment the entrance mirror has been traversed by heavy ions. Maximal beam intensity I_{beam} reached in the experiment was $2,5 \cdot 10^9$ particles per bunch. Minimal ion beam spot size, expected on the mirror with taking into account the beam straggling after propagating all intermediate materials on the way to the cavity (exit Al window of the beamline, air drift, pressure window to the laser cell), was: $S_{beam} = 31 \text{ mm}^2$ which corresponds to the beam diameter of **6,3 mm**. Considering, that maximal energy loss of ions $\Delta E/\Delta x$ in the mirror falls on its reflective surface and it is amounted **12,36 GeV** per mm, one can calculate (using Equ.3.3) a maximal value for a specific deposited energy to the mirror: $\varepsilon_{max} = 69 \text{ J/g}$. Thus, a temperature of the mirror (on the reflective surface) could come up to **100°C** after a single shot in the experiment, which together with shockwaves produced by the ion beam in the mirror material can cause a damaging of a thin aluminum reflective layer as well as a MgF_2 protective layer and, consequently, reducing of the mirror reflectivity in the heated area.

During the experiment the reflective surface of the entrance mirror has been damaged by the ion beam, and this affected on the mirror reflectivity and, as a result, on the quality factor of the laser resonator. A damaged spot has been formed after the experiment which had a size of about **3 x 4 mm**, it was located near the center of the mirror and could be clearly seen by the

naked eye. After the experiment the mirror surface has been studied under optical and electron microscopes in order to determine the level of damage on the surface and the reflective coating.

With an optical microscope it was possible to acquire images of the observed area with magnification factors from **5** up to **100**, using various lenses. Also, it had a feature to use different kinds of illumination: front, back and both of them simultaneously. The front illumination is useful for most purposes like observation of scratches, digs and hole size on the surface. The back illumination is essential tool for observing through holes in the non-transparent samples. The use of combination of these kinds of illumination is very convenient for studying the front surface of the sample with highlighting through holes. In our case all three types of illumination have been used.

Images of the damaged spot on the reflective mirror surface acquired with optical microscope, using different magnification factors (from 5 to 50) and different illumination, are represented in Supplement C. As one can see from the images, the reflective Al coating (non-transparent) is hardly damaged in the area heated by the ion beam. The main process responsible for this is recrystallization of Al due to the heating of observed area up to high temperatures [Dob06, Tor76].

A surface analysis of the entrance mirror has been performed with a scanning electron microscope Philips XL-30. It is equipped with field-emission electron gun (Schottky emitter) and accelerating voltage could be varied from **200 V** up to **30 kV**. The highest resolution achieved with Philips XL-30 is **2 nm** (for 30 kV). The magnification factor could be changed in a very wide range: from **15** to **500000**. The microscope has five different detection modes (secondary electron, backscattered electron, cathodoluminescence, X-ray and electron backscatter diffraction), as well as CCD-camera. A spot size of the electron beam could be chosen from seven different values (from 1.0 to 7.0)¹³. The smaller beam spot the better image resolution, but the lower electron beam intensity and therefore weaker target illumination.

Images, acquired with the electron microscope, for both damaged and non-damaged areas on the mirror surface, using different magnification factor (from 500 up to 4000), are compared in Supplement C. From the images it is clearly seen an appearance of small cracks on the outer layer of the mirror

¹³ An information about the electron beam spot size is available from microscope manual only in arbitrary units, but it is noted that the beam diameter approximately doubles every step from smaller spot size value to bigger.

surface (most probably on the MgF₂ protective layer). This argues about intense behavior of recrystallization processes in protective as well as in reflective layers, during the heating by heavy ions. Also, on the damaged area one can see light and dark clusters from the material science literature it could be concluded that light clusters corresponds to dielectric materials like oxides or halides (in our case it could be MgF₂), and dark clusters corresponds to conductive materials (in our case it could be Al) [Wil96, Dob06].

Concluding this paragraph it was observed that heavy ion beam heating produced a significant damage of the reflective layer of the entrance cavity mirror. Unfortunately, it is difficult to conclude without additional measurements how considerable this had affected the mirror reflection coefficient for the excimer laser light ($\lambda = 248$ nm), and therefore one can not calculate the real optical gain achieved in the cavity. However, it becomes clear that there is a need of further investigations of the entrance mirror under ion beam irradiation, in order to select optimal substrate material, reflection coating (from the sense of material and thickness) and protective coating, and to make the mirror more resistant to the ion beam heating.

Chapter 6

Conclusions and Outlook

In this chapter the conclusions from the experiment as well as the main results of the work are summarized. Also, the view on a possible extension of the work on this topic, some suggestions for the next steps and some numerical predictions related to the future experiments are given.

6.1 Main results of the present work

As a main result of this work, the first heavy ion beam pumped UV laser has been successfully demonstrated at the well known laser transition of KrF^* excimer at $\lambda = 248 \text{ nm}$ in the experiment, performed at GSI accelerator facility. The laser threshold value of $0,51 \text{ MW}/\text{cm}^3$, which corresponds to the ion beam intensity of $1,2 \cdot 10^9$ particles per pulse, has been obtained for this specific cavity setup. Laser action has been clearly proofed by the several independent methods, listed below:

- *appearance of the laser line*
A strong laser line appeared on the on-axis spectrum as soon as the ion beam intensity became higher than $1,2 \cdot 10^9$ particles per pulse.
- *spectral narrowing of the laser line*
The spectral width (W) of the KrF^* laser line in the spectrum registered along the beam axis was almost two times narrower than in the spontaneous emission spectrum, registered perpendicular to the beam axis. However, quantitative analysis of this effect was limited due to a pure optical resolution of the spectrometer.
- *temporal narrowing of the laser signal*
A different time structure of the spontaneous emission and the laser signals has been observed. The steepness of rising edge of the laser

pulse was higher than of spontaneous emission signal. The maximum duration of the laser pulse was around **87 ns** (FWHM), corresponding to maximum intensity of ion beam pumping pulses, while the duration of spontaneous emission was independent from the beam intensity and was approximately **150 ns** (FWHM) including afterglow processes which is about 40 ns longer than duration of the pumping ion beam pulse.

- *non-linear response of the laser output intensity on the pumping power*
In contrast to spontaneous emission where the intensity changed linearly with ion beam power, laser emission has showed a clear threshold behavior and non-linear growth of output intensity with increasing number of particles in the pumping pulse.
- *cavity disalignment effect*
Laser effect in the cavity disappeared if one of resonator mirrors was slightly misaligned and it appeared again when the cavity alignment was restored.

The calibration of the photodiode detectors using commercial KrF* excimer laser with known laser pulse parameters made possible to conclude the total energy of the laser pulse obtained in the experiment. It was about **2 mJ** corresponding to the ion beam intensity of $2 \cdot 10^9$ particles per pulse. From this value a conversion efficiency of the ion beam energy to the laser light of **0,04%** has been derived.

Time delays of the onset of the laser emission from the pumping pulse have been measured and analyzed. It was observed that the laser delay was depending on the beam power and it was amounted from **100 ns** to **65 ns** for ion beam intensities between $1,3 \cdot 10^9$ and $2,5 \cdot 10^9$ particles per pulse correspondingly.

Also within the course of the experiments the dependence of spontaneous emission spectra on the gas pressure in a range of **1,3 ÷ 2 bar** was measured. From this it was concluded that the optimal gas pressure for laser experiments in the sense of laser efficiency is the lowest in observed region.

As a general conclusion of the present work, it could be shown that the intensity, space and time characteristics of ion beams, provided by heavy-ion-synchrotron SIS-18 at GSI are sufficient now to pump gas lasers in UV spectral region.

6.2 Suggestions and outlook for future experiments

As a next step in studying short wavelength lasers pumped with heavy ion beams it is planned to reduce the laser wavelength and to extend the laser experiments into Vacuum-UV range of the spectrum ($\lambda < 200$ nm). Also it is planned to proceed to the excimer lasers of the pure rare gases and to use the so called second continua of rare gas excimers as a laser transition: Xe_2^* ($\lambda = 172$ nm), Kr_2^* ($\lambda = 146$ nm), Ar_2^* ($\lambda = 126$ nm), Ne_2^* ($\lambda = 83$ nm) and He_2^* ($\lambda = 80$ nm). These systems are of more fundamental interest than the rare gas halogen lasers because they work with kinetic processes of pure gases. Also, the pure rare gases are technically easier to handle and reduce the safety issues of the experiment. However, these lasers require considerably higher pumping power levels in comparison with rare gas halide excimers, because of the shorter wavelength (for Ne and He cases) and significantly broader laser transition. The emission spectra of the rare gas excimers, observed using low energy electron beam excitation [Fed04], are represented in a Figure 6.1. Some numerical estimations and prediction of the optical gain for the next step of experiments are given in the next paragraph.

Laser action on the second continuum of Ar, Kr and Xe excimers was observed using high energy electron beams for pumping [Hof73, Hug74]. Also

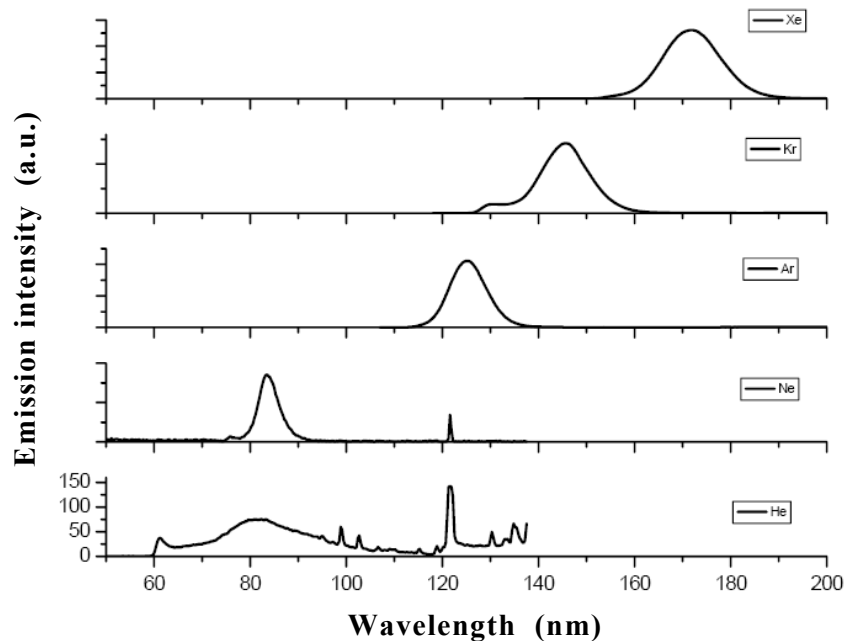


Figure 6.1: Emission spectra of the pure rare gas excimers.

the spontaneous emission of Ne_2^* and He_2^* excimers has been studied spectroscopically using various excitation methods [Kro89, Fed04], but the laser effect on these transitions is not yet obtained. With intense heavy ion beams it should be possible to pump these lasers under well controlled conditions with optical cavities and high repetition rates compared with electron beam pumping. The homogeneous and well controlled excitation conditions will provide data for correlation between pumping power densities and optical gain, which is in a great importance for development discharge pumped rare gas excimer lasers for commercial and industrial purposes.

In order to study the efficiency for the ion beam induced production of coherent as well as incoherent excimer light quantitatively, it is necessary to obtain detailed information about the absolute values of pumping power densities which can be reached using heavy ion beam pumping. So it is planned to study more carefully the stopping and straggling processes of heavy ions in the laser gas. For this purpose the more reliable diagnostics for ion beam size inside the cavity has to be developed.

The use of heavy ion beams as a pumping source may lead to new pumping schemes on the higher lying level transitions and considerably shorter wavelengths (in the extreme UV and X-ray spectral region), which rely on the high cross sections for multiple ionization of the target species. In the framework of the future facility for antiprotons and ion research named FAIR project it is planned to upgrade the existing accelerators at GSI and build up a new heavy ion synchrotron which will be composed of two rings: SIS-100 and SIS-300. They will be capable to produce heavy ion beams with a magnetic rigidity of 100 Tm for fast extraction and 200÷300 Tm for slow extraction [Hof05]. It is expected that FAIR facility will provide the beams of heavy ions which exceed the current beam parameters up to two order of magnitude by intensity and three orders by the beam power [Tah05a, Tah05b]. Thus, it opens wide perspectives for studying short wavelength lasers and for discovering new laser schemes which could be efficiently pumped only with intense heavy ion beams.

6.3 Numerical estimations for future experiments

The experience of the previous experiment has shown that one of the key-problem of heavy-ion-beam pumping is the significant beam straggling in the laser gas cell. This is due to the ions scattering in the laser gas as well as in the intermediate materials between the beamline and the gas cell. As was

mentioned in Chapter 5 the main contribution to the angular spread of the ion beam before entering the cavity was brought in by long (more than 2 m) air section and by thick (3,2 mm) quartz mirror. We can strongly reduce the angular spread of the ion beam at the cavity entry and therefore the beam straggling by decreasing the air gap and the thickness of the entrance cavity mirror. With the present setup it is possible to reduce the air section down to 20 cm without making any changes in the construction. A thin (1,5 mm) Si-wafer can be used as a substrate for the entrance mirror.

In Table 6.1 the energy losses of U-ions in the intermediate materials on a way to the cavity are shown. Calculations were done with the SRIM-code for initial ion energies of 300 and 350 MeV/u . The increasing of the ion beam radius (each radiuses in the case of elliptical beam) after propagation of certain material, estimated with the TRIM-code¹⁴, are also given in the table.

Table 6.1: Ions energy and increasing of the beam radius in the intermediate materials between the beamline and the laser cavity.

Propagated Material	Thickness	Ion Energy after propagation (GeV)		Blowing of the ion beam (for 90% of particles)	
		300 MeV/u (71,4 GeV)	350 MeV/u (83,3 GeV)	300 MeV/u (71,4 GeV)	350 MeV/u (83,3 GeV)
Initial ions energy					
Exit Al-window from the beamline	150 μm	70,51	82,47	58 nm	46 nm
Air gap	20 cm	69,87	81,87	44 μm	40 μm
Stainless Steel pressure window	50 μm	69,06	81,13	27 nm	23 nm
Cavity mirror on Si-wafer	1,5 mm	61,05	73,71	2 μm	1,7 μm
Ion energy at the cavity entrance		61,05 GeV		73,71 GeV	

To reduce the ion beam straggling inside the laser cell more one can proceed to shorter resonator length (shorter beam stopping length) and higher initial ions energy. But this, of course, will require higher gas pressures. Let us consider a new length of the optical resonator in the region between 40 and 60 cm. In order to pump more energy in the laser gas as well as to decrease the energy loss of the ions in the intermediate materials (and, consequently, to

¹⁴ The estimations were performed for each material separately without taking into account ion beam straggling in the previous materials. Each calculation had a statistic of 1000 ions and the results, listed in Table 6.1, are valid for 90% of the particles.

reduce the angular spread of the ion beam at cavity entry) let us increase the initial energy of the ions and consider the cases with 300 and 350 MeV/u .

In Table 6.2 the minimum values for the gas pressure for Xe, Kr, Ar and Ne gases which are necessary to stop Uranium ions with certain initial energy in certain range (in order to fit the resonator length) are given. The present setup can be used with gas pressures up to 10 bar. This limit is defined by the mirror adjustment units (Chapter 4, Fig.4.4) of the laser cavity.

Table 6.2: Values for pressure of various laser gases for the cases with different lengths of the optical resonator and different initial ion energies.

Initial ions energy	Range of the ions in the gas	Gas pressure (bar)			
		Xe ($\lambda = 172 \text{ nm}$)	Kr ($\lambda = 146 \text{ nm}$)	Ar ($\lambda = 126 \text{ nm}$)	Ne ($\lambda = 83 \text{ nm}$)
300 MeV/u	40 cm	9,7	14	25,5	44
	50 cm	7,8	11,2	20,4	35
	60 cm	6,5	9,3	17	29
350 MeV/u	40 cm	13	18,5	34	58
	50 cm	10,2	14,9	27,4	47
	60 cm	8,6	12,4	22,7	39

It is planned to use the optical cavity only in experiments with Xe and Kr gases for the wavelengths of 173 and 146 nm correspondingly. With the other gases (Ar, Ne and He) the laser could be operated only in ASE (Amplified Spontaneous Emission) mode, since where are no mirrors for these wavelengths ($\lambda < 130 \text{ nm}$) commercially available (at least at the present time). Let us consider two cases for further calculations:

	Laser gas	Laser wavelength	Gas pressure	Initial ions energy	Resonator length ¹⁵
Case 1:	Xe	172 nm	8,6 bar	350 MeV/u	70 cm
Case 2:	Kr	146 nm	9,3 bar	300 MeV/u	70 cm

since they do not require significant changes in the present setup.

The expected sizes of the ion beam inside the cavity could be the following: **2,3 mm** (FWHM) at the cavity entry and **9,8 mm** and **8,7 mm** (FWHM) at the Bragg-peak region for Xe and Kr cases respectively. These

¹⁵ The distance between cavity mirrors (resonator length) should be bigger than the ions stopping length in the cavity in order to avoid the heating of the exit mirror with the ion beam.

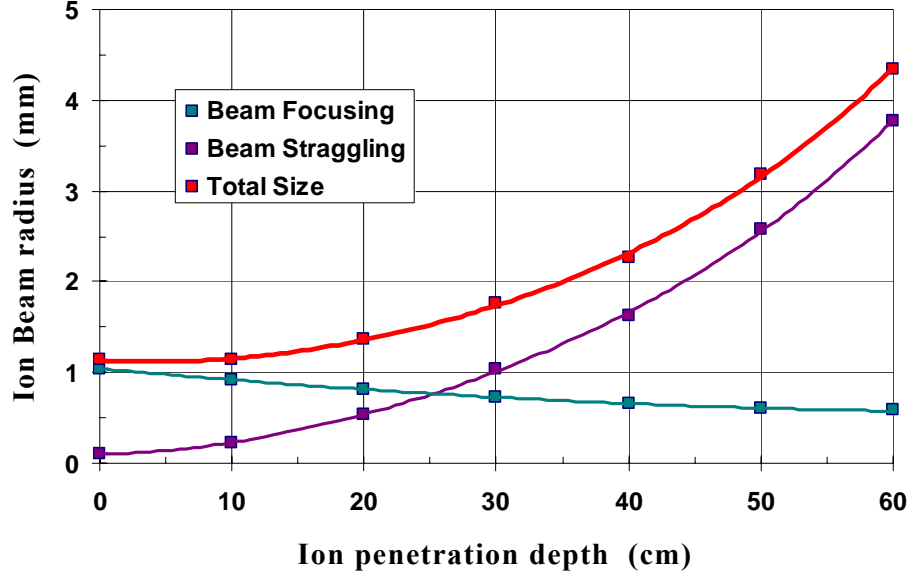


Figure 6.2: Ion beam envelope inside the gas cell for U-ions with initial particle energy of 300 MeV/u in Kr gas (9,3 bar)

sizes are considerably smaller in comparison with beam sizes which we had in the experiment (6 mm at the entry and around 15 mm at the Bragg-peak region, see Chapters 3 and 5) owing to reducing of the ion beam straggling in the intermediate materials and in the laser gas.

In Figure 6.2 the dependence of the ion beam radius from the penetration depth in the laser gas for the Kr-case is shown. The total beam radius (red curve) is determined by the beam focusing (teal curve) and by the beam straggling (violet curve). The parameters of the beam focusing were used the same as was in the experiment (Paragraph 5.2). The beam straggling in the laser gas was calculated using the TRIM-code.

If we assume the maximum intensity of the ion beam of $4 \cdot 10^9$ particles per pulse (such intensity was obtained at GSI for U-beams in 2003 [Var03], see Chapter 4), the average (along the beam axis) energy density deposited in the laser gas will be $4,1 \text{ J/cm}^3$ and $4,08 \text{ J/cm}^3$ for Xe and Kr cases respectively. Which gives 41 MW/cm^3 and $40,8 \text{ MW/cm}^3$ of the peak power density for the case of 100 ns (FWHM) ion beam pulse. These values are more than 30 times higher than the maximum value of deposited power density of $1,1 \text{ MW/cm}^3$ achieved in the experiment (Chapter 5).

Assuming the efficiency of the upper state population ε_{up} of 10% [Hut80, Sak87] one can obtain the part of the deposited in the gas energy which goes to produce the excimer molecules per time unit and volume unit: $4,1 \text{ MJ/s}\cdot\text{cm}^3$

and $4,08 \text{ MJ}/\text{s}\cdot\text{cm}^3$ for Xe and Kr cases, respectively. The ionization energies of xenon and krypton atoms are 12 eV and 14 eV, respectively [NIST]. From these values the pumping rate R_{lu} (a number of upper states produced in a volume unit per time unit) could be concluded: $2,14\cdot 10^{24} \text{ s}^{-1}\cdot\text{cm}^{-3}$ for Xe and $1,82\cdot 10^{24} \text{ s}^{-1}\cdot\text{cm}^{-3}$ for Kr. Since the lifetime of the excimer states are: 5,5 ns for Xe_2^* [Ket74] and around 6 ns for Kr_2^* [Koe75, Bon80, Smi83], the spontaneous emission rates will be: $1,82\cdot 10^8 \text{ s}^{-1}$ and $1,67\cdot 10^8 \text{ s}^{-1}$ for Xe and Kr cases, respectively (Equ.3.9).

To determine the collisional quenching rate of excimer molecules, let us assume the worst case, when the quenching of the excited states occurs every collision with an atom or a molecule. In this case, the quenching rate will be equal to the average collision frequency ν_{coll} , which in turn is defined by the average velocity $\langle v \rangle$ and the mean free path L_{free} of the particles:

$$\nu_{coll} = \frac{\langle v \rangle}{L_{free}} \quad (6.1)$$

The average velocity can be found using the following formula:

$$\langle v \rangle = \sqrt{\frac{3 \cdot R \cdot T}{M}} \quad (6.2)$$

where: R – molar gas constant,
 T – gas temperature,
 M – molar mass of the rare gas,

so for the room temperature it is 238 m/s and 298 m/s for Xe and Kr cases, respectively. The mean free path is calculated using the following formula:

$$L_{free} = \frac{0,707}{\pi \cdot d^2 \cdot n} \quad (6.3)$$

where: d – diameter of the rare gas atom,
 n – concentration of atoms (density),

it is approximately 0,52 μm for the Xe case and 0,56 μm for the Kr case. Thus, the estimated in this way collisional quenching rate is $4,6\cdot 10^8 \text{ s}^{-1}$ and $5,3\cdot 10^8 \text{ s}^{-1}$ for Xe and Kr cases, respectively.

Thereby, the upper state population N_u for Xe case will be $3,33\cdot 10^{15}$ molecules per cm^3 and for Kr case – $2,61\cdot 10^{15}$ molecules per cm^3 (Equ.3.7) The stimulated emission cross section σ_{st} for Xe_2^* is assumed to be $1,5\cdot 10^{-17} \text{ cm}^2$ and for Kr_2^* it can be estimated around 10^{-17} cm^2 [Hut80]. The photons emitted by Xe_2^* as well as by Kr_2^* molecules have sufficient energy

to ionize other excimers (Xe_2^* and Kr_2^* , respectively), thereby reducing the gain of the laser. The cross section of this photoionization process is estimated to be $2 \cdot 10^{-18} \text{ cm}^2$ for Xe_2^* and around 10^{-18} cm^2 for Kr_2^* [Hut80, Eck88]. Thus, by taking into account the photoionization as a competitive process to the stimulated emission, the small signal gain g_{ss} is predicted to be about **4,3%** per cm and about **2,3%** per cm for Xe and Kr cases, respectively.

Assuming the length of the active medium in the resonator of 60 cm (range of the ions in the laser gas) for both cases, and using the highly reflective cavity mirrors with reflectivity of 96% for $\lambda = 172 \text{ nm}$ (Xe case) [Eck88], and about 85% for $\lambda = 146 \text{ nm}$ (Kr case) [Sas01], one can obtain the net gain g_{net} per single trip of **2,54** for the Xe_2^* and **1,22** for the Kr_2^* , respectively. Since for 100 ns pumping pulse one can assume around 42 single trips, the clear laser action can be expected for both cases.

Over the last few years there were a number of works, reported about the laser action in pure rare gas excimers achieved using the discharge and the electron beam pumping [Eck88, Koc95, Nee96, Sas01]. Kochetov and Lo in their work [Koc95] achieved the power deposition with a self-sustained discharge up to 13 MW/cm^3 in binary mixtures of Xe/Ne and Xe/He and a net gain of the Xe_2^* laser up to 4,5% per cm. In 2001 Sasaki et al. had demonstrated the Kr_2^* laser oscillation with the self-sustained discharge pumping of the pure Kr at 10 bar pressure [Sas01]. They obtained the net gain coefficient of 1,1% per cm and the deposited power of more than 20 MW/cm^3 was estimated. Thereby, with our estimations, we definitely can expect the successful laser action for both Xe and Kr cases.

Supplement

A. Calculation of gases concentrations in the laser gas mixture

It was necessary to know the mixing ratio of gases in the mixture in order to calculate the range of the ions and the ion beam straggling in the laser gas, and then to conclude the energy density deposited in the laser gas. Since the continuous flow was established in the gas cell, the mixing ratio of gases can be concluded from the ratio of the flow rates of the excimer gas and the buffer gas respectively. During the experiment it was not possible to measure the flow rates of each gas component directly. However, this ratio can be obtained from the procedure of establishing a steady flow in the laser cell. This procedure as well as the flow rates calculation is described below.

Step 1:

As a first step a constant flow of pure Ar was set at a pressure of 1,6 bar. Stabilization of the gas flow basically means a parity of an input and output flow rate:

$$F_{in} = F_{Ar} = F_{out} \quad (\text{A.1})$$

The flow rate F is proportional to the orifice cross section S and the pressure difference ΔP between both sides of the orifice:

$$F = S \cdot \Delta P \cdot K(T, M) \quad (\text{A.2})$$

where: $K(T, M)$ – some coefficient depending on gas temperature and molecular weight.

In spite of the fact that both input orifices for Ar and for Excimer gas as well as output orifice were controllable, the values of their cross sections were unknown. The pressure difference for the gas inlets were defined by pressure reducers installed on each gas bottle and pressure inside the gas cell. Preset value for both reducers was the same: 7,2 bar. For the gas outlet ΔP was determined by the pressure inside the cell and atmospheric pressure. So there was no way to set the pressure in the laser cavity at constant flow less than one atmosphere without an additional evacuating system.

Thus equations (A.1) and (A.2) give:

$$S_{Ar} \cdot \Delta P_{Ar} \cdot K_{Ar}(T, M) = S_{out} \cdot \Delta P_{out} \cdot K_{Ar}(T, M)$$

where: $\Delta P_{Ar} = 5,6$ bar and $\Delta P_{out} = 0,6$ bar.

And therefore the ratio of the orifice cross sections is following:

$$S_{out} = \frac{\Delta P_{Ar}}{\Delta P_{out}} \cdot S_{Ar} = 9,33 \cdot S_{Ar} \quad (A.3)$$

So it can be concluded that stabilization of the Ar flow at the conditions described above required the output orifice to be 9,33 times larger than the input orifice.

Step 2:

As a second step the orifice for the excimer gas was opened and the gas flow was stabilized at 2 bar pressure without changing orifice's size for Ar as well as the output orifice. For this case equation (A.1) will be extended:

$$F_{in} = F_{Ar} + F_{Exc} = F_{out}$$

Pressure differences in the second step were: $\Delta P_{Ar} = \Delta P_{Exc} = 5,2$ bar and $\Delta P_{out} = 1$ bar. Thus the ratio of orifice cross sections for excimer gas will be

defined as:

$$S_{Exc} = \frac{9,33 \cdot K_{Ar+Exc} - 5,2 \cdot K_{Ar}}{5,2 \cdot K_{Exc}} \cdot S_{Ar} \quad (A.4)$$

The dependence of the coefficients K on the molecular weight of the gas for a

fixed temperature is [Scot, LLas, Fuj75]: $K_{gas} \sim \sqrt{\frac{1}{M_{gas}}}$

So, as far as the temperature T is the same for all gases in mixture, one can calculate the ratios between these coefficients for different gases:

$$K_{Exc} = \sqrt{\frac{M_{Ar}}{M_{Exc}}} \cdot K_{Ar} = 0,69 \cdot K_{Ar} \quad (A.5)$$

As for K_{Ar+Exc} , in the first order of approximation let us assume equal parts of Ar and excimer gases:

$$K_{Ar+Exc} = \sqrt{\frac{M_{Ar}}{0,5 \cdot M_{Ar} + 0,5 \cdot M_{Exc}}} \cdot K_{Ar} = 0,8 \cdot K_{Ar} \quad (A.6)$$

Now if we put together equations (A.4), (A.5) and (A.6), we will obtain the following ratio:

$$S_{Exc} = 0,63 \cdot S_{Ar}$$

which in combination with K -ratio (A.5) will determine a ratio between flow rates for Ar and excimer gases:

$$F_{Exc} = 0,44 \cdot F_{Ar} \quad (A.7)$$

From the last equation one can directly conclude the mixing ratio of gases in the laser cell in some (short) time after forming the steady flow: **70%** of Ar and **30%** of excimer mixture. But this is a result of a first order of approximation when we assumed equal parts of the gases (50% of Ar and 50% of excimer mixture). If we put this result back into equation (A.4) and make a second iteration we will get a new ratio between the flow rates:

$$F_{Exc} = 0,55 \cdot F_{Ar}$$

which in terms of the mixing ratio means: 64% of Ar and 36% of excimer mixture.

After several iterations final ratios for orifices and flow rates have been obtained:

$$S_{Exc} = 0,77 \cdot S_{Ar}; \quad F_{Exc} = 0,53 \cdot F_{Ar} \quad (A.8)$$

And consequently the definitive mixing ratio of gases inside the cell is: **65%** of Ar and **35%** of excimer (95,5% Kr + 0,5% F₂). So this was one mixing ratio which has been used in the experiment and another one has been established by the next two steps described below.

Step 3:

The outlet orifice S_{out} was increased to stabilize the gas flow inside the cavity cell at **1,6 bar**. In addition S_{Ar} and S_{Exc} were not changed. Thus the parameters of inlet and outlet flows were following:

$$\begin{aligned} \Delta P_{Ar} = \Delta P_{Exc} = 5,6 \text{ bar}; \quad \Delta P_{out} = 0,6 \text{ bar}; \\ S_{Exc} = 0,77 \cdot S_{Ar}; \quad K_{Exc} = 0,69 \cdot K_{Ar}; \quad K_{Ar+Exc} = 0,85 \cdot K_{Ar} \end{aligned}$$

(obviously Ar-Excimer ratio does not depend on the pressure in the gas cell if the inlet orifices do not change, as far as pressure differences ΔP_{Ar} and ΔP_{Exc} are equal). From these parameters one could simply conclude a new ratio for the outlet orifice:

$$S_{out} = 16,8 \cdot S_{Ar} \quad (A.9)$$

Step 4:

And a final step of the procedure of receiving a second gas mixing ratio is increasing the excimer inlet orifice until the gas flow will stabilize at a pressure of **2 bar** inside the cell.

Thus the new flows parameters are:

$$\Delta P_{Ar} = \Delta P_{Exc} = 5,2 \text{ bar} ; \quad \Delta P_{out} = 1 \text{ bar} ;$$

$$S_{out} = 16,8 \cdot S_{Ar} ; \quad K_{Exc} = 0,69 \cdot K_{Ar}$$

By analogy with Step 2 (A.4) the expression for the new inlet orifice for excimer gas will be following:

$$S_{Exc} = \frac{16,8 \cdot K_{Ar+Exc} - 5,2 \cdot K_{Ar}}{5,2 \cdot K_{Exc}} \cdot S_{Ar} \quad (\text{A.10})$$

where K_{Ar+Exc} is unknown. But for the first iteration one can take into account a previous value which corresponds to the mixing ratio 65% Ar and 35% excimer.

Thus, solving equation (A.10), one gets: $S_{Exc} = 2,53 \cdot S_{Ar}$, and consequently, a new mixing ratio: 36% Ar and 64% excimer which is almost opposite to the first assumption. Return this result to (A.10), make a few more iterations, and finally the ultimate ratios for orifices and flow rates between buffer gas Ar and pure excimer mixture are obtained:

$$S_{Exc} = 2,18 \cdot S_{Ar} ; \quad F_{Exc} = 1,51 \cdot F_{Ar} \quad (\text{A.11})$$

which in terms of gases mixing ratio means **40%** of Ar and **60%** of excimer.

B. Observed atomic spectral lines

There were several measurements when the light collecting system of the side spectrometer was placed very close to the ion beam axis. The recorded spectra of the spontaneous emission for these measurements had saturation of the signal for the KrF^* line (248 nm) as well as for the Kr_2F^* band (350÷550 nm). But on the other hand, on these spectra it was possible to distinguish low intensity atomic lines. An example of such a spectrum is shown on Figure B.1.

The lines observed in the spectrum are listed in a table below. The relative emission intensity (integral) as well as eventual producers is specified across each line. The transition parameters for eventual line producers are taken from NIST (National Institute of Standards and Technology) atomic spectra database [NIST].

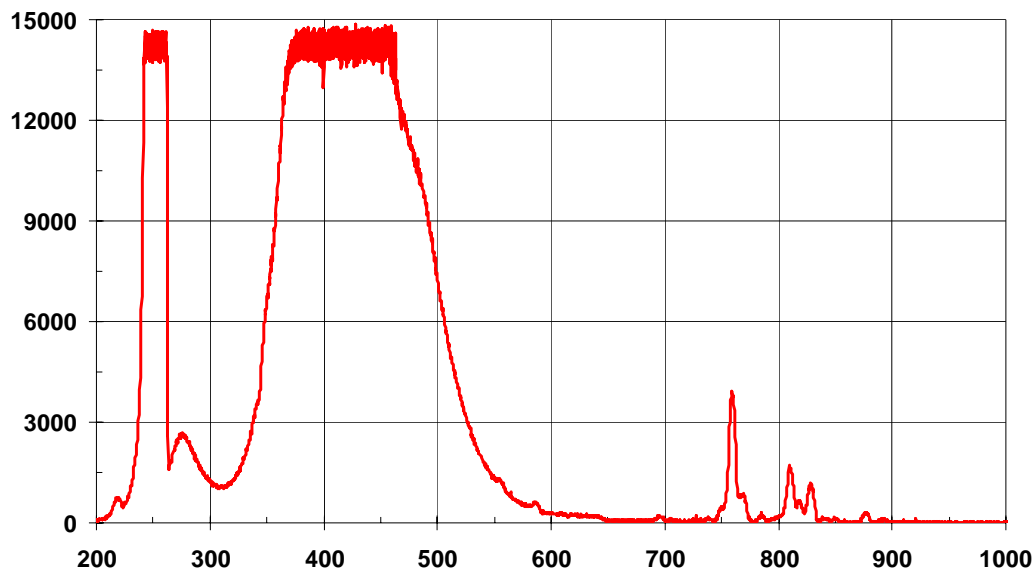
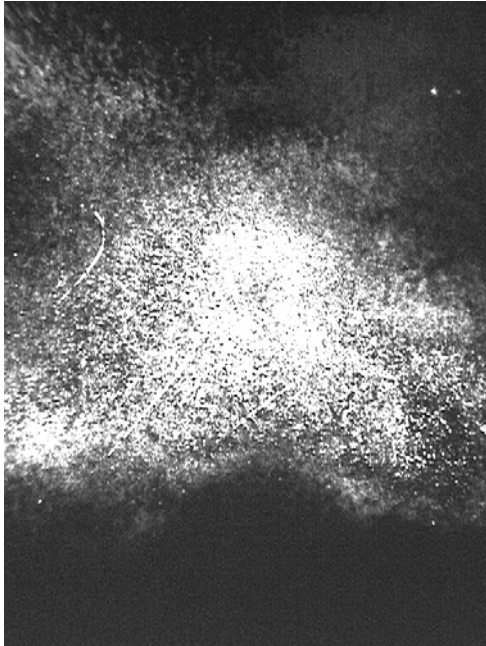


Figure B.1: Spontaneous emission spectra of the laser gas (65% Ar – 34,8% Kr – 0,2% F₂) at the pressure of 1,6 bar for the ion beam intensity of $2,28 \cdot 10^9$.

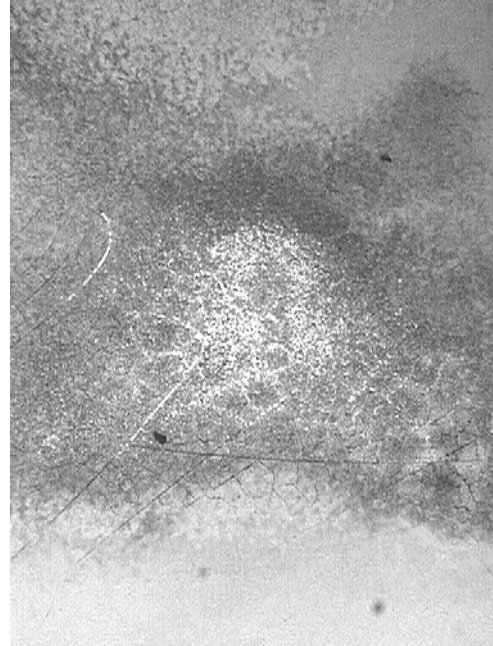
Observed Lines		NIST data				
λ (nm)	Relative intensity	Eventual producer	λ (nm)	Relative Intensity	Trans. Probability A_{ki} (10^8 s^{-1})	Life Time τ (ns)
219	700	Ar III	219,2	15	-	-
276	2700	Ar III	276,2	7	-	-
		Kr IV	277,5	6	-	-
556	400	Ar I	555,9	25	0,014	714
		Kr I	556,2	500	0,003	3,3 us
		Kr I	557,0	2000	0,021	476
587	400	Ar I	588,3	15	0,012	833
		Kr I	587,1	3000	0,018	556
696	250	Ar I	696,5	10000	0,064	156
750	350	Ar I	750,4	20000	0,445	22,5
		Ar I	751,5	15000	0,402	24,9
		Kr I	748,7	100	-	-
759	6200	Ar II	758,9	-	0,107	93,5
		Ar I	763,5	25000	0,245	40,8
		Kr I	758,7	1000	0,51	19,6
		Kr I	760,2	2000	0,31	32,3
771	1000	Ar I	772,3	15000	0,052	192
		Ar I	772,4	10000	0,117	85,5
		Kr III	773,6	250	-	-
785	300	Ar I	786,8	-	0,004	2,5 us
		Kr I	785,5	800	0,23	43,5
810	2500	Ar I	810,4	20000	0,25	40
		Ar I	811,5	35000	0,331	30,2
		Kr I	810,4	4000	0,13	76,9
		Kr I	811,3	6000	0,36	27,8
818	400	Kr I	819,0	3000	0,11	90,9
828	1800	Ar I	826,5	10000	0,153	65,4
		Kr I	828,1	1500	0,19	52,6
		Kr I	829,8	5000	0,32	31,3
841	200	Ar I	840,8	15000	0,223	44,8
		Ar I	842,5	20000	0,215	46,5
		Kr I	841,2	100	-	-
850	200	Ar I	852,1	15000	0,139	71,9
		Kr I	850,9	3000	0,24	41,7
877	450	Ar I	876,2	-	0,01	1 us
		Ar II	877,2	20	-	-
		Kr I	877,7	6000	0,27	37
892	140	Ar II	892,6	-	0,006	1,7 us
		Kr I	892,9	2000	0,37	27

C. Damaged reflective area on the entrance mirror

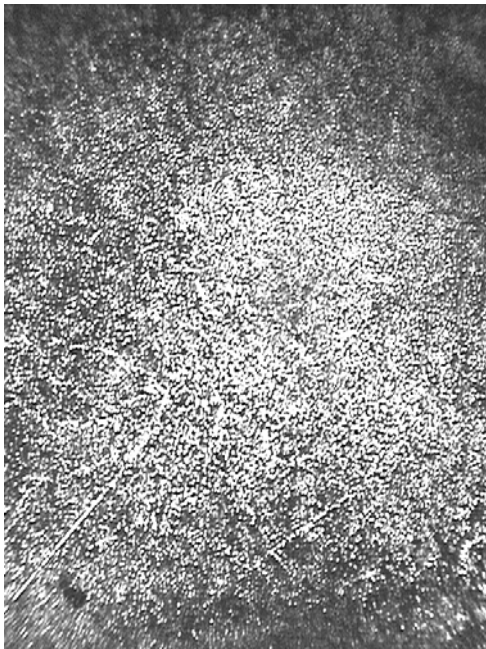
1. Images acquired with optical microscope.



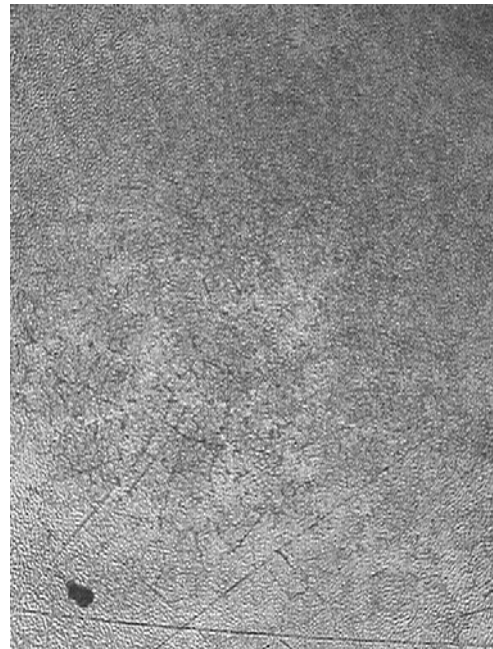
Magnification factor: 5x
Backlighting: back



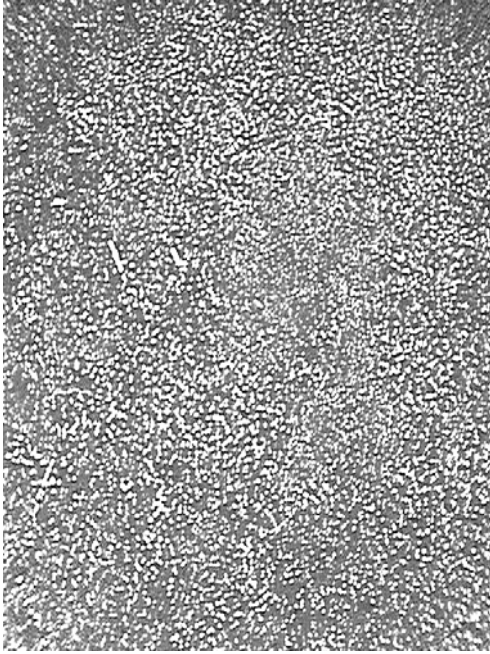
Magnification factor: 5x
Backlighting: front + back



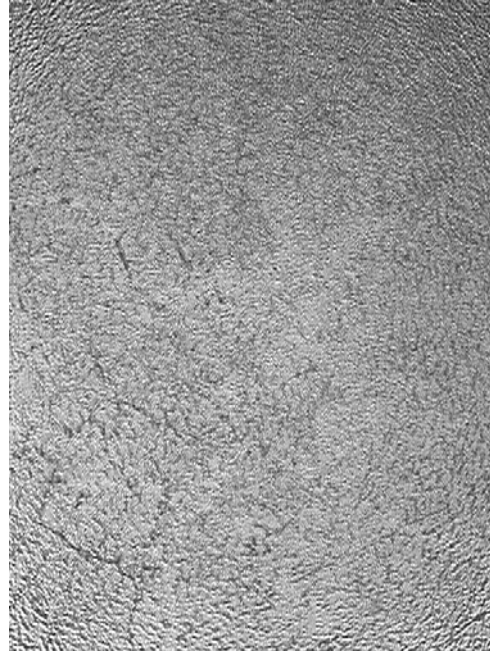
Magnification factor: 10x
Backlighting: back



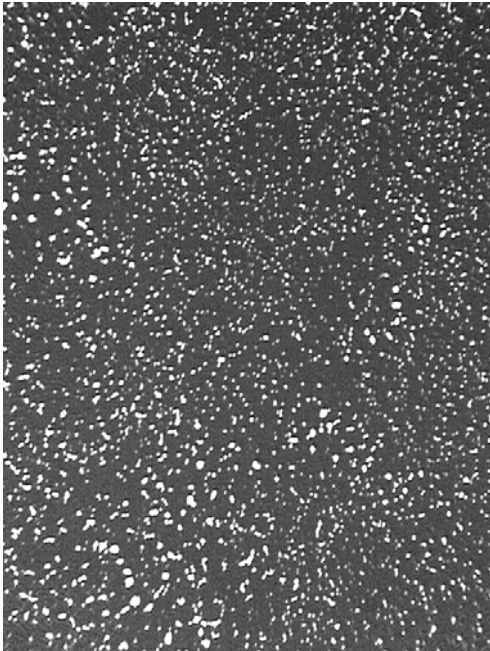
Magnification factor: 10x
Backlighting: front



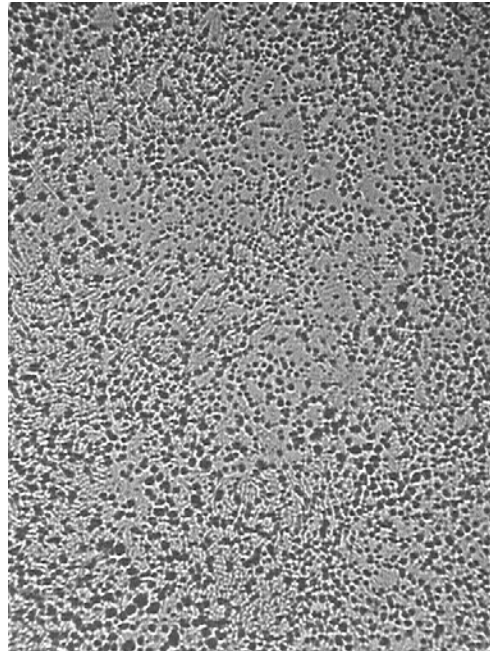
Magnification factor: 20x
Backlighting: front + back



Magnification factor: 20x
Backlighting: front

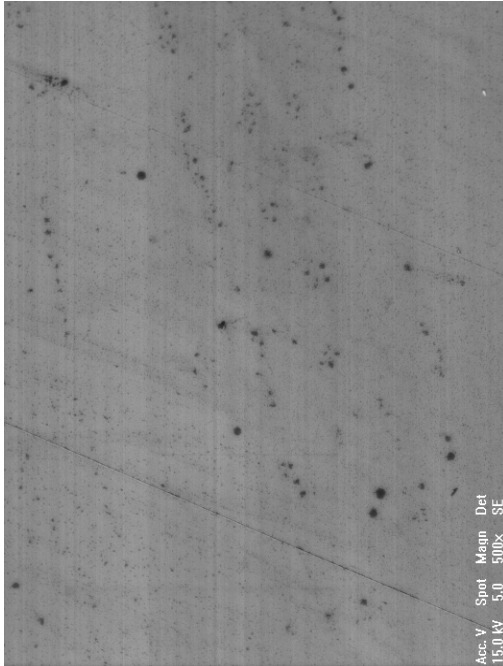


Magnification factor: 50x
Backlighting: back

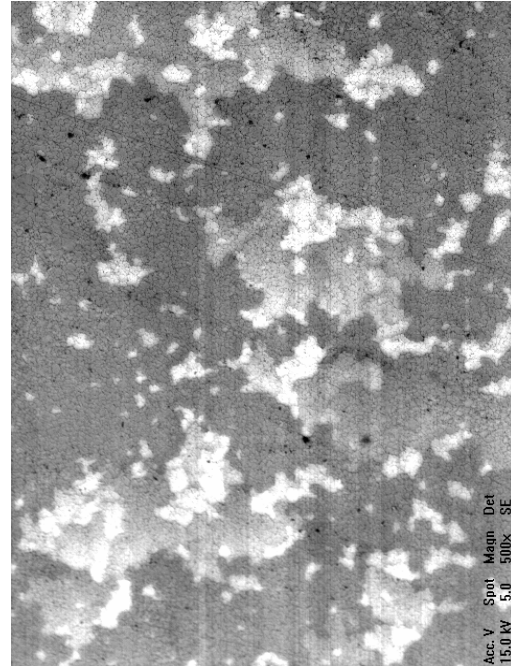


Magnification factor: 50x
Backlighting: front

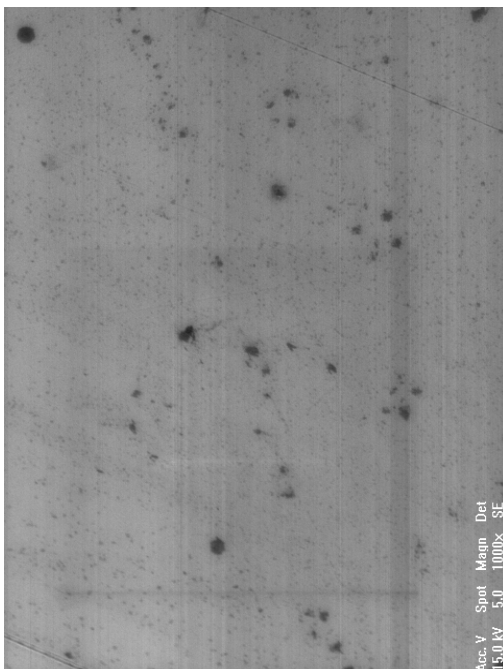
2. Images of non-damaged (on the left) and damaged (on the right) reflective areas acquired with electron microscope with different magnifications using secondary electrons detector.



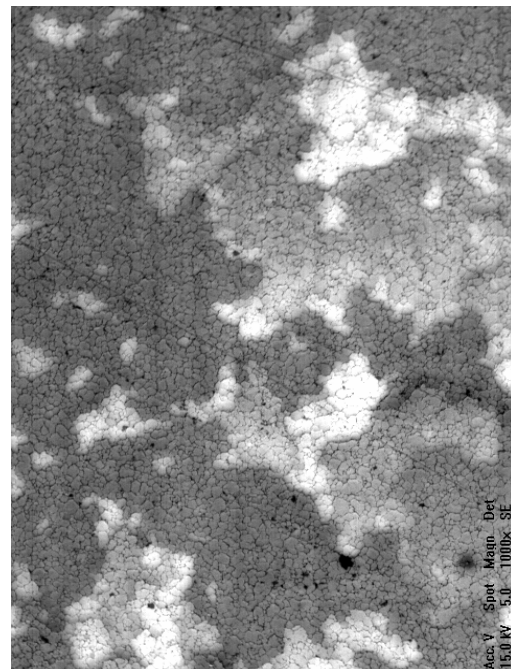
Magnification factor: 500x ;



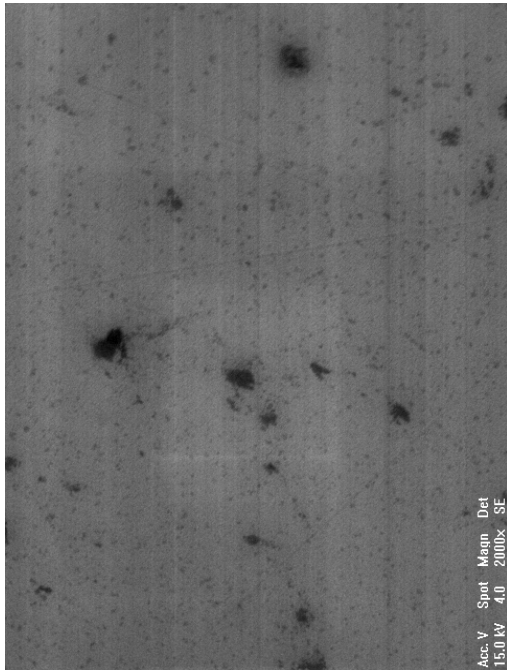
Electron beam spot size: 5.0



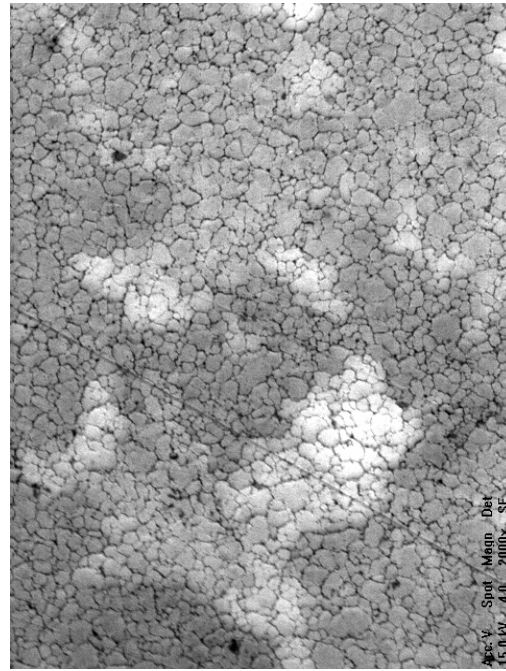
Magnification factor: 1000x ;



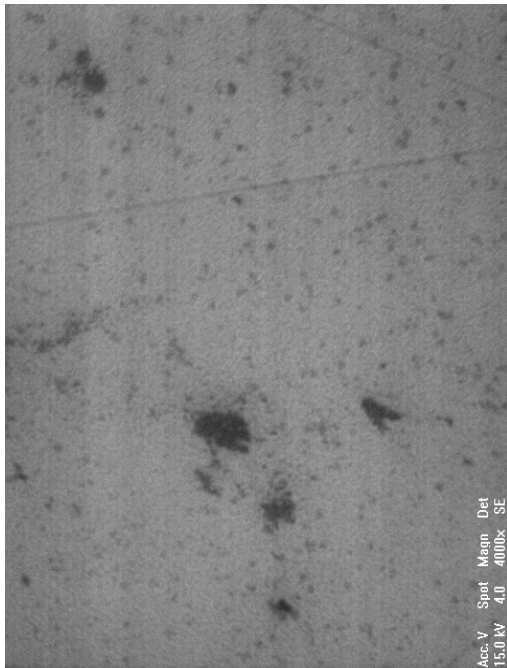
Electron beam spot size: 5.0



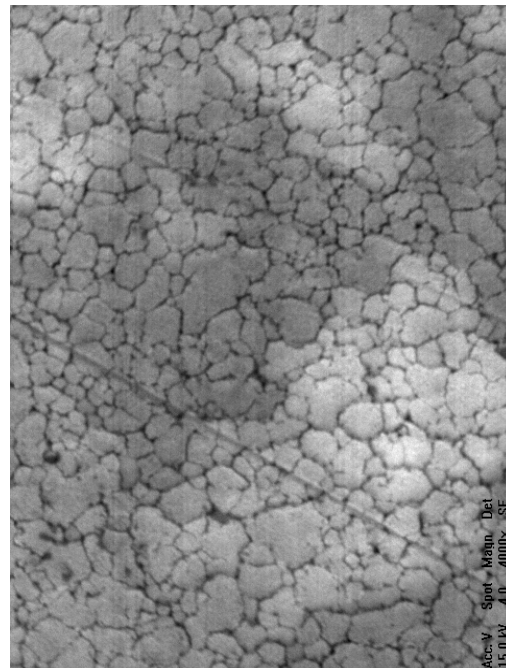
Magnification factor: 2000x ;



Electron beam spot size: 4.0



Magnification factor: 4000x ;



Electron beam spot size: 4.0

Bibliography

- [Abo03] – Y. Abou-Ali, G.J. Tallents, M. Edwards, R.E. King, et al.: *Measurement of the duration of X-ray lasing pumped by an optical laser pulse of picosecond duration*, Optics Communications, Vol.215, p.397, (2003).
- [Ado05] – A. Adonin et al., *Measurements of heavy ion beam profiles in gases*, GSI-2005-3 report June 2005.
- [Ado07a] – A. Adonin, J. Jacoby, V. Turtikov, A. Fertman, A. Golubev, D.H.H. Hoffmann, A. Ulrich, D. Varentsov and J. Wieser: *Laser effect on the 248nm KrF transition using heavy ion beam pumping*, Nucl. Instr. and Meth. A, Vol.577, p.357, (2007).
- [Ado07b] – A. Adonin, J. Jacoby, V. Turtikov, A. Fertman, A. Golubev, D.H.H. Hoffmann, A. Ulrich, D. Varentsov, and J. Wieser: *Pressure dependence of excimer emission induced by an intense uranium beam*, GSI Scientific Report 2006, p.283, (2007).
- [And77] – A.J. Andrews, A.J. Kearsley and C.E. Webb: Opt. Commun., Vol.20, p.265, (1977).
- [ATIM] – Manual for ATIMA, GSI website, (2007),
URL: <http://www-linux.gsi.de>
- [ARCo] – Catalogue of Action Research Corporation: *Excimer and UV Laser Optics*, 2005.
- [AXUV] – AXUV Photodiodes Operating Principles, IRD-Inc. website, (2007), URL: <http://www.ird-inc.com>
- [Ban03] – A. Bank, P. Forck: *Residual Gas Fluorescence for Profile Measurements at the GSI UNILAC*, Proceedings DIPAC 2003, Mainz, Germany.
- [Bar70] – J.N. Bardsley, M.A. Biondi: Adv. At. Mol. Phys., Vol.6, (1970).

- [Bar78] – J.N. Bardsley and J.M. Wadehra: *Calculations of ion-ion recombination rates at high pressures*, Appl. Phys. Lett., Vol.32, p.76, (1978).
- [Bas70] – N.G. Basov, V.A. Danilychev, Yu.M. Popov, and D.D. Khodkevich: *Laser operating in the vacuum region of the spectrum by excitation of liquid xenon with an electron beam*, JEPT Lett., Vol.12, p.329, (1970).
- [Bec96] – U. Bechthold, Ph.D. thesis: *Elektronenemission nach Stößen schneller Schwerionen mit komplexen Targets*, Johann Wolfgang Goethe-Universität, Frankfurt am Main, (1996).
- [Bec06] – F. Becker, C. Andre, P. Forck, D.H.H. Hoffmann, H. Iwase: *Profile Measurement by Beam Induced Fluorescence for 60 MeV/u to 750 MeV/u Heavy Ion Beams*, Proceedings of EPAC 2006, Edinburgh, Scotland.
- [Ber91a] – J. Bergoz: Handbook for Fast Current Transformer for Heavy Ion Fusion at GSI, Technical report, (1991).
- [Ber91b] – J. Bergoz: Handbook for Integrating Current Transformer for Heavy Ion Fusion at GSI, Technical report, (1991).
- [Bha76] – M.L. Bhaumik, R.S. Bradford, Jr. and E.R. Ault: *High-efficiency KrF excimer laser*, Appl. Phys. Lett., Vol.28, p.23, (1976).
- [Bio63] – M.A. Biondi: *Studies of the Mechanism of Electron-Ion Recombination*, Phys. Rev., Vol.129, p.1181, (1963).
- [Boh70] – D.K. Bohme, N.G. Adams, M. Muselman, D.B. Donkin and E.E. Ferguson: *Flowing afterglow studies of the reactions of the rare-gas molecular ions He, Ne, and Ar with molecules and rare-gas atoms*, J. Chem. Phys., Vol.52, p.5094, (1970).
- [Bon80] – T.D. Bonifield, F.H.K. Rambow, G.K. Walters, M.V. McCusker, D.C. Lorents and R.A. Gutcheck: *Production and decay of the 0_u^+ and 1_u states of Kr_2 excited by synchrotron radiation*, Chem. Phys. Lett., Vol.69, p.290, (1980).
- [Bra75] – C.A. Brau and J.J. Ewing: *Emission spectra of XeBr, XeCl, XeF, and KrF*, J. Chem. Phys., Vol.63, p.4640, (1975).

-
- [Bra81] – H.C. Brashears, Jr., D.W. Setser, and Y.-C. Yu: *Emission spectra of KrXeCl^{*}, KrXeBr^{*}, KrXeI^{*}, ArKrF^{*}, and ArKrCl^{*}*, J. Chem. Phys., Vol.74, p.10, (1981).
- [Bra84] – Ch. A. Brau: *Rare gas halogen excimers*, in “Excimer Lasers”, Ed. Ch. K. Rhodes, Topics in Applied Physics, Vol. 30, Springer-Verlag, Berlin, Heidelberg, New York, Tokyo (Second ed. 1984).
- [Bru70] – G. Bruk: *Cyclic charge particles accelerators*, Atomizdat, Moscow, 1970 (Russian edition).
- [Bur77] – R. Burnham and S.K. Searles: *Radiative lifetime of KrF^{*}*, J. Chem. Phys., Vol.67, p.5967, (1977).
- [Bus93] – B. Busch, A. Ulrich, W. Krötz, G. Ribitzki, J. Wieser, and M. Winkler: *Heavy ion beam pumped amplified spontaneous emission on the 172 nm xenon excimer transition*, J. Appl. Phys., Vol.74, p.5960, (1993).
- [Cal66] – J.G. Calvert and J.N. Pitts: *Photochemistry*, Wiley, New-York, (1966).
- [Can98] – L.R. Canfield, R.E. Vest, R. Korde, H. Schmidtke, and R. Desor, *Absolute silicon photodiodes for 160 nm to 254 nm photons*, Metrologia, Vol. 35, p. 329, 1998.
- [CASI] – User manual of CASINO, Scanning, Vol.29, Issue 3, p.92, (2007).
- [Che69] – Che Jen Chen: *Temperature Dependence of Dissociative Recombination and Molecular-Ion Formation in He, Ne, and Ar Plasmas*, Phys. Rev., Vol.177, p.245, (1969).
- [Che77] – H. Chen, R.E. Center, D.V. Trainor and W.I. Fyfe: *Dissociative attachment of electrons to F₂*, Appl. Phys. Lett., Vol.30, p.99, (1977).
- [Che79] – C.H. Chen and M.G. Payne: *Kinetics of proton-excited Ar-F₂ and Kr-F₂ mixtures*, J. Quant. Elect., Vol.15, p.149, (1979).
- [CVIL] – Catalogue of CVI Laser: *Laser optics and coating*, p.162, (2005).
- [Der05] – K. Dermati, private communication (2005).

-
- [Dob06] – D. Dobrev, private communication (2006).
- [Dol05] – A. Dolinskii, private communication (2005).
- [Dun76] – T.H. Dunning, Jr. and P.J. Hay: *Electronic states of KrF*, Appl. Phys. Lett., Vol.28, p.649, (1976).
- [Dun78] – T.H. Dunning, Jr. and P.J. Hay: *The covalent and ionic states of the rare gas monofluorides*, J. Chem. Phys., Vol.69, p.134, (1978).
- [Ede78] – J.G. Eden, R.W. Waynant, S.K. Searles, and R. Burnham: *New quenching rates applicable to the KrF laser*, Appl. Phys. Lett., Vol.32, p.733, (1978).
- [Egg75] – E. Eggarter: *Comprehensive optical and collision data for radiation action. II. Ar^{*}*, J. Chem. Phys., Vol.62, p.833, (1975).
- [Eck88] – D.J. Eckstrom, H.H. Nakano, C.C. Lorents, et al.: *Characteristics of electron-beam-excited Xe₂^{*} at low pressures as a vacuum ultraviolet source*, J. Appl. Phys., Vol.64, p.1679, (1988).
- [Ewi75] – J.J. Ewing, C.A. Brau: *Emission spectrum of XeI in electron-beam excited Xe/I₂ mixtures*, Phys. Rev. A, Vol.12, p.129, (1975).
- [Fed04] – A. Fedenev, A. Morozov, R. Krücken, S. Schoop, J. Wieser and A. Ulrich: *Applications of a broadband electron-beam pumped XUV radiation source*, J. Phys. D, Vol.37, p.1586, (2004).
- [Fri63] – S.E. Frish: *Atomic Optical Spectra*, Izdat., 1963 (Russian edition).
- [For04] – P. Forck, A. Peters: *Methods of Beam Profile Measurements at High Current Hadron Accelerators*, proceedings to ICFA-HB 2004, Bensheim.
- [For05] – P. Forck, A. Bank, T. Giacomini, A. Peters: *Beam Profile Monitors Based on Residual Gas Interaction*, DIPAC 2005, Lyon.
- [For06a] – P. Forck, *Lecture notes to Beam Instrumentation and Diagnostics*, Joint University Accelerator School, 2006.

-
- [For06b] – P. Forck, private communication (2006).
- [Fuj75] – T. Fujimoto, S. Kato: *Rarefied gas flow through a pipe orifice*, JSME, Vol.18, p.826, Bulletin, Aug. 1975.
- [Jac75] – J.D. Jackson: *Classical Electrodynamics*, John Wiley, 2 edition, (1975).
- [Jac76a] – J.H. Jacob and J.A. Mangano: *Modeling the KrF laser discharge*, Appl. Phys. Lett., Vol.28, p.724, (1976).
- [Jac76b] – J.H. Jacob and J.A. Mangano: *Total electron impact excitation cross sections of Ar and Kr*, Appl. Phys. Lett., Vol.29, p.467, (1976).
- [Jac78] – J.H. Jacob, M. Rokni, J.A. Mangano and R. Brochu: *Formation and quenching processes in e-beam-pumped Kr/F₂ mixtures*, Appl. Phys. Lett., Vol.32, p.109, (1978).
- [Jac90] – J. Jacoby, D.H.H. Hoffmann, R.W. Müller, K. Mahrt-Olt, R.C. Arnold, V. Schneider, and J. Maruhn: *Hydrodynamic motion of a heavy-ion-beam-heated plasma*, Phys. Rev. Lett., Vol.65, p.2007, (1990).
- [Jac95] – J. Jacoby, D.H.H. Hoffmann, W. Laux, R.W. Müller et al.: *Stopping of Heavy Ions in a Hydrogen Plasma*, Phys. Rev. Lett., Vol.74, p. 1550, (1995).
- [Jam92] – A.M. James and M.P. Lord: *Macmillan's chemical and physical data*, Macmillan, London, (1992).
- [Joh80] – T.H. Johnson and A.M. Hunter: *Physics of the krypton fluoride laser*, J. Appl. Phys., Vol.51, p.2406, (1980).
- [Har76] – G.A. Hart and S.K. Searles: *Kinetic model of the XeBr rare-gas monohalide excimer laser*, J. Appl. Phys., Vol.47, p.2033, (1976).
- [Haw77] – A.M. Hawryluk, J.A. Mangano and J.H. Jacob: *Gain and absorption measurements in a KrF* laser*, Appl. Phys. Lett., Vol.31, p.164, (1977).

-
- [Hay77] – P.J. Hay and T.H. Dunning, Jr.: *The electronic states of KrF*, J. Chem. Phys., Vol.66, p.1306, (1977).
- [Hof73] – P.W. Hoff, J.C. Swingle and Ch.K. Rhodes: *Observations of stimulated emission from high-pressure krypton and argon/xenon mixtures*, Appl. Phys. Lett., Vol.23, p.245, (1973).
- [Hof05] – D.H.H. Hoffmann, A. Blazevic, O. Rosmej, M. Roth, et al.: *Present and future perspectives for high energy density physics with intense heavy ion and laser beams*, Laser and Particle Beams, Vol. 23, p. 47, (2005).
- [Hou60] – F.G. Houtermans: Helv. Phys. Acta., Vol.33, p.933, (1960).
- [Hug74] – W.M. Hughes, J. Shannon and R. Hunter: *126,1-nm molecular argon laser*, Appl. Phys. Lett., Vol.24, p.488, (1974).
- [Hut80] – M.H.R. Hutchinson: *Excimers and excimer lasers*, Appl. Phys., Vol.21, p.95, (1980).
- [Ish77] – V.N. Ishchenko, V.N. Lisitsyn and A.M. Razhev: *Superradiative rare gas halide lasers excited by electric discharge*, Appl. Phys., Vol.12, p.55, (1977).
- [Gol75] – M.F. Golde: *Interpretation of the oscillatory spectra of the inert-gas halides*, J. Mol. Spectrosc., Vol.58, p.261, (1975).
- [Good] – Material Properties, GoodFellow website, (2007),
URL: <http://www.goodfellow.com>
- [Gro80] – K-O. Groeneveld, E. Schopper and S. Schumann: *Solid state nuclear track detectors*, edited by H. Francois et al., Oxford and New York, (1980).
- [Gul96] – E.M. Gullikson, R. Korde, L.R. Canfield and R.E. Vest, *Stable silicon photodiodes for absolute intensity measurements in the VUV and soft x-ray regions*, J. of Elec. Spect. and Rel. Phen., Vol.80, p.313, (1996).
- [Kar97] – A.V. Karelin, A.A. Sinyanskii and S.I. Yakovlenko: *Nuclear-pumped lasers and physical problems in constructing a reactor-laser*, Quantum Electronics, Vol.27, p.375, (1997).

-
- [Kel88] – R. Keller: *Multicharged ion production with MUCIS*, GSI Scientific Report 1987, (1988).
- [Ket74] – J.W. Keto, R.E. Gleason, Jr., and G.K. Walters: *Production Mechanisms and Radiative Lifetimes of Argon and Xenon Molecules Emitting in the Ultraviolet*, Phys. Rev. Lett., Vol.33, p.1365, (1974).
- [Kli02] – A. Klisnick, J. Kuba, D. Ros, R. Smith, et al.: *Demonstration of a 2-ps transient x-ray laser*, Phys. Rev. A, Vol.65, (2002).
- [Koc95] – I.V. Kochetov and D. Lo: *Kinetics of a self-sustained discharge-pumped Xe₂^{*} laser at 172 nm*, Opt. Commun., Vol.113, p.541, (1995).
- [Koe75] – H.A. Koehler, L.J. Ferderber, D.L. Redhead, and P.J. Ebert: *Vacuum-ultraviolet emission from high-pressure krypton*, Phys. Rev. A, Vol.12, p.968, (1975).
- [Kra07] – M. Krämer, private communication, (2007).
- [Kro89] – W. Krötz, A. Ulrich, B. Busch, G. Ribitzki and J. Wieser: *Emission of vacuum ultraviolet radiation from neon excimers excited by a heavy ion beam*, Appl. Phys. Lett., Vol.55, p.2265, (1989).
- [Lac78] – W.B. Lacina and D.B. Cohn: *Theoretical analysis of the electrically excited KrF laser*, Appl. Phys. Lett., Vol.32, p.106, (1978).
- [Lac06] – G. Laczkó, Ph.D. thesis: *Investigation of the Radial Ionization Distribution of Heavy Ions with an Optical Particle Track Chamber and Monte-Carlo Simulations*, Johann Wolfgang Goethe-Universität, Frankfurt am Main (2006).
- [LLas] – *Fluid Flow Through Small Calibrated Orifices*, Lenox Laser website, (2007), URL: <http://www.lenoxlaser.com>
- [Len66] – B.A. Lengyel: *Introduction to Laser Physics*, Wiley and Sons, New York, (1966).

- [Lin96] – J. Lindhard and A.H. Sørensen: *Relativistic theory of stopping for heavy ions*, Phys. Rev. A, Vol.53, p.2443, (1996).
- [Man71] – A. Mandl: *Electron Photodetachment Cross Section of the Negative Ion of Fluorine*, Phys. Rev. A, Vol.3, p.251, (1971).
- [Man77] – J. Mangano, J. Jacob, M. Rokni, A. Hawryluk: *Three-body quenching of KrF* by Ar and broad-band emission at 415 nm*, Appl. Phys. Lett., Vol.31, p.26, (1977).
- [Mat85] – D.L. Matthews, P.L. Hagelstein, M.D. Rosen, M.J. Eckart, et al.: *Demonstration of a Soft X-Ray Amplifier*, Phys. Rev. Lett., Vol.54, p.110, (1985).
- [Max93] – S. Maxon, K.G. Estabrook, M.K. Prasad, A.L. Osterheld, R.A. London, and D.C. Eder: *High gain x-ray lasers at the water window*, Phys. Rev. Lett., Vol.70, p.2285, (1993).
- [McD70] – E.W. McDaniel, V. Ermak, A. Dalgarno, E.E. Ferguson and L. Friedman: *Ion molecule reaction*, Wiley-Interscience, New-York, (1970).
- [Mic78] – H.H. Michels, R.H. Hobbs and L.A. Wright: *Electronic structure of excimer molecular lasers*, Int. J. Quant. Chem., Vol.13, p.169, (1978).
- [Mor81] – W.L. Morgan and A. Szöke: *Kinetic processes in Ar-Kr-F₂ laser mixtures*, Phys. Rev. A, Vol.23, p.1256, (1981).
- [Nak76] – H. Nakano, R. Hill, D. Lorents, D. Huestis, et al.: *New electronic transition laser systems*, Tech. Report MP, p.76, Stanford Res. Inst., (1976).
- [Nee96] – S. Neeser, M. Schumann and H. Langhoff: *Improved gain for the Ar₂* excimer laser at 126 nm*, Appl. Phys. B: Laser and Optics, Vol.63, p.103, (1996).
- [Neu04] – P. Neumayer, W. Seelig, K. Cassou, A. Klisnick, et al.: *Transient collisionally excited X-ray laser in nickel-like zirconium pumped with the PHELIX laser facility*, Appl. Phys. B, Vol.78, p.957, (2004).

-
- [NIST] – *Atomic Spectra Database*, National Institute of Standards and Technology website, (2007),
URL: <http://physics.nist.gov/>
- [Ocea] – Ocean Optics Inc. website, (2007),
URL: <http://oceanoptics.com>
- [Oga01] – M. Ogawa, et al.: *Stopping Power of Heavy Ions in Hot Dense Plasmas*, Acta Phys. Pol. B, Vol.32, p.945, (2001).
- [Pet72] – L.R. Peterson and J.E. Allen, Jr.: *Electron Impact Cross Sections for Argon*, J. Chem. Phys., Vol.56, p.6068, (1972).
- [Pet87] – P.J.M. Peters, H.M.J. Bastiaens, W.J. Witteman and T. Gerber: *A study of the electron quenching of excimers in a KrF* laser excited by a coaxial electron beam*, Appl. Phys. B, Vol.43, p.253, (1987).
- [Pet04] – A. Peters, P. Forck: *Non-Interfering Beam Diagnostic Developments*, Proceedings of LINAC 2004, Lübeck, Germany.
- [PHEL] – PHELIX proposal, GSI Report, GSI-98-10, (1998).
- [Pip73] – L.G. Piper, J.E. Velazco and D.W. Setser: *Quenching cross sections for electronic energy transfer reactions between metastable argon atoms and noble gases and small molecules*, J. Chem. Phys., Vol.59, p.3323, (1973).
- [Plu02] – M.A. Plum, E. Bravin, J. Bossert, R. Maccaferri: *N₂ and Xe gas scintillation cross-section, spectrum, and lifetime measurements from 50 MeV to 25 GeV at the CERN PS and Booster*, Nuc. Inst. Meth., A 492, p.74, (2002).
- [Qui78a] – G.P. Quigley and W.M. Hughes: *Lifetime and quenching rate constants for Kr₂F* and Kr₂**, Appl. Phys. Lett., Vol.32, p.649, (1978).
- [Qui78b] – G.P. Quigley and W.M. Hughes: *The radiative lifetime and quenching of KrF*, Appl. Phys. Lett., Vol.32, p.627, (1978).
- [Rad80] – A.A. Radzig, B.M. Smirnov: *Handbook on Atomic and Molecular Physics*, Atomizdat, 1980 (Russian edition).

-
- [Rap65] – D. Rapp and P. Englander-Golden: *Total Cross Sections for Ionization and Attachment in Gases by Electron Impact. I. Positive Ionization*, J. Chem. Phys., Vol.43, p.1464, (1965).
- [Ree01] – N. Reeg and N. Schneider: *Current transformers for GSI's keV/u to GeV/u ion beams*, DIPAC Proceedings ESRF, Grenoble (2001).
- [Ree06] – N. Reeg, private communication (2006).
- [Rho74] – Ch.K. Rhodes: *Review of ultraviolet laser physics*, IEEE J. Quantum Electron., Vol.10, p.153, (1974).
- [Rok77] – M. Rokni, J.H. Jacob, and J.A. Mangano: *Dominant formation and quenching processes in E-beam pumped ArF and KrF lasers*, Phys. Rev. A, Vol.16, p.2216, (1977).
- [Rok78] – M. Rokni, J.A. Mangano, J.H. Jacob and J.C. Hsia: IEEE J. Quant. Electron., Vol.14, p.464, (1978).
- [Ros85] – M.D. Rosen, P.L. Hagelstein, D.L. Matthews, E.M. Campbell, et al.: *Exploding-Foil Technique for Achieving a Soft X-Ray Laser*, Phys. Rev. Lett., Vol.54, p.106, (1985).
- [Rut11] – E. Rutherford: Philos. Mag., Vol.21, p.669, (1911).
- [Sak87] – T. Sakurai, N. Goto and C.E. Webb: *Kr₂^{*} excimer emission from multi-atmosphere discharges in Kr, Kr-He and Kr-Ne mixtures*, J. Phys. D: Appl. Phys., Vol.20, p.709, (1987).
- [Sal98] – M. Salvermoser, A. Ulrich, and J. Wieser: *Heavy-ion-beam-induced laser scheme in hydrogenlike He⁺*, Phys. Rev. E, Vol.58, p.6531, (1998).
- [Sas01] – W. Sasaki, T. Shirai, S. Kubodera, J. Kawanaka, and T. Igarashi: *Observation of vacuum-ultraviolet Kr₂^{*} laser oscillation pumped by a compact discharge device*, Optics Lett., Vol.26, p.503, (2001).
- [Sch96] – A. Schamass, N. Schneider and R. Steiner: *A Beam Intensity Monitor for Synchrotron Beams with Fast Beam Extraction Mode*, Technical report, GSI Darmstadt, (1996).

-
- [Sch97] – C. Scheidenberger and H. Geissel: *Penetration of Relativistic Heavy Ions Through Matter*, Preprint GSI-97-34, GSI-Darmstadt, (1997).
- [Sch98] – C. Scheidenberger, Th. Stöhlker, W.E. Meyerhof, H. Geissel, P.H. Mokler and B. Blank: *Charge states of relativistic heavy ions in matter*, Nucl. Instr. and Meth. B, Vol.142, p.441, (1998).
- [Scot] – Airflow through an Orifice, Scott Specialty Gases Inc. website, (2007), URL: <http://www.scottsemicon.com>
- [See64] – D.J. Seery and D. Britton: *The Continuous Absorption Spectra of Chlorine, Bromine, Bromine Chloride, Iodine Chloride, and Iodine Bromide*, J. Phys. Chem., Vol.68, p.2263, (1964).
- [See89] – J.F. Seely: *Transmission filter for the “water-window” wavelength region 23–44 Å*, Optics Communications, Vol.70, p.207, (1989).
- [Sha69] – M. Shaper and H. Scheibner: Beitr. Plasmaphys., Vol.9, p.45, (1969).
- [Shu77] – V.H. Shui: *Calculation of recombination rate constants for $KrF^{*+}R+R \rightarrow RKrF^{*+}R$ ($R=Ar, Kr$)*, Appl. Phys. Lett., Vol.31, p.50, (1977).
- [Sie86] – A.E. Siegman: *Lasers*, University Science Books, Sausalito, California, (1986).
- [Sig98] – P. Sigmund: *Stopping power in perspective*, Nucl. Instr. and Meth. B, Vol.135, p.1, (1998).
- [Sig02] – P. Sigmund and A. Schinner: *Binary theory of electronic stopping*, Nucl. Instr. and Meth. B, (2002).
- [Smi83] – B.M. Smirnov: *Excimer molecules*, Sov. Phys. Uspekhi, Vol.26, p.31, (1983).
- [Spä98] – P. Spädtke, J. Bossler, H. Emig, K.D. Leible, C. Mühle, H. Reich, H. Schulte, and K. Tinschert: *Ion source development at GSI*, Rev. Sci. Inst., Vol.69, p.1079, (1998).

- [Spi97] – Ch. Spielmann, N.H. Burnett, S. Sartania, R. Koppitsch, et al.: *Generation of Coherent X-rays in the Water Window Using 5 fs Laser Pulses*, Science, Vol.278, p.661, (1997).
- [Spi05] – P. Spiller, private communication (2005).
- [Spi06] – P. Spiller, K. Blasche, U. Blell, P. Forck, et al.: *SIS18 Status Report*, GSI Report 2006-1, August 2006.
- [Ste56] – R.K. Steunenbergh and R.C. Vogel: *The Absorption Spectrum of Fluorine*, J. Am. Chem. Soc., Vol.78, p.901, (1956).
- [Ste93] – M. Steck, K. Beckert, H. Eickhoff, B. Franzke, F. Nolden and P. Spadtke: *Electron cooling of heavy ions at GSI*, Proceedings of PAC 93, Washington, (1993).
- [Ste05] – M. Steck, private communication (2005).
- [Tah05a] – N.A. Tahir, A. Adonin, et al., D.H.H. Hoffmann, S. Udrea, D. Varentsov: *Studies of heavy ion induced high-energy-density states in matter at the GSI Darmstadt SIS-18 and future FAIR facility*, Nucl. Instr. Meth. A, Vol.544, p.16, (2005).
- [Tah05b] – N.A. Tahir, C. Deutsch, V.E. Fortov, V. Gryaznov, D.H.H. Hoffmann, et al.: *Proposal for the Study of Thermophysical Properties of High-Energy-Density Matter Using Current and Future Heavy-Ion Accelerator Facilities at GSI Darmstadt*, Phys. Rev. Lett., Vol.95, 035001, (2005).
- [Tel76] – J. Tellinghuisen, A.K. Hays, J.M. Hoffman and G.C. Tisone: *Spectroscopic studies of diatomic noble gas halides. II. Analysis of bound-free emission from XeBr, XeI, and KrF*, J. Chem. Phys., Vol.65, p.4473, (1976).
- [Tie90] – J.J. Tiee, C.R. Quick, A.H. Hsu and D.E. Hof: *Time-resolved fluorescence measurements of KrF emission produced by vacuum ultraviolet photolysis of KrF₂ and Kr/F₂ mixtures*, Physica Scripta., Vol.41, p.71, (1990).
- [Tor76] – E. Torchinskiy: *Crystallization and thermotreatment of thin foils*, Nauka i Tehnika, p.312, Minsk, 1976 (Russian edition).

-
- [Tra80] – D.W. Trainor and J.H. Jacob: *Electron quenching of KrF* and ArF**, Appl. Phys. Lett., Vol.37, p.675, (1980).
- [Ulr83] – A. Ulrich, H. Bohn, P. Kienle, and G.J. Perlow: *Heavy ion beam pumped He-Ar laser*, Appl. Phys. Lett., Vol.42, p.782, (1983).
- [Ulr87] – A. Ulrich, H.J. Körner, W. Krötz, et al.: *Heavy-ion excitation of rare-gas excimers*, J. Appl. Phys., Vol.62, p.357, (1987).
- [Ulr91] – A. Ulrich, J. Wieser, R. Pfaffenberger, B. Busch, et al.: *Optical gain on the 476.5 nm Argon-ion laser line in a gas-target excited by a heavy ion beam*, Z. Phys. A, Vol.341, p.111, (1991).
- [Ulr94a] – A. Ulrich, R. Gernhäuser, W. Krötz, J. Wieser, and D.E. Murnick: *Ion-atom charge-transfer system for a heavy-ion-beam pumped Laser*, Phys. Rev. A, Vol.50, p.1931, (1994).
- [Ulr94b] – A. Ulrich, J. Wieser, A. Brunnhuber, W. Krötz: *Heavy ion beam pumped visible laser*, Appl. Phys. Lett., Vol.64, p.1902, (1994).
- [Ulr06a] – A. Ulrich, A. Adonin, J. Jacoby, V. Turtikov, et al.: *Excimer Laser Pumped by an Intense, High-Energy Heavy-Ion Beam*, Phys. Rev. Lett., Vol.97, 153901, (2006).
- [Ulr06b] – A. Ulrich, V. Turtikov, A. Adonin, D.H.H. Hoffmann, J. Jacoby et al.: *Heavy-Ion-Beam Pumped Excimerlaser*, GSI Scientific Report 2005, p.329, (2006).
- [Var02] – D. Varentsov, Ph.D. thesis: *Energy loss dynamics of intense heavy ion beams interacting with matter*, Technische Universität Darmstadt (2002)
- [Var03] – D. Varentsov, P. Spiller, and S. Udrea: *Influence of focal length and beam rigidity on final focusing at HHT*, GSI Scientific Report 2003.
- [Var04] – D. Varentsov et al., GSI-2004-3 report July 2004.
- [Var05] – D. Varentsov, private communication (2005).
- [Vel75] – J.E. Velazco, D.W. Setser: *Bound-free emission spectra of diatomic xenon halides*, J. Chem. Phys., Vol.62, p.1990, (1975).

-
- [Vel76] – J.E. Velazco, J.H. Kolts and D.W. Setser: *Quenching rate constants for metastable argon, krypton, and xenon atoms by fluorine containing molecules and branching ratios for XeF* and KrF* formation*, J. Chem. Phys., Vol.65, p.3468, (1976).
- [Vri65] – L. Vriens: *A semi-empirical formula for calculation of absolute cross sections for ionization and excitation of atoms by electrons*, Physica, Vol.31, p.395, (1965).
- [Wea02] – B.A. Weaver and A.J. Westphal: *Energy loss of relativistic heavy ions in matter*, Nucl. Instr. and Meth. B, Vol.187, p.285, (2002).
- [Wei00] – H. Weick, H. Geissel, C. Scheidenberger, et al.: *Slowing down of relativistic few-electron heavy ions*, Nucl. Instr. and Meth. B, Vol.164, p.168, (2000).
- [Wie93] – H. Wiedemann: *Particle Accelerator Physics: basic principles and linear beam dynamics*, Springer Verlag, Berlin, 1993.
- [Wie01] – J. Wieser et al.: *Optical Beam Diagnostics*, GSI-2001-4 report October 2001
- [Wil96] – D. Williams and B. Carter: *“Transmission electron microscopy”* A textbook for material science, Plenum Press, New York and London, 1996.
- [WinA] – Description of the WinAGILE code, CERN website, (2007),
URL: <http://bryant.home.cern.ch/bryant/>
- [You81] – R.J. De Young: *Kilowatt multiple-path ³He-Ar nuclear-pumped laser*, Appl. Phys. Lett., Vol.38, p.297, (1981).
- [Zie03] – J.F. Ziegler, J.P. Biersack and U. Littmark: full description of the SRIM2003 code in the tutorial book *“The Stopping and Range of Ions in Solids”*, Pergamon Press, New York, 2003.
- [Zhu00] – E.E. Zhurkin and S.D. Bogdanov: *Investigation of the effect of high order Z₁ terms in electronic stopping powers on the ranges of heavy ions with energies of about 1 GeV/amu*, Nucl. Instr. and Meth. B, Vol.164, p.230, (2000).

Zusammenfassung

Laser und deren spezifische physikalische Eigenschaften haben sich sowohl auf vielen Gebieten der Grundlagenforschung als auch in weiten Bereichen des alltäglichen Lebens etabliert. Die Anwendungsgebiete liegen zwischen dem Infraroten- bis hin zum hochenergetischen Röntgenspektralbereich. Dabei besteht derzeit ein großes Interesse neuartige Anwendungsgebiete von Lasern im UV-Wellenlängenbereich zu erschließen. Für die Erzeugung der nötigen Besetzungsinversion bei UV-Lasern werden hohe Puleistungen benötigt. Das Hauptziel dieser Arbeit ist die Untersuchung von Schwerionenstrahlen als Pumpquelle in Gasen zur Erzeugung von Laserstrahlung im UV-Bereich.

Die grundlegende Idee der Anwendung von Schwerionen zur Erzeugung von Laserstrahlung liegt in den spezifischen Eigenschaften der Wechselwirkung von Ionen mit Materie. Der Energieverlust der Schwerionen in Materie skaliert quadratisch mit dem Ladungszustand des Ionenstrahls und ermöglicht somit eine hohe Energiedichte im Targetgas. Eine weitere Eigenschaft der Wechselwirkung von Schwerionenstrahlen mit Gasen ist der nicht-thermische Anregungsmechanismus von Atomen und Molekülen im Target. Des weiteren haben schwere Teilchen kleine Streuwinkel, die in Kombination mit der Ionenstrahlfokussierung und dem räumlichen Verlauf der Energiedeposition im Gas ein annähernd zylindrisches, gleichmäßig angeregtes Volumen auf der Strahlachse ergeben. Dieses kann optimal an das Modenvolumen eines Laserresonators angepasst werden.

Erstmals wurde ein schwerionenstrahlgepumpter Gaslaser am "van-de-Graaff"-Beschleuniger in München im Jahre 1983 realisiert. Mit 100 MeV ^{32}S Ionen gelang es, einen He-Ar Laser im infraroten Wellenlängenbereich zu betreiben. Weitere Entwicklungen auf diesem Gebiet wurden durchgeführt, stießen jedoch durch die begrenzte Pumpleistung des Ionenstrahls an ihre Grenzen. Deshalb war die Wellenlänge der emittierten Laserstrahlung auf den infraroten und sichtbaren Bereich beschränkt. Neue Perspektiven ergaben sich am Beschleuniger der GSI (Gesellschaft für Schwerionenforschung, Darmstadt, Deutschland), an dem beträchtlich höhere Strahlströme bei

gleichzeitig besserer Strahlqualität bereitgestellt werden konnten. In dieser Arbeit wird nun erstmalig über einen mit einem Schwerionenstrahl gepumpten UV-Laser berichtet. Das Experiment wurde mit einem vom SIS-18 bereitgestellten intensiven, hochenergetischen Uranionenstrahl an der GSI durchgeführt.

Das Schwerionensynchrotron SIS-18 an der GSI kann Schwerionen bis hin zu Uran mit Energien bis zu 2 GeV (1 GeV für U-Ionen) pro Nukleon für Experimente liefern. Durch eine zusätzliche Elektronenkühlung des Strahls, können an der vorhandenen Anlage Strahlintensitäten bis hin zu $5 \cdot 10^9$ Teilchen pro Schuß für die schweren Uranionen und Intensitäten von mehr als 10^{11} für leichtere Teilchen wie z.B. Stickstoff, Kohlenstoff usw. erreicht werden. Zusätzlich wird mit der Elektronenstrahlkühlung eine signifikante Reduzierung der Strahlemittanz erreicht, wodurch eine bessere Fokussierung und Kollimierung des Strahls für das Experiment möglich ist. Mit einer speziellen Kompression des Strahls können gepulste Ionenstrahlen mit Zeiten kürzer als 100 ns (Halbwertsbreite) erzeugt werden.

Für die in dieser Arbeit beschriebenen Experimente wurde ein KrF* Excimer-Laser verwendet, dessen Laseremissionswellenlänge bei 248 nm liegt. Die Wahl dieses Excimers hatte den Grund, dass sich Strahlung dieser Wellenlänge ohne merkliche Abschwächung in Luft ausbreitet, wodurch keine zusätzlichen Vakuumvorrichtungen und spezielle UV-Detektoren notwendig waren.

Der experimentelle Aufbau des Lasers selbst besteht aus einer Edelstahlröhre als Laserrohr mit einer Länge von 1,2 m bei einem Durchmesser von 38 mm. Diese befindet sich ungefähr 2 m hinter dem Fokussiersystem des Ionenstrahls. An der Röhre befinden sich Anschlüsse zum Vakuumsystem und zur Gasbefüllungsanlage für das Targetgas. An den Stirnseiten befinden sich jeweils Justiermotoren für die dort befindlichen Laserspiegel. Zusätzlich wurden noch verschiedene Strahldiagnostiken am Laser angebracht. Das Vakuumsystem besteht aus einer ölfreien Vorpumpe und einer Turbomolekularpumpe für das Feinvakuum. Für die Desorption und somit für die Verbesserung des Vakuums wurde der Rezipient mit Hilfe von Heizdrähten auf eine Temperatur von 130°C erhitzt. Zusätzlich konnte mit den gewickelten Heizdrähten eine Abschirmung der HF-Strahlung für die experimentellen Untersuchungen erreicht werden.

Die Hochdruckgasversorgung für das Gastarget wurde an zwei verschiedenen Punkten mittels Teflonschläuchen mit einem Durchmesser von

6 mm mit dem Rezipienten verbunden. Teflon wurde als Material verwendet, da es resistent gegen korrosive Gase ist und zugleich hohe Drücke bis zu 10 bar standhält. Um das Mischungsverhältnis des Excimergases konstant zu halten und eine Erschöpfung des Fluors durch Verunreinigungen zu vermeiden, wurde ein konstanter Gasfluss gewährleistet. Die Lage der Gasanschlüsse am Rezipienten wurde dabei so gewählt, dass das gesamte Gasvolumen ständig umgewälzt wurde. Das Lasergas bestand aus 95,5% Kr versetzt mit 0,5% F₂. Durch eine zusätzliche Gaszuführung konnte Argon (Ar 4.8) als Puffergas beigemischt werden. Die Steuerung des Gasdurchflusses durch den Rezipienten wurde durch die Kombination von verschiedenen Ventilen und Drucksensoren überwacht und wenn nötig reguliert.

Als optischer Resonator wurden ein auf die Wellenlänge von 248 nm hochreflektierender dielektrisch beschichteter Spiegel mit einem Durchmesser von 25 mm und Krümmungsradius vom 3 m sowie ein ebener, 25 mm Durchmesser, aluminium-beschichteter Spiegel verwendet. Positioniert wurde der Al-Spiegel am Eintrittsort des Ionenstrahls und in einem Abstand von 1,3 m der dielektrische Spiegel. Dieser Ausgangsspiegel diente auch als Vakuumabschluss und Auskoppelfenster für den Laserstrahl. Beide Spiegel wurden mit speziellen Justageeinheiten für die Optimierung des Strahlenganges innerhalb des Resonators versehen, die dem in der Gaszelle vorherrschenden hohen Druck (bis zu 10 bar) standhalten mussten. Mit der Justiereinheit konnten die Spiegel in Mikrometerschritten mittels computerunterstützter Steuerung von Elektromotoren verstellt werden.

Für die Messungen der zeitlichen Struktur und der Laserintensität entlang der Ionenstrahlachse sowie für die Untersuchung der Spontanemission senkrecht zur Strahlachse wurden zwei im UV-Wellenlängenbereich empfindliche Photodioden mit hoher Zeitauflösung verwendet. Um nur die für die KrF* Emissionslinie interessante Wellenlänge zu detektieren und alle andere Komponenten auszufiltern, wurden beide Photodioden mit einem Interferenz-Breitband-Filter versehen. Die Breite der transmittierten Strahlung der Filter war 40 nm (Halbwertsbreite), wobei die zentrale Wellenlänge bei 254 nm (Hg-Linie) lag. Die Photodioden wurden mit einer Grundspannung von -117 V versorgt, wodurch eine zeitliche Auflösung von unter 2 ns erreicht werden konnte.

Die spektral aufgelösten Untersuchungen wurden mittels zweier faseroptisch gekoppelter USB-Spektrometer durchgeführt. Der spektrale Messbereich lag zwischen 200 nm und 1100 nm bei einer Auflösung von

2,3 nm. Durch einen zusätzlichen elektronischen Filter konnte eine zeitliche Auflösung von bis zu 10 μ s erreicht werden.

Weiterhin wurden verschiedenste Diagnostikmethoden für den Ionenstrahl angewandt. Sowohl die gesamte als auch die zeitaufgelöste Intensität des Ionenstrahls wurden über eine Transformatorspule im Extraktionsbereich des SIS-18 induktiv erfasst. Der Fehler bei der Messung der Gesamtintensität betrug weniger als 2%. Bei der zeitaufgelösten Messung am Ende des Strahlrohrs konnte eine Genauigkeit < 5 ns erreicht werden. Weitere Messungen wurden bezüglich des orts aufgelösten Profils des Ionenstrahls an zwei verschiedenen Stellen durchgeführt. Am Eingang zur Gaszelle wurde der Strahl mit einem 600 μ m dicken Al_2O_3 -Szintillator gemessen. Der zweite Messpunkt befand sich innerhalb des Rezipienten im Bereich der größten Energiedeposition der Ionen. Diese optischen Messungen während der Positionierung und Fokussierung erfolgten mit Hilfe eines Al_2O_3 -Szintillators.

Um die genaue Position des Strahls am zweiten Meßpunkt zu erhalten, wurden zwei senkrecht zueinander angeordnete hochauflösende triggerbare CCD-Kameras verwendet. Mit beiden Kameras konnte das Leuchten des Lasergases während der Ionenstrahl-Gas-Wechselwirkung aufgenommen werden. Die Auswertung der Aufnahmen lieferte die nötigen Informationen über die Intensitätsverteilung der Ionen, Strahllage, Strahlgröße und die Position des Bragg-Peaks. Diese Größen, zusammen mit dem Gasdruck und dem Gas-Mischungsverhältnisses, liefern ein Wert für die anfängliche Ionenenergie am Eingang der Zelle.

Die Durchführung des Experiments fand im Dezember 2005 am HHT-Messplatz der Gesellschaft für Schwerionenforschung statt. Uranionen wurden gepulst im SIS-18 auf eine Energie von bis zu 250 MeV/u beschleunigt. Für quantitative Messungen werden einzelne Pulse verwendet, und während der Justage eine Repetitionsrate von 0,1 Hz. Die Intensität der Uranionen konnte während der Experimente von ca. 10^8 Teilchen pro Puls bis hin zu $2,5 \cdot 10^9$ Teilchen pro Puls mit einer Pulsdauer von 110 ns (Halbwertsbreite) gesteigert werden. Bevor der Strahl von der Strahlführung zum Gastarget gelangt, muss er eine Reihe von verschiedenen Sektionen durchqueren:

- den Ausgang der Strahlführung, einem Al-Fenster mit einer Dicke von 150 μ m.
- einen Luftspalt von 210 cm.
- einen Al_2O_3 Szintillator mit einer Dicke von 600 μ m.
- das Eingangsfenster zur Gaszelle aus Edelstahl mit einer Dicke von 50 μ m.

- einen 3,175 mm dicken, aus SiO_2 bestehenden, Resonatorspiegel.

So wird nur die restliche Ionenenergie von $71 \text{ MeV}/u$ im Lasergas deponiert. Die maximal im Gas deponierte Energie beträgt 6,7 J bei einer Strahlleistung von etwa 61 MW.

Bei diesen Experimenten betragen die Mischungsverhältnisse zwischen Excimer und Puffergas 35/65 und 60/40. Der Druck im Laserrohr konnte im Bereich zwischen 1,2 und 2 bar variiert werden.

Erste Anzeichen von Laseraktivität entlang der Strahlachse wurden mit einem Spektrometer beobachtet. Durch die Erhöhung der Strahlenergie bzw. der Pumpenergie über einen bestimmten Schwellenwert setzte die starke Laseremission bei einer Wellenlänge von $\lambda = 248 \text{ nm}$ ein. Abbildung 1 zeigt zwei Beispiele für auf der Strahlachse gemessene Emissionsspektren für Ionenstrahlintensitäten von $1,09 \cdot 10^9$ Ionen pro Puls (unterhalb der Laserschwelle) und $1,34 \cdot 10^9$ Ionen pro Puls (über der Laserschwelle).

Mit diesem Experiment wurde an der GSI erstmals ein schwerionengepumpter UV-Laser bei einem bekannten Übergang eines KrF^* Eximer Lasers bei $\lambda = 248 \text{ nm}$ realisiert. Die experimentell ermittelte

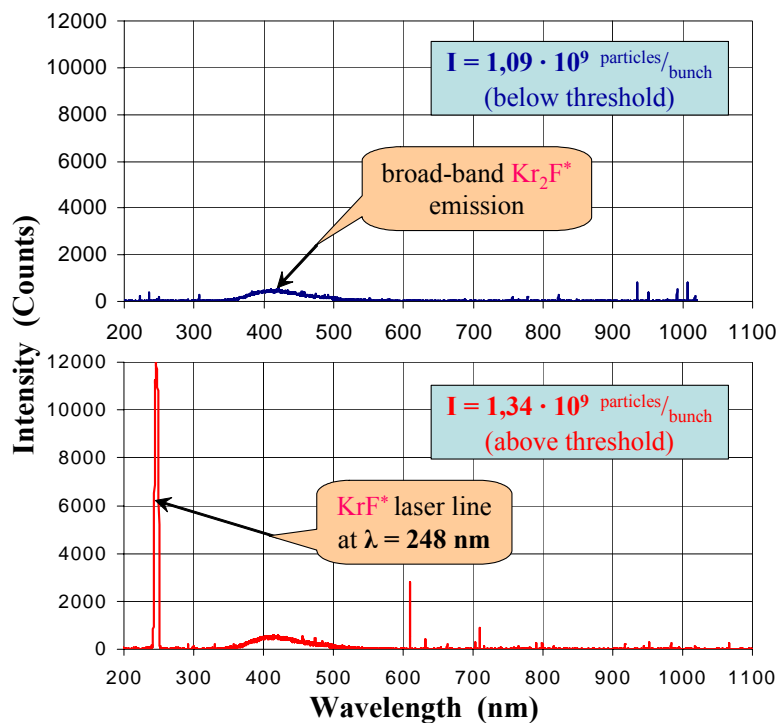


Abbildung 1: Darstellung der Laserschwelle.

Laserschwelle des Excimers bei diesem Aufbau lag bei einer Leistungsdichte von $0,51 \text{ MW/cm}^3$. Dies entspricht einer Strahlintensität von $1,2 \cdot 10^9$ Ionen pro Puls. Die Laseraktivität wurde zusätzlich noch durch verschiedene Messmethoden klar nachgewiesen.

Die Methoden zum Nachweis von Laseraktivität werden im folgendem kurz erläutert:

– *Auftreten einer Laserlinie*

Eine starke Laserlinie trat im Spektrum auf der Achse auf, sobald die Intensität des Ionenstrahls $1,2 \cdot 10^9$ Teilchen pro Puls überstieg.

– *Spektrale Verschmälerung der Laserlinie*

Die spektrale Breite (W) der KrF^* -Laserlinie im Spektrum, die entlang der Strahlachse beobachtet wurde, war fast um einen Faktor 2 schmäler als im Spektrum der spontanen Emission, das senkrecht zur Strahlachse aufgenommen wurde. Jedoch war eine quantitative Analyse dieses Effekts durch die optische Auflösung des Spektrometers begrenzt.

– *Zeitliche Verkürzung des Lasersignals*

Verschiedene zeitliche Strukturen der spontanen und der induzierten Emission wurden während der Experimente vermessen. Dabei wurde beobachtet, dass die Anstiegsflanke bei induzierter Emission einen steileren Verlauf hatte als bei spontaner Emission. Die maximale Zeitdauer des Laserpulses entsprach ungefähr 87 ns, was in etwa der Zeitdauer des gepulsten Ionenstrahls entsprach. Im Gegensatz zur induzierten Emission war die Leuchtdauer der spontanen Emission nicht abhängig von der Zeitdauer des maximalen Ionenstromes. Bei der spontanen Emission wurde eine Leuchtdauer von 150 ns (Halbwertsbreite) gemessen. Die längere Zeitdauer ist auf ein Nachleuchten von etwa 40 ns infolge von spontaner Emission zurückzuführen.

– *Schwellenwertverhalten und Nichtlinearität der Laserstrahlung im Verhältnis zur Pumpenergie.*

Bei der spontanen Emission besteht ein linearer Zusammenhang zwischen Pumpenergie und Intensität der emittierten Strahlung. Hingegen beim Nachweis zur induzierten Emission und somit von Laserstrahlung konnte ein Schwellenwertverhalten und ein nichtlinearer Zusammenhang zwischen Pumpenergie und der Intensität der Laserstrahlung nachgewiesen werden.

– *Effekt durch Dejustage des Resonators*

Mit der Verstimmung des Laserresonators verschwand der Effekt der Laserverstärkung vollständig, während er bei den erneuten Justagen der Spiegel des Resonators wieder auftrat.

Die Energiekalibrierung der Photodioden wurde mit Hilfe eines kommerziellen KrF* Excimer-Lasers mit bekannter Leistung und Pulslänge durchgeführt. Bei einer Strahlintensität von $2 \cdot 10^9$ Teilchen pro Puls entsprach die maximale Energie des Laserstrahls 2 mJ. Die Konversionseffizienz von Ionenstrahlenergie in Laserlicht wurde zu 0,04% bestimmt.

Ebenso wurde die zeitliche Verzögerung der induzierten Emission gegenüber dem Pumpimpuls analysiert und ausgewertet. Es stellte sich ein direkter Zusammenhang zwischen dem Einsetzen des Laserstrahls (Delay) und der Pumpleistung heraus. Die Verzögerungswerte lagen zwischen 120 und 85 ns bei Strahlintensitäten zwischen $1,3 \cdot 10^9$ und $2,5 \cdot 10^9$ Teilchen pro Puls.

Ebenso wurde das Spektrum bei spontaner Emission in Abhängigkeit des Gasdruckes zwischen 1,3 und 2 bar untersucht. Die Messungen ergaben, dass sich bei hohen Drucken die niedrigste Effizienz an Laseremission einstellte.

Ein wichtiges Ergebnis dieser Arbeit ist, dass gezeigt werden konnte, dass die Intensität sowie die räumlichen und zeitlichen Eigenschaften des Ionenstrahls des Schwerionen-Synchrotrons SIS-18 der GSI ausreichend sind, um einen schwerionensreihgepumpten Gaslaser im UV-Wellenlängenbereich zu realisieren.

Als nächsten Schritt für die Untersuchung von kurzwelligen, Schwerionenstrahl-gepumpten Lasern ist eine Reduzierung der Wellenlänge bis unterhalb von $\lambda < 200$ nm (Vakuum-Ultraviolett-Wellenlängenbereich) sowie Experimente mit reinen Edelgasen geplant. Für weitere Experimente ist vorgesehen, den Übergang des so genannten zweiten Kontinuums der verschiedenen Edelgase zu untersuchen. Die Excimermoleküle dieser Gase und ihre charakteristischen Laserübergänge sind: Xe₂* ($\lambda = 172$ nm), Kr₂* ($\lambda = 146$ nm), Ar₂* ($\lambda = 126$ nm), Ne₂* ($\lambda = 83$ nm) and He₂* ($\lambda = 80$ nm). Die Vorteile von Systemen mit reinen Edelgasen gegenüber korrosiven Edelgasgemischen sind die einfachere technische Realisierbarkeit und die geringeren Sicherheitsbestimmungen für den Umgang im Labor. Jedoch werden für reine Excimer gases gegenüber KrF* beträchtlich höhere Anregungsenergien wegen der kürzeren Wellenlängen und des breiteren Laserübergangs benötigt.

Die benötigten Leistungsdichten um die Edelgasexcimerlaser zu betreiben betragen gemittelt entlang der Strahlachse 41 MW/cm^3 und $40,8 \text{ MW/cm}^3$. Dies entspricht einer maximalen Intensität des Uranstrahls von $4 \cdot 10^9$ Teilchen pro Puls in einer Pulsdauer von 100 ns (Halbwertsbreite). Die Kleinsignalverstärkung wurde für Xe zu 4,3% und für Kr zu 2,3% geschätzt.

Der erwartete Wert der Nettoverstärkung pro Einzelumlauf ist 2,5 für Xe und 1,2 für Kr. Da für einen 100 ns andauernden Pumpimpuls 42 Einzelumläufe angenommen werden, kann für beide Fälle eine klare Laseraktivität erwartet werden.

Die Verwendung von Schwerionen zum Pumpen von Gaslasern führt durch den hohen Wirkungsquerschnitt des Gases zu Mehrfachionisation und somit zu neuen Anregungsmechanismen von höher liegenden Energieniveaus. Demzufolge besteht die Möglichkeit beträchtlich kürzere Wellenlängen (ggf. im extremen UV- und Röntgenspektralbereich) von Laserstrahlung erzeugen zu können. Mit dem Zukunftsprojekt FAIR, einer Einrichtung für Antiprotonen- und Ionenforschung, ist eine Erweiterung des bereits bestehenden Beschleunigers für Schwerionen an der GSI geplant. Die beantragte Erweiterung enthält unter anderem den Bau von zwei neuen Speicherringen, dem SIS-100 und SIS-300. FAIR soll zukünftig hochgeladene Ionen erzeugen mit Strahlströmen, die um zwei Größenordnungen höher liegen bei gleichzeitig dreifach höheren Strahlintensitäten, als die der jetzigen Einrichtung der GSI. Mit dieser geplanten Erweiterung könnten neue Wege für die Untersuchung neuartiger hochenergetischer Laserquellen für kurze Wellenlänge erschlossen werden. Mit dem von FAIR beabsichtigten Strahlparametern könnten neue Wege für effektive Anregungsniveaus entstehen, die nur mit intensiven Schwerionen erreicht werden können.

Acknowledgements

At the end of my work I would like to express my gratitude to all people who have contributed in this work and whose help and support were so necessary for its successful performing.

First of all, I am glad to acknowledge Prof. Dr. Joachim Jacoby from the Institute of Applied Physics (IAP) at Frankfurt University (JWG-Uni Frankfurt-am-Main) for his support and advice on many aspects of the work as well as for his care and friendly assistance, which was helping a lot.

My very special thanks are addressed to the “father” of heavy-ion-beam pumped laser experiments at GSI, Priv. Doz. Dr. Andreas Ulrich from Physic Department of the Munich Technical University (TUM). Without his extensive knowledge, professional approach and great scientific experience in the field of coherent and incoherent excimer light sources, this experiment could not be possible. I am also very grateful to him for providing corrections and detailed comments on the thesis, which has significantly improved its quality.

I am particularly indebted to my friend and colleague from the Institute for Theoretical and Experimental Physic (ITEP), Dr. Vladimir Turtikov for his expert support in all aspects of the experimental work. His tremendous enthusiasm, excellent ideas and unlimited energy have strongly motivated me during the preparations and the experiment. His help has played a significant role in the success of the experiment.

A lot of thanks I would like to say to our Munich collaborators: Dr. Jochen Wieser from Coherent Company for his inestimable help in technical support and for many illuminating discussions; and Dr. Andrey Morozov from TUM, owing to the fruitful discussions with him I got started to be more or less familiar with laser theory at the beginning of my work.

I would very like to acknowledge the leader of Plasma Physics group at GSI, Prof. Dr. Dr.h.c. Dieter H.H. Hoffmann for supporting of this project and for his indispensable help in many administrative questions. In many respects owing to his efforts the experiment became possible.

I would also like to express my gratitude:

To Dr. Olga Rosmej for primary corrections of my thesis and many helpful discussions. Her kind care was always there even besides the professional activities.

To the entire HHT team for the long beamtime nights shared together and personally Dr. Dmitry Varentsov for positioning and alignment of the ion

beam for the experiment. Without his professional assistance the experiment was not possible.

To Gabriel Schaumann and Heinrich Wahl for they help with ordering, technical support and very useful advices.

To Renate Knobloch for English corrections and Frank Nürnberg and Marius Schollmeier for German corrections in my thesis.

To the entire Plasma Physics group for being nice colleagues and for the pleasant time spent together.

During my work I had close communications with the specialists from other groups at GSI, so I wish to especially thank:

Dr. Alexey Dolinskiy from Accelerator Division. He has provided me with important knowledge about the ion optics, acceleration principles and the calculation of the ion beam spatial parameters.

Dr. Kalliopi Dermati from Material Research group for her inestimable help in choosing and testing the materials for the ion beam entrance window and diagnostic viewports during preparations for the experiment.

Dipl.-Ing. Markus Römig, the head of the workshop, owing to his efforts the manufacturing of many parts of the experimental setup were very fast.

Dr. Dobri Dobrev from Material Research group for plenty of fruitful discussions. The investigations with electron microscope could not be successful without his professional assistance.

I am also very grateful to my Frankfurt colleagues, to the entire Plasma Physics group of the IAP at University of Frankfurt. It was a pleasure to work in such a warm and friendly atmosphere. Thanks a lot for your seasonable support and, of course, for the pleasant time spent together. My special thanks are addressed to Dr. Markus Iberler for his opportune help with German translation. His inexhaustible optimism and very friendly relationship were always in time and gave a hope for the best.

The research was funded by the German Ministry of Research and Education (BMBF).

I can not offer enough thanks to my parents and parents of my wife for their endless supporting during several years away from home.

And at last, but not least, I would like to say a Great Thanks to my family: my wife Marina Adonina, my daughter Diana Adonina and my son Mikhey Adonin for their love and patience, which were surrounding me all this time. Without their support this thesis would not have been possible.

Curriculum Vitae

Name: Aleksey Adonin
Birth date: 21 January 1979
Birth place: Omsk, Russia
Citizenship: Russian
Parents: father: Adonin Alexandr Dmitrievich
mother: Adonina Ludmila Andreevna
Marital status: married

Educational Profile:

1985 – 1988: Primary school, Snechkus, USSR
1988 – 1996: Secondary and high-school, Sosnovy Bor, Russia
June 1996: School leaving certificate
1996 – 2003: St. Petersburg State University, Russia
June 2000: Certificate of degree „Bachelor of Science“
February 2003: Certificate of degree „Master of Science with Honours“
since May 2003: PhD student at Johann Wolfgang Goethe-University, Frankfurt am Main, Germany.
14 March 2008: Date of the Disputation.